Production Cross Section Measurement of Top–Antitop Pairs in the Dimuon Decay Channel at $\sqrt{s} = 7\,\mathrm{TeV}$ with the CMS Experiment

Dissertation
zur Erlangung des Doktorgrades
des Department Physik
der Universität Hamburg

vorgelegt von

Dirk Dammann

aus Buxtehude

Hamburg
2011

Gutachter der Dissertation: Prof. Dr. Joachim Mnich
Priv.-Doz. Dr. Achim Geiser

Gutachter der Disputation: Prof. Dr. Joachim Mnich
Prof. Dr. Peter Schleper

Datum der Disputation: 27. April 2011

Vorsitzende des Prüfungsausschusses: Prof. Dr. Caren Hagner
Vorsitzender des Promotionsausschusses: Prof. Dr. Joachim Bartels

Leiterin des Departments Physik: Prof. Dr. Daniela Pfannkuche
Dekan der MIN-Fakultät: Prof. Dr. Heinrich Graener

Abstract

The LHC started to produce first proton–proton collisions at a centre of mass energy of 7 TeV in spring 2010 opening up a new energy scale for particle physics. During the first data taking period, the CMS detector has recorded $35.9\,\mathrm{pb}^{-1}$ of data. One of the first goals is the rediscovery and precision measurement of the already known standard model. Especially the top quark is interesting since it is the heaviest particle observed by now. In this work, an early measurement of the top–antitop cross section using the first CMS data is presented, which is based on 28 selected candidate events. The dimuon decay channel $t\bar{t} \rightarrow b\bar{b}\,\mu^+\mu^- + \mathit{neutrinos}$ has been chosen for this study since the two isolated muons give a clear signature to distinguish signal events from the QCD background.

The contribution of events with muons from heavy flavour decays and misidentified muons is expected to be the least understood background in first data. Most important background, however, is the Drell–Yan production of a muon pair accompanied by additional hard jets. For this reason, both backgrounds are estimated from data. Several approaches are studied for the measurement of the cross section. The default selection of two muons, two jets from the hadronised b quarks, and missing transverse energy is improved by applying a kinematic reconstruction algorithm for the top mass. Both attempts give consistent results. In addition, two b tagging algorithms are tested to improve the significance. They lead to compatible results for the cross section. The value obtained by the mass reconstruction method, which is taken as final result, is $\sigma_{t\bar{t}} = 150 \pm 48\ (\mathrm{stat.}) \pm 35\ (\mathrm{syst.}) \pm 6\ (\mathrm{lumi.})\,\mathrm{pb}$.

Zusammenfassung

Im Frühjahr 2010 erzeugte der LHC die ersten Proton-Proton-Kollisionen bei einer Schwerpunktsenergie von 7 TeV, womit ein neuer Energiebereich für die Teilchenphysik erschlossen wird. Während der ersten Periode der Datennahme zeichnete der CMS-Detektor 35,9 pb^{-1} an Analysedaten auf. Eines der ersten Ziele ist die Wiederentdeckung und präzise Vermessung des bereits bekannten Standardmodells. Vor allem das Top-Quark ist dabei von Interesse, da es das schwerste bisher beobachtete Teilchen ist. In dieser Arbeit wird eine Messung des Wirkungsquerschnitts für die Produktion von Top-Antitop-Paaren präsentiert, die auf 28 selektierten Ereigniskandidaten basiert. Für die Analyse wurde der dimyonische Zerfallskanal $t\bar{t} \rightarrow b\bar{b}\,\mu^{+}\mu^{-} + \mathit{Neutrinos}$ als Signalkanal gewählt, da er durch die zwei isolierten Myonen eine klare Signatur bietet um Signalereignisse vom QCD-Untergrund zu unterscheiden.

In den ersten Daten erwartet man, dass der Beitrag von Myonen aus dem Zerfall schwerer Quarks und von fehlidentifizierten Myonen der am wenigsten verstandene ist. Der wichtigste Untergrund ist jedoch die Drell-Yan-Produktion eines Myonenpaares mit zusätzlichen Jets. Beide diese Untergründe werden daher aus Daten bestimmt. Für die Messung des Wirkungsquerschnitts werden verschiedene Ansätze probiert. Die Standardselektion von zwei Myonen, zwei Jets aus den hadronisierten b-Quarks und fehlender Transversalenergie wird durch einen kinematischen Rekonstruktionsalgorithmus für die Top-Masse verbessert. Dieses Vorgehen liefert ein konsistentes Ergebnis. Zusätzlich werden zwei verschiedene Algorithmen zur Identifikation von b-Jets betrachtet, um die Signifikanz des Signals zu verbessern. Dies führt ebenfalls zu kompatiblen Werten für den Wirkungsquerschnitt. Der Wert, der mit der Massenrekonstruktionsmethode ermittelt wird, wird als Endergebnis genommen. Er beträgt $\sigma_{t\bar{t}} = 150 \pm 48\ (\mathrm{stat.}) \pm 35\ (\mathrm{syst.}) \pm 6\ (\mathrm{lumi.})\ \mathrm{pb}$.

Contents

Chapter 1

Introduction

In this work, an early measurement of the top–antitop production cross section at the new energy scale opened up by the Large Hadron Collider (LHC) is presented. The top quark is until today by far the heaviest elementary particle observed with a mass comparable to that of a large atom. This is the reason why the top quark was one of the last particles of the standard model that was discovered. Only the tau neutrino was proven later. The Higgs boson, which is also part of the standard model, has not been observed until today.

The prediction of the existence of the top quark goes back to the 1970s when M. Kobayashi and T. Maskawa postulated the existence of a third generation of particles to explain the CP violation of the kaon decay [1]. Although the down-type partner of the top quark, the bottom quark, was already discovered in 1977 [2], it took almost 20 years until also the existence of the top quark could be proven in direct observation.

The top quark was finally discovered by the CDF and DØ experiments in 1995 at the Tevatron accelerator at Fermilab [3]. After the discovery, the Tevatron stayed to be the only machine in the world that was able to accelerate particles to an energy sufficient for the production of top quarks for almost one and a half decades. The LHC exceeded the energy of the Tevatron with two proton beams for the first time by the end of November 2009 [4]. Proton–proton collision data at a centre of mass energy of 7 TeV, which approximately three and a half times higher than the Tevatron energy, are recorded since Spring 2010. Top quarks are therefore produced with a much higher rate and the top quark was rediscovered after only few months in the first $3\,\mathrm{pb}^{-1}$ of data by the CMS and the ATLAS experiments [5] [6]. With the data that will be recorded in 2011, the LHC experiments should already be able to improve the Tevatron results.

Although the top quark has already been observed at the Tevatron, the study of its properties and especially the measurement of the production cross section at the LHC is important and interesting. Many intrinsic properties of the top quark still have large uncertainties due to the limited statistics collected at the Tevatron. Further, top quarks are expected to be background for many processes assumed beyond the standard model or appear in the decays of exotic particles. Hence, it is crucial to measure and to understand the production mechanism of top quarks.

The analysis presented in this work is also documented in a CMS-internal analysis note with all technical details [7]. That note is used as cross check for the upcoming CMS publication which combines cross section measurements from three different dileptonic decay channels [8].

This work is organised in the following way. In Chapter 2, the necessary physical basics are described. The standard model of particle physics and the process of hadron–hadron interaction are introduced. The theory of top quark physics like production, decay, and mass are expounded as well as its connection to the standard model and theories beyond. Also, the status of experimental results is summarised.

In Chapter 3, the Large Hadron Collider and its experiments are introduced. Especially the CMS detector and its subdetector components that are relevant for this study are described in detail.

Chapter 4 is about simulation of collision events using Monte Carlo event generators. The software used for this analysis is briefly described.

Chapter 5 summarises the data processing at CMS. The trigger system is explained as well as the measurement of the luminosity. The reconstruction of physics objects is depicted for those objects which are needed for this analysis.

The description of the analysis starts in Chapter 6. In this chapter the event signature is characterised and subsequently the selection of signal events is presented.

Systematic studies concerning the selection efficiency of signal events are expounded in Chapter 7 as well as two different methods to estimate the background using data. The results of this studies are used to correct the predictions made by the simulation.

Based on these results, the production cross section is calculated in Chapter 8. A summary of all uncertainties is also given.

Subsequently, additional steps are studied to improve the result. In Chapter 9, an algorithm is applied on all selected candidate events to reconstruct the mass of the top quark candidates. This is done to validate the top-like topology of the selected events and to further reduce remaining background since not for all events a solution of the event kinematics exist.

As an alternative to the kinematic event reconstruction, two different b tagging algorithms are studied in Chapter 10.

Finally, all results are summarised in Chapter 11. The final value for the top–antitop production cross section is compared to theoretical predictions and to first measurements published by the CMS and ATLAS collaborations.

Chapter 2

The Top Quark in Particle Physics

2.1 Standard Model of Particle Physics and Theories beyond

Our present understanding of particles and their interactions is most consistently summarised in the standard model of particle physics. In the standard model, all visible matter that we can observe in the universe is composed of 12 fermions while their interactions are described by the exchange of force mediating particles. These interactions are the electromagnetic, the strong, and the weak interaction. The gravity as the fourth known interaction is not described in the standard model and is many orders of magnitude weaker than the other three forces.

From the theoretical point of view, the standard model is a relativistic quantum field theory. The interactions are a result of local gauge invariance of the fermion's wave functions. More extensive descriptions of the standard model than presented here can be found in several textbooks, e.g. [9].

2.1.1 Particles

All particles contained in the standard model and their most important properties are listed in Table 2.1. In the first three columns, the fermions are displayed sorted in quarks (red), charged leptons (orange), and uncharged leptons (yellow) that are called neutrinos. This classification is established by the different interactions the particles are liable to. The quarks underlie the strong as well as the electromagnetic and weak interaction. The charged leptons interact electromagnetically and weakly while the neutrinos only underlie the weak force.

The three columns containing the fermions correspond to the three generations of matter particles. We find four fermions in each generation, which have

	1. Generation	**2. Generation**	**3. Generation**	**Gauge Bosons**
Quarks	**u** **up** $s = 1/2$ $Q = +2/3e$ $m = 1.5$–$3\,\mathrm{MeV}$	**c** **charm** $s = 1/2$ $Q = +2/3e$ $m = 1.27^{+0.07}_{-0.11}\,\mathrm{GeV}$	**t** **top** $s = 1/2$ $Q = +2/3e$ $m = 173 \pm 1\,\mathrm{GeV}$	γ **photon** $s = 1$ $Q = 0$ $m < 10^{-18}\,\mathrm{eV}$
	d **down** $s = 1/2$ $Q = -1/3e$ $m = 5.5$–$6\,\mathrm{MeV}$	**s** **strange** $s = 1/2$ $Q = -1/3e$ $m = 104^{+26}_{-34}\,\mathrm{MeV}$	**b** **bottom** $s = 1/2$ $Q = -1/3e$ $m = 4.2^{+0.2}_{-0.1}\,\mathrm{GeV}$	$\mathbf{Z^0}$ $s = 1$ Q=0 $m = 91.2\,\mathrm{GeV}$
Leptons	$\mathbf{e^-}$ **electron** $s = 1/2$ $Q = -1e$ $m = 0.51\,\mathrm{MeV}$	$\boldsymbol{\mu^-}$ **muon** $s = 1/2$ $Q = -1e$ $m = 105.6\,\mathrm{MeV}$	$\boldsymbol{\tau^-}$ **tau** $s = 1/2$ $Q = -1e$ $m = 1777\,\mathrm{MeV}$	$\mathbf{W^\pm}$ $s = 1$ $Q = \pm 1e$ $m = 80.4\,\mathrm{GeV}$
	$\boldsymbol{\nu_e}$ **electron neutrino** $s = 1/2$ $Q = 0$ $m < 2\,\mathrm{eV}$	$\boldsymbol{\nu_\mu}$ **muon neutrino** $s = 1/2$ $Q = 0$ $m < 2\,\mathrm{eV}$	$\boldsymbol{\nu_\tau}$ **tau neutrino** $s = 1/2$ $Q = 0$ $m < 2\,\mathrm{eV}$	**g** **gluon** $s = 1$ $Q = 0$ m=0

Table 2.1: The elementary particles of the standard model listed with spin quantum number, electric charge and masses in the $\overline{\mathrm{MS}}$ scheme [10][1]. The Higgs boson is not shown in the table although it is also part of the standard model.

the same properties as the corresponding particles in the other two generations except for their different masses. The top that is the third generation up-type quark has the highest mass comparable to that of a heavy atom. For each of these 12 standard model fermions, there exists an antifermion with opposite charge but apart from that identical properties.

The gauge bosons of the standard model, which are the force-mediating particles, are shown in the most right column of Table 2.1. The photon is the gauge boson of the electromagnetic interaction while the gluon carries the strong force. Three gauge bosons, which are called Z^0, W^+, and W^-, are needed to describe the observed weak processes.

The Higgs boson is not contained in the table since it is the only particle of the standard model that has not been observed until today. But there are strong theoretical arguments why such a particle should exist. These arguments and the expected properties of the Higgs will be treated in Subsection 2.1.3.

---

[1] For top mass see 2.3.3

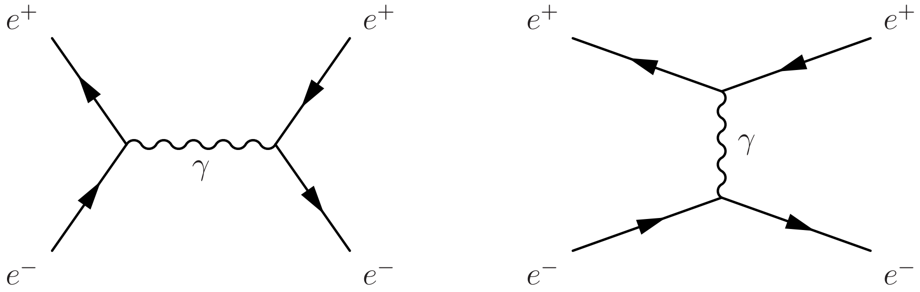

(a) s-channel (b) t-channel

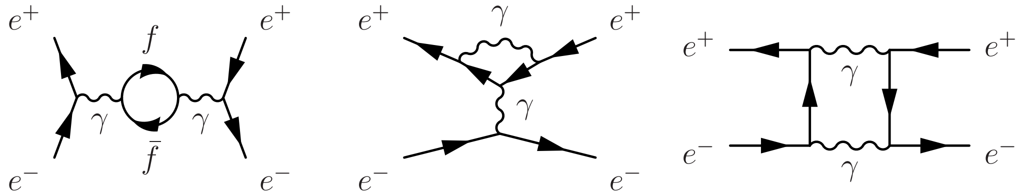

(c) s-channel with virtual $f\bar{f}$-loop (d) t-channel with vertex correction (e) box graph

Figure 2.1: Feynman diagrams for electron–positron scattering (Bhabha scattering [13]): Subfigures (a) and (b) show the leading order graphs while (c), (d), and (e) show three examples for next-to-leading order (NLO) corrections with four vertices.

2.1.2 Interactions

In relativistic quantum field theory, the fermions and interactions are mathematically described as terms in the Lagrangian density of the fields. The form of the interaction terms result from the postulated invariance under certain continuous gauge transformations, which are represented as Lie groups. The interaction mediating particles are linked to the generators of the corresponding gauge group. According to Noether's theorem, this invariance leads to a conserved quantity that can be identified as a charge of the interacting particle.

Electromagnetic Interaction Particles with electric charge interact by exchanging virtual photons, which are the quanta of the electromagnetic field. The electromagnetic field is found by demanding gauge invariance of the standard model Lagrangian regarding to an arbitrary time and space dependent $U(1)$ gauge transformation.

Since the coupling constant of the electromagnetic interaction

$$\alpha = \frac{e^2}{4\pi} \ll 1 \tag{2.1}$$

is small, this interaction can be handled in perturbation theory. The different steps of perturbation theory can be visualised as Feynman diagrams. Figure 2.1 shows as an example some Feynman diagrams for electron–positron scattering. Quantum electro dynamics (QED) is one of the best and most exactly proven theories in physics [11][12].

Strong Interaction The gauge group of the strong interaction is $SU(3)_C$. From this group symmetry, it follows that there are three different charge eigenstates of the quarks named colour. These three colour eigenstates are called red, green, and blue. The theory of the interaction is called quantum chromodynamics (QCD). Further, it can be deduced from the the group structure that there is an octet of eight gluons that carry colour and anticolour charge and a singlet that is invariant under colour transformation. The singlet gluon is not observed in nature. Gluons can also couple to each other, which can also be deduced from the non-abelian $SU(3)_C$ group structure.

The strength of the strong interaction is quantified by the strong coupling constant α_s, which depends on the momentum transfer Q^2 of an interaction, respectively on the distance of the two interacting quarks. At low Q^2, corresponding to large distances of $\mathcal{O}(10^{-13}\,\mathrm{cm})$, α_s becomes very large. The consequence is that quarks cannot be observed as free particles but are always bound as hadrons. This is called confinement of the quarks: if two quarks are separated from each other, at a certain point the gluon field energy becomes so high that it is energetically more beneficial to create a quark–antiquark pair. This happens in high energy collisions with outgoing quarks and gluons and is called hadronisation.

Hadrons consist either of three quarks (baryons), three antiquarks (antibaryons) or a quark–antiquark pair (mesons) so that they build a colour singlet. The existence of other combinations like $qqqq\overline{q}$ is controversial although indications have been seen in some experiments e.g. [14].

At small distances, corresponding to higher Q^2, α_s becomes small. This is called asymptotic freedom of the quarks. The running behaviour of α_s leads also to the consequence that interactions at high energy scales can be calculated in perturbative QCD. At the QCD scale $\Lambda_\mathrm{QCD} \approx 220\,\mathrm{MeV}$ the coupling becomes unity so that perturbation theory can not be applied.

Weak Interaction The weak interaction has some interesting characteristics that make it very special. It violates parity [15] since the interaction only couples to left-handed fermions and right-handed antifermions.

Also, the weak interaction is much weaker than the other two forces at low energy scales. This is due to the high masses of the weak gauge bosons, which are of order 100 GeV. Above the unification energy, the weak and the electromagnetic force merge into a single electroweak force. The formalism of this electroweak unification will be described in the next subsection.

Weak interactions with electrically charged currents have been observed in experiments as well as reactions with neutral currents. An example for charged current is the β-decay of atomic nuclei while the neutral current has been discovered in reactions between neutrinos and nuclei at the Gargamelle experiment in 1973 [16].

Historically, the weak interaction has originally been described as an interaction between four fermions with a coupling constant G_F. The β-decay, for example, was described as a neutron directly decaying into a proton, an electron, and an antineutrino. This approximation can be used for lepton–lepton scattering with low momentum transfer but renormalisability made it necessary to replace this four particle interaction by an exchange of Z^0 or $W^\pm$ bosons. These particles have directly been observed at the UA1 and UA2 experiments [17][18][19] and have been measured with remarkable precision in later experiments at LEP and at the Tevatron [20][21].

The weak eigenstates of the quarks differ from their mass eigenstates. For this reason, the weak interaction can transform quarks from one generation into those of another. This is to leading order only possible in charged currents in which an up-like quark converts into a down-like quark and vice versa through coupling to a $W^\pm$. The transition probability between the different quark flavours is given by the Cabibbo–Kobayashi–Maskawa-matrix (CKM-matrix) [22], which transforms the down-like quark's mass eigenstates into the weak eigenstates:

$$\begin{pmatrix} u' \\ s' \\ b' \end{pmatrix} = \begin{pmatrix} V_{ud} & V_{us} & V_{ub} \\ V_{cd} & V_{cs} & V_{cb} \\ V_{td} & V_{ts} & V_{tb} \end{pmatrix} \times \begin{pmatrix} u \\ s \\ b \end{pmatrix}. \tag{2.2}$$

The matrix elements in the lower row involving the top quark are not yet directly measured very well and $|V_{td}|$ and $|V_{ts}|$ have only been measured indirectly from $B\overline{B}$ oscillations or loop-mediated K and B decays [23]. In the standard model, the unitarity of the CKM-matrix is assumed. It is therefore expected that $|V_{tb}|$ is close to one and $|V_{td}|$ and $|V_{ts}|$ are hence close to zero. The most precise direct measurement until today without the assumption of unitarity states

$$|V_{tb}| > 0.78 \quad \text{at 95\% C. L. [24][25].}$$

A similar mixing has been observed in the lepton sector that causes neutrino oscillations between the different generations and is evidence for the non-zero mass of the neutrinos. The corresponding mixing matrix is called Maki–Nakagawa–Sakata-matrix (MNS-matrix) [26][27].

2.1.3 Electroweak Unification and the Higgs Boson

In order to formulate the weak interaction as a gauge theory, it is postulated that the Lagrangian of the standard model is invariant with respect to a $SU(2)$ transformation. This is achieved by introducing three new gauge fields W^1_μ, W^2_μ, and W^3_μ into the Lagrangian, which couple to the fermions with the coupling constant g. The linear combinations of the first two fields

$$W^\pm_\mu = \frac{1}{\sqrt{2}}(W^1_\mu \mp iW^2_\mu) \tag{2.3}$$

can be identified with the fields of the $W^\pm$ bosons since they couple to left-handed fermions and not to those that are right-handed. The left-handed fermions can be ordered in doublets of the weak isospin T. These doublets contain either a charged lepton ($T_3 = -\frac{1}{2}$) and the corresponding neutrino ($T_3 = +\frac{1}{2}$) of the same generation or a down-type quark ($T_3 = -\frac{1}{2}$) and the corresponding up-type quark ($T_3 = +\frac{1}{2}$). The interaction with a $W^\pm$ flips in this formalism the component T_3 of the weak isospin within one doublet.

The $U(1)$ symmetry to include electromagnetic interaction gives a fourth field called B_μ with the coupling constant g'. Both fields B^3_μ and W^3_μ couple to the neutrinos, and therefore cannot be identified with the electromagnetic field. Instead, the electromagnetic field A_μ is a linear combination of both fields orthogonal to the term responsible for the neutrino coupling Z^μ. The solution can be written in the form

$$A_\mu = \frac{1}{\sqrt{g^2 + g'^2}}(gW^3_\mu - g'B_\mu) = W^3_\mu \cos\vartheta_\mathrm{W} - B_\mu \sin\vartheta_\mathrm{W} \tag{2.4}$$

$$Z_\mu = \frac{1}{\sqrt{g^2 + g'^2}}(gW^3_\mu - g'B_\mu) = W^3_\mu \sin\vartheta_\mathrm{W} + B_\mu \cos\vartheta_\mathrm{W} \tag{2.5}$$

with the weak mixing angle ϑ_W, which is a free parameter of the standard model and has to be determined from experiments [28][29]. The elementary electric charge is given by

$$e = g \sin\vartheta_\mathrm{W} = g' \cos\vartheta_\mathrm{W}. \tag{2.6}$$

The electric charge Q and the weak isospin T can be combined to a weak hypercharge Y defined by a Gell-Man–Nishijima relation

$$Y = 2(Q - T_3). \tag{2.7}$$

The gauge symmetry of the electroweak theory is $SU(2)_L \otimes U(1)_Y$ of the weak isospin and the weak hypercharge. This model is also named the Glashow–Salam–Weinberg model [30].

This formal description has a large problem. Gauge symmetry is only conserved if the gauge bosons are massless. An ad hoc introduction of mass terms into the Lagrangian breaks the gauge invariance. The standard model solution is to postulate the existence of an additional quantum field coupling to the particles that are a priori massless so that the particles get their mass dynamically through this coupling. This field is called the Higgs field. The special property of the Higgs field is its non-zero vacuum expectation value caused by a spontaneous symmetry breaking, which is necessary to make the mechanism work [31].

The particle of this field is the Higgs boson, which is expected to be a spin-0 boson. The theory makes no prediction about its mass but direct searches have excluded a mass lower than 114 GeV at the LEP experiments [32] and between 163 GeV and 166 GeV at the Tevatron [33]. The mass of the Higgs boson is connected to those of the other standard model particles via radiative corrections. For this reason, a fit can be applied giving a most probable value for the Higgs boson mass. The results can be seen in Figure 2.2. They prefer a small mass with the highest probability in the region excluded by the LEP

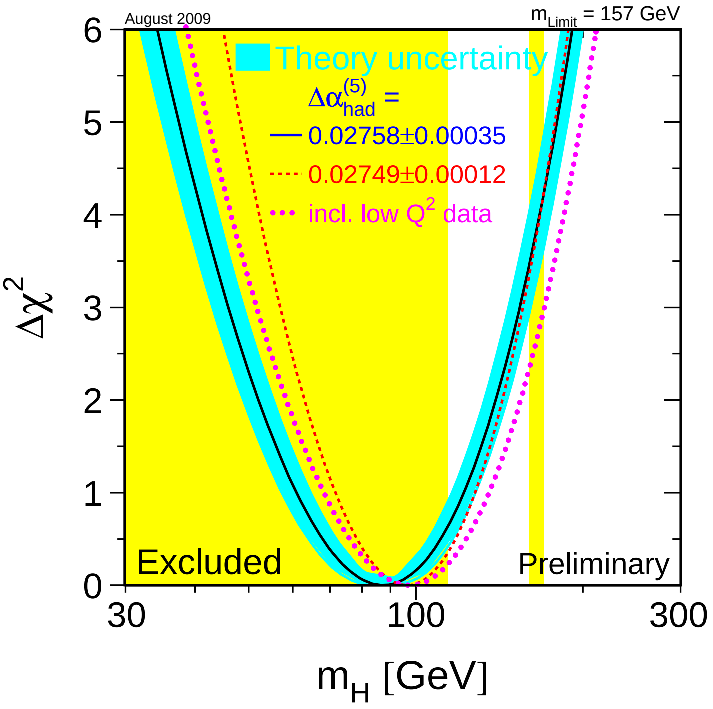

Figure 2.2: Higgs mass exclusion and fits [34].

experiments. In Subsection 2.3.4 the interrelationship between the particle masses will be explained in more detail.

There is an additional argument for the existence of the Higgs boson. Like in QCD, the non-abelian structure of the electroweak gauge group results in a self-coupling of the gauge bosons. The $W^{\pm}$ and Z^0 bosons can couple with each other, and also the photon can couple to the $W^{\pm}$ since they carry electric charge. For some processes with longitudinally polarised bosons, the scattering amplitude exceeds the unitarity limit at tree level. This can only be fixed by assuming additional Feynman graphs containing the Higgs boson with a mass lower than 1 TeV so that also an upper limit for the Higgs mass is given [35].

2.1.4 Extensions of the Standard Model

Although the standard model describes most observations in high energy physics very precisely, it leaves some open questions. One is the question of the nature of the dark matter that is observed only by its gravitational influence on the visible matter. Measurements show that there is much more dark than visible matter in the universe and that it contributes about 23% of the energy density of the universe [36].

Another problem is the hierarchy problem between the electroweak unification scale and the grand unification scale, which is the scale where electroweak and strong interaction become equal in strength and which is orders of magnitude larger. The Planck scale, which is the scale where quantum effects of gravity become important, is even larger. Because of radiative corrections of the same order of magnitude as these very large scales, the Higgs mass should be very large compared to the masses of the other standard model particles. A small Higgs mass can only be explained by a fine-tuning mechanism in which the quantum corrections cancel each other.

A solution for both of these problems would be a supersymmetry between fermions and bosons. In supersymmetric models, each fermion has a partner boson with integer spin and apart from that same quantum numbers and each boson has a partner fermion with half-integer spin. No such superpartners have been observed yet, so supersymmetry must be broken if it is realised in nature. This means that the masses of the superpartners must be much higher than the masses of the corresponding standard model particles. In most supersymmetric models, there is a conservation of a newly introduced R-parity. This conservation has the effect that the lightest supersymmetric particle is stable. This particle would be a proper candidate for dark matter if it is uncharged. The hierarchy problem is solved in supersymmetry in a natural way since each quantum correction containing standard model fermions is compensated by the corresponding boson and vice versa.

In the minimal supersymmetric standard model (MSSM) [37], there is not only one Higgs boson but five. The h^0, H^0 and A^0 are uncharged but there are also charged Higgs bosons $H^{\pm}$. The h^0 and the H^0 are CP-even like the standard model Higgs boson while the A^0 is CP-odd. The h^0 is expected to have a relatively low mass and therefore to be similar to the standard model Higgs. Even more Higgs bosons are needed in more complex supersymmetric extensions of the standard model in order to achieve a consistent theory.

There are also many models that try to solve the hierarchy problem and to include also gravity into the theory by introducing extra space dimensions. These extra dimensions are curled up and of finite size in most of these models. It is distinguished between models where only gravity can propagate into the extra dimensions [38], which can be as large as $10\,\mu$m [39], and models with very small universal extra dimensions. In these models, the extra dimensional wave function component of all particles can be excited in analogy to a particle caught in an infinite deep potential pit. In this case, one could observe a spectrum of Kaluza–Klein eigenstates for each particle.

Theories like Technicolour or Topcolour try to avoid the hierarchy problem by explaining electroweak symmetry breaking without a Higgs boson. Instead of that, new particles and interactions occur at higher energies [40].

In principle, nothing in the standard model forbids the existence of a fourth generation of fermions but the LEP experiment has shown that even the neutrinos of this generation must have a mass higher than half the Z^0 mass. But also if this particles can not be produced directly in experiments, a measurement of the CKM-matrix elements can give a hint since the 3×3-submatrix of the first three generations would not be unitary anymore.

2.2 Proton–Proton Collisions

In contrast to lepton collisions where two point-like particles interact, the hard interaction between two protons is a more complicated process due to the complex internal structure of hadrons. The kinematic distribution of the quarks and gluons inside the proton has to be considered as well as the hard process between those partons itself in order to get to quantitative predictions. The formalism to do this is well described in [41].

Predictions for soft interactions between two protons are even more complicated since the interaction between the partons cannot be treated in perturbation theory. For such calculations, phenomenological descriptions are used.

2.2.1 Structure of the Proton

The inner structure of the proton is described by parton density functions (PDFs) $f_{\mathrm{a|p}}(x, Q^2)$, which give the probability to find a quark, respectively a gluon, a with the momentum fraction x at the momentum scale Q^2 inside the proton. Logarithmic corrections from collinear gluon emission are absorbed into the definition of the PDF in form of a scale dependence. The scale dependence is described by the DGLAP [42] equations

$$\frac{\partial f_{\mathrm{a|p}}(x, Q^2)}{\partial \log Q^2} = \frac{\alpha_{\mathrm{s}}}{2\pi} \int_x^1 \frac{dz}{z} \left\{ P_{\mathrm{aa'}}(z, \alpha_{\mathrm{s}})\, f_{\mathrm{a'|p}}(\frac{x}{z}, Q^2) \right\} \tag{2.8}$$

where the splitting functions $P_{aa'}(z, \alpha_{\mathrm{s}})$ give the probability that a parton a emits a gluon or quark and turns into another parton a' carrying a momentum fraction z. They can be calculated as perturbative expansions in α_{s}:

$$P_{\mathrm{aa'}}(z, \alpha_{\mathrm{s}}) = P^{\mathrm{LO}}_{\mathrm{aa'}}(x) + \frac{\alpha_{\mathrm{s}}}{2\pi} P^{\mathrm{NLO}}_{\mathrm{aa'}}(z) + \left(\frac{\alpha_{\mathrm{s}}}{2\pi}\right)^2 P^{\mathrm{NNLO}}_{\mathrm{aa'}}(z) + \ldots . \tag{2.9}$$

PDFs are fitted to data, which are gained from different experimental setups like deep inelastic scattering at HERA [44], fixed target experiments [45], or neutrino–nucleon scattering [46]. Figure 2.3 shows the MSTW PDFs of the different quark flavours and gluons at two different scales of Q^2. The density is at large values of the momentum fraction x dominated by the up and down valence quarks. Going to smaller values of x, the gluon density increases and becomes most important.

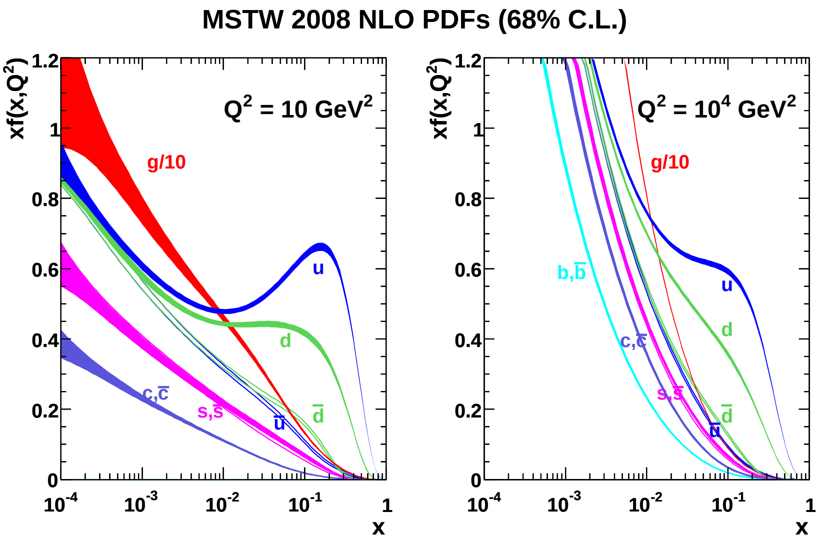

Figure 2.3: MSTW NLO PDFs at $\mathrm{Q}^2 = 10\,\mathrm{GeV}^{\,2}$ and $\mathrm{Q}^2 = 10^4\,\mathrm{GeV}^{\,2}$ [43].

2.2.2 Partonic Cross Section

The partonic cross section $\hat{\sigma}$ for a given process is calculated by integrating its squared matrix element over the available phase space. This has to be done numerically in most cases. Regions of the phase space where the matrix element diverges have to be avoided.

Taking into account only the leading order (LO) Feynman diagrams gives in most cases already a good estimate of the expected cross section. But due to the strong scale dependence of the strong interaction, a next-to-leading order (NLO) calculation is needed for reliable predictions. In general, a quantity calculated to a certain order of α_s does not depend on the scale up to the next higher order. The strength of the NLO calculation with respect to the LO order is quantified by a K-factor which is the ratio between the LO and NLO cross section.

The NLO corrections contain all diagrams, which contain an extra factor of α_s. This comprises virtual corrections as well as the radiation of real gluons before (initial state radiation) or after (final state radiation) the hard process. Some properties or distributions can only be modelled by going to next-to-leading order. For example, the transverse momentum of a top–antitop pair can only be non-zero if initial and final state radiation is taken into account.

2.2.3 Factorisation Theorem

The hard interaction between protons can be well described using the factorisation theorem by Drell and Yan [47]. It states that for a hard process the cross section σ_AB can be written as the convolution of the PDF $f_{\mathrm{a|A}}(x, \mu_\mathrm{F})$ of the proton and the cross section $\hat{\sigma}_{\mathrm{ab}\to\mathrm{X}}$ of the interacting partons. This theorem is true for the asymptotic scaling limit, i.e. the squared centre of mass energy s going to infinity while the ratio $\hat{s}/s$ remains fixed (with $\hat{s} = x_{\mathrm{a}}x_{\mathrm{b}}s$ being the squared centre of mass energy of the interacting partons). To calculate a physics quantity like the cross section in a certain order in α_{s}, one needs both the partonic cross section and the PDFs in the respective order. Considering the dependence of the PDFs on the factorisation scale μ_{F} and the the renormalisation scale μ_{R} of the hadronic cross section, the factorisation theorem reads

$$\sigma_{\mathrm{AB}} = \int dx_{\mathrm{a}}dx_{\mathrm{b}}\, f_{\mathrm{a}|\mathrm{A}}(x_{\mathrm{a}}, \mu_{\mathrm{F}}^2)\, f_{\mathrm{b}|\mathrm{B}}(x_{\mathrm{b}}, \mu_{\mathrm{F}}^2)\, \left\{\hat{\sigma}_{\mathrm{LO}} + \alpha_{\mathrm{s}}(\mu_{\mathrm{R}}^2)\hat{\sigma}_{\mathrm{NLO}} + \dots\right\}_{\mathrm{ab}\to\mathrm{X}} . \tag{2.10}$$

The resulting prediction depends on the choice of the scales if no higher order corrections are calculated. The scales are usually chosen to be of the order of magnitude of the momentum scale of the hard process.

2.2.4 Underlying Event and Pile-up

After the hard interaction has taken place, a remnant of both protons remains. Multiple interactions can occur, which means that two additional partons of the two protons do a hard interaction. The coloured fragments and particles from multiple interactions hadronise and create additional particles that are observed in the event. Everything from the proton–proton interaction that does not belong to the hard interaction of interest is summarised under the term *underlying event*. The underlying event does not depend on the luminosity of the collider in contrary to pile-up [48].

At higher luminosities, more than one proton–proton interaction can occur in one bunch crossing. This effect is called pile-up and gives additional background in the event. About twenty proton–proton interactions per bunch crossing are expected on average at the design luminosity of $10^{34}\ \mathrm{cm}^{-2}\,\mathrm{s}^{-1}$[49]. The luminosity during the first data taking was much lower. However, systematic errors due to pile-up events have to be taken into account for the analysis described here.

2.3 Physics of the Top Quark

Before the LHC era, the top quark was only observed at the CDF and DØ experiments at the Tevatron where it was discovered in 1995 [3]. Although some thousands of $t\bar{t}$ pairs have been produced at the Tevatron since then, the measurements of many quantities are still dominated by statistical errors. The LHC will with increasing luminosity soon be able to improve the results of the Tevatron and even permit to perform completely new measurements. This section summarises the experimental status of top physics based on Tevatron results and gives an outlook on measurements planned at the LHC.

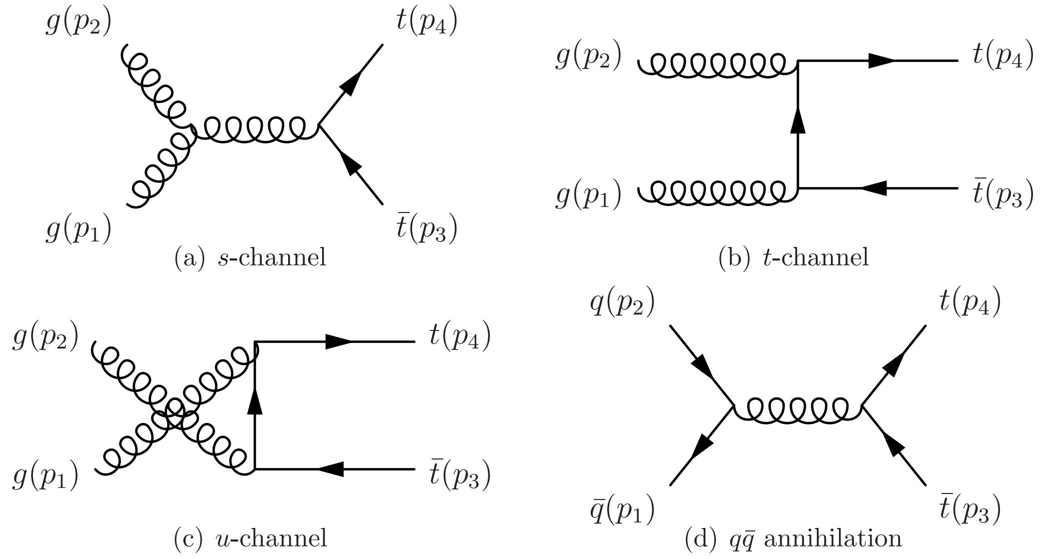

(a) s-channel (b) t-channel

(c) u-channel (d) $q\bar{q}$ annihilation

Figure 2.4: Leading order $t\bar{t}$ production diagrams.

2.3.1 Production

Top quarks are in hadron collisions predominantly produced as top–antitop pairs since the quark flavour is conserved in strong interactions. The main mechanisms are gluon–gluon fusion and quark–antiquark annihilation. The LO QCD diagrams for $t\bar{t}$ production are displayed in Figure 2.4. The corresponding matrix elements of the partonic cross section are

$$|\mathcal{M}_{gg\to t\bar{t}}|^2 = (4\pi\alpha_\mathrm{s})^2 \left(\frac{1}{6\tau_1\tau_2} - \frac{3}{8}\right)\left(\tau_1^2 + \tau_2^2 + \rho - \frac{\rho^2}{4\tau_1\tau_2}\right) \tag{2.11}$$

$$|\mathcal{M}_{q\bar{q}\to t\bar{t}}|^2 = (4\pi\alpha_\mathrm{s})^2 \left(\frac{4}{9}\right)\left(\tau_1^2 + \tau_2^2 + \frac{\rho}{2}\right) \tag{2.12}$$

with the abbreviations

$$\tau_1 = \frac{2\,p_1\cdot p_2}{\hat{s}}, \quad \tau_2 = \frac{2\,p_2\cdot p_3}{\hat{s}}, \quad \rho = \frac{4\,m_t^2}{\hat{s}}, \quad \hat{s} = (p_1+p_2)^2,$$

which are already averaged over all initial and summed over all final colour and spin states [50]. The high mass of the top quark, which is much larger than the QCD scale Λ, provides a cut-off that makes the calculation of the matrix elements in perturbative QCD applicable. It can further be concluded from the matrix elements that the top quarks are preferentially produced centrally and close in rapidity to each other with a transverse momentum that is typically comparable to the top mass.

To create a $t\bar{t}$ pair in hadron collisions, the centre of mass energy of the two interacting partons $\sqrt{\hat{s}}$ has to be at least twice the top mass i.e. about 350 GeV. For this reason, only two partons with high momentum fractions $x_{\mathrm{a,b}}$ fulfilling

$$\sqrt{x_\mathrm{a} x_\mathrm{a}} > \frac{350\,\mathrm{GeV}}{1.96\,\mathrm{TeV}} \approx 0.2 \tag{2.13}$$

can create a pair of top quarks at the Tevatron where 1.96 TeV is the centre of mass energy. As illustrated in Figure 2.3, the PDFs are dominated by the valence quarks at such high momentum fractions so that quark–antiquark annihilation is the dominating production process with a contribution of about 85%. Going to higher centre of mass energies, this ratio turns around. Because the higher energy allows $t\bar{t}$ production also at smaller values of x and because the gluon density increases steeply going to smaller values, the gluon–gluon fusion becomes overriding. It is expected that at the LHC about 90% of the $t\bar{t}$ pairs are produced in gluon–gluon fusion. Also, the LO cross section increases as can be seen in Figure 2.5.

The NLO corrections to the cross section are large for gluon–gluon fusion, so $t\bar{t}$ production at the LHC has a big K-factor. At 7 TeV and with a top mass of 173 GeV, the calculated LO cross section is 94 pb while the value for the NLO cross section is 155±20 pb. The most precise calculation, which is approximately in NNLO, is 165±10 pb [51].

Single top quarks can be produced via the weak interaction. The LO diagrams are shown in Figure 2.6. In the upper two diagrams, a virtual $W^{\pm}$ is exchanged in the s-channel and t-channel and the top quark is produced together with a bottom quark. Both production channels have already been observed at the Tevatron [52]. At the LHC, the the t-channel graph becomes predominant and has a NLO cross section of 62 pb [53] at $\sqrt{s} = 7\,\text{TeV}$. The associated production with an on-shell $W^{\pm}$, which is expected to have a very small cross section of ~ 0.1 pb at the Tevatron, has not been observed yet. The calculated NLO cross section for tW production at the LHC at $\sqrt{s} = 7\,\text{TeV}$ is 10 pb and should be observable and also has to be taken into account as an important background processes for $t\bar{t}$ production.

2.3.2 Decay Channels and Branching Ratios

The only possible decay of the top quark in the standard model is into a down-type quark and a W boson. The branching fractions for the different quark flavours is given by the CKM-matrix. Assuming its unitarity, $|V_{tb}|^2$ is close to one, so most top quarks decay into bottom quarks. Because of the high mass, the top decay is the only quark decay where the W boson is on-shell. The total decay width is given by

$$\Lambda_{t\to bW} = \frac{G_{\mathrm{F}} m_t^3}{8\pi\sqrt{2}} |V_{tb}|^2 \approx 1.74\,\text{GeV} \tag{2.14}$$

assuming a top mass of 173 GeV and $V_{tb} \approx 1$. Because G_{F} contributes to the total width only in the first power and because of the high top mass, the lifetime of the top quark is of the order of 10^{-25} s. This is about one order of magnitude shorter than the time scale on which hadronisation happens. Therefore, there exist no hadrons containing top quarks although strong interaction may have an influence on the final state [50].

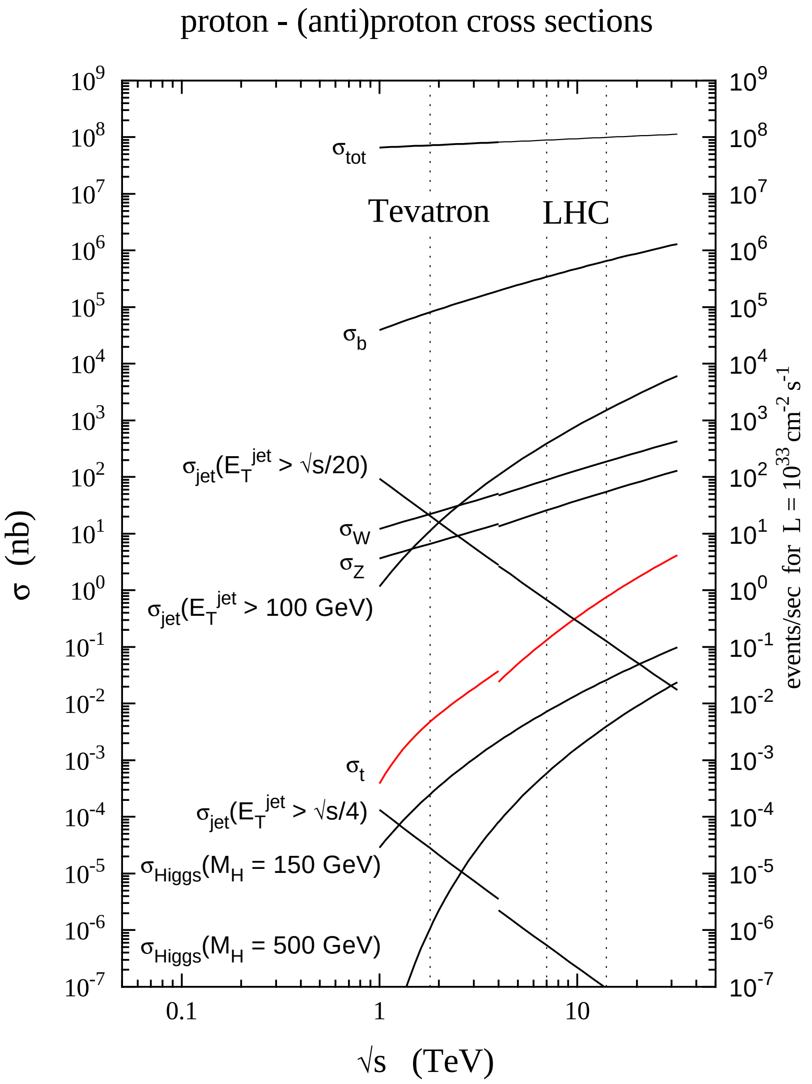

Figure 2.5: The LO cross sections of some standard model processes are displayed as functions of the centre of mass energy $\sqrt{s}$. The dashed vertical lines mark the energies of the Tevatron at 1.96 TeV and the LHC at 7 TeV and the design maximum energy of 14 TeV.
The gap at $\sqrt{s} = 4$ TeV is due to the fact that the cross sections at lower energies are extrapolated for $p\bar{p}$-collisions while those at higher energies are calculated for pp-collisions [54].

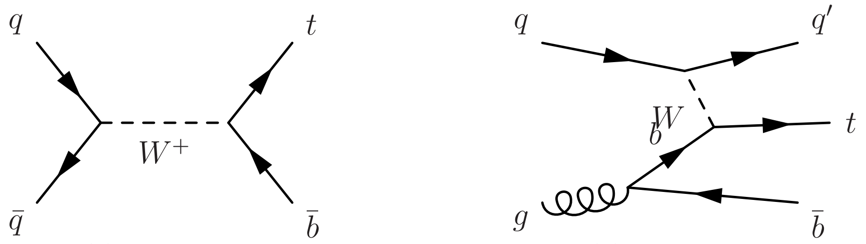

(a) s-channel (b) t-channel

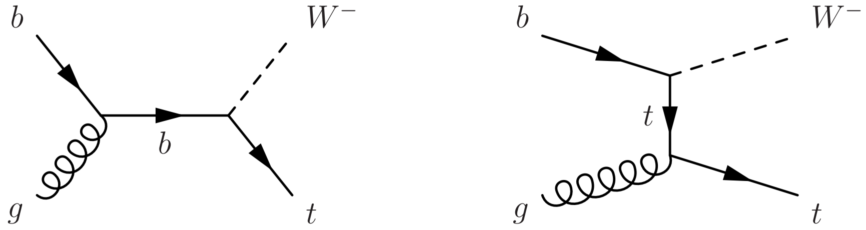

(c) associated tW production in the s-channel (d) associated tW production in the t-channel

Figure 2.6: Leading order single top production diagrams.

Decays of $t\bar{t}$ pairs are classified solely by the decay modes of the two W bosons. The allowed decays are into a lepton (e, μ, τ) and a corresponding neutrino or into two quarks (ud' or cs'). All channels have in leading order the same probability whereas the hadronic modes have to be counted trice because of the three different colour states. From this it follows, that the decays where both W bosons decay leptonically have a branching fraction of about 1/9 and in particular the dimuon channel has a ratio of about 1/81. The exact resulting branching ratios for $t\bar{t}$ pairs, which have been measured from W decays, are given in Table 2.2.

2.3.3 Top Mass

The experimental value of the top mass published by the Tevatron experiments is the value of the invariant mass peak which is gained by combining the four-momenta of the bottom and the W boson. However, it is not obvious how this measured mass has to be interpreted. The masses of the lighter quarks given in Table 2.1 are short distance masses $\overline{m}$ calculated in the $\overline{\text{MS}}$ scheme which depend on the scale μ on which they are evaluated. This is useful as long as the characteristic scale of the process is given by the momentum scale and is large compared to the quark masses [55].

It has to be distinguished between this $\overline{\text{MS}}$ mass and the on-shell pole mass m_{pole}, which is the real part of the complex pole in the quark propagator. A complication is the fact that the confinement of the quarks implies that there is no pole in the full propagator but only in a finite order of perturbation theory. Furthermore, the pole mass has a theoretical uncertainty of the order of Λ because of non-perturbative QCD effects [56].

decay	r [%]	decay	r [%]
$\ell\ell$	10.50 ± 0.12	ee	1.16 ± 0.02
		$\mu\mu$	1.12 ± 0.02
		$\tau\tau$	1.27 ± 0.03
		$e\mu$	2.27 ± 0.04
		$e\tau$	2.42 ± 0.05
		$\mu\tau$	2.38 ± 0.05
ℓ+hadrons	43.80 ± 0.40	e+hadrons	14.53 ± 0.19
		μ+hadrons	14.29 ± 0.21
		τ+hadrons	15.21 ± 0.28
all hadrons	45.70 ± 0.26		

Table 2.2: $t\bar{t}$ branching ratios calculated from the W branching fractions that are taken from [10]

.

Since the difference is believed to be small, it is common to identify the experimental mass m_{exp} reconstructed from kinematic variables with the pole mass. The $\overline{\text{MS}}$ mass evaluated at the scale $\mu = \bar{m}$ is about 10 GeV lower [57].

2.3.4 Impact on the Higgs Boson Mass

One point that makes the measurement of the top mass so important is that the masses of the particles are not independent of each other but rather connected via radiative corrections. High precision measurements of the W and top mass can therefore help to constrain the mass of the Higgs boson. The interrelation of the weak quantities is given by

$$G_{\text{F}} = \frac{\pi\alpha}{\sqrt{2}\, m_W^2 \sin^2 \vartheta_{\text{W}}} \frac{1}{1 - \Delta r} \tag{2.15}$$

where Δr summarises the higher order radiative corrections [58] [59]. These corrections can be calculated in perturbation theory and can be written in the form

$$\Delta r = \Delta\alpha + \cot\theta_{\text{W}} \Delta\rho + \dots \tag{2.16}$$

where $\Delta\alpha$ is a correction to the running coupling and $\Delta\rho$ is given by loop corrections to the W self-energy as displayed in Figure 2.7.

The loop correction as shown in Subfigure 2.7(a) of course regard to all doublets of fermions ff' but according to [60] the contribution is given by

$$\Delta\rho_f = \frac{3G_{\text{F}}}{8\pi^2\sqrt{2}} \left(m_f^2 + m_{f'}^2 - 2\frac{m_f^2 m_{f'}^2}{m_f^2 - m_{f'}^2} \ln \frac{m_f^2}{m_{f'}^2} \right) \tag{2.17}$$

so the top–bottom pair gives the largest contribution because of the large top mass. In the approximation $m_t^2 \gg m_b^2$ it becomes

$$\Delta\rho_t \approx \frac{3G_{\text{F}}}{8\pi^2\sqrt{2}} m_t^2. \tag{2.18}$$

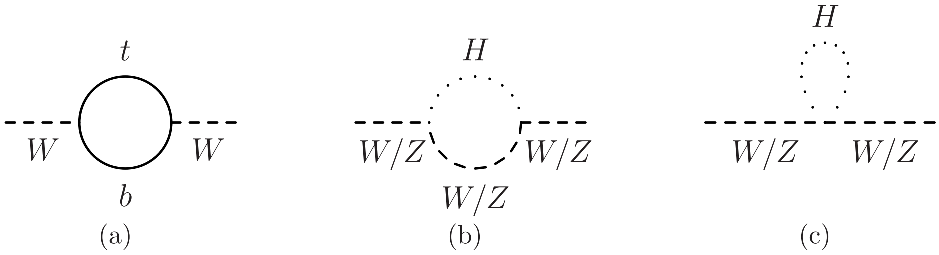

Figure 2.7: Corrections to the W self-energy involving the top quark and the Higgs boson.

The Higgs contributions in Figure 2.7(b) and 2.7(c) give rise to a correction

$$\Delta\rho_H = -\frac{3G_\mathrm{F}}{8\pi^2\sqrt{2}}(m_Z^2 + m_W^2)\left(\ln\frac{m_H^2}{m_W^2} - \frac{5}{6}\right). \tag{2.19}$$

The interdependence between m_t, m_W, and m_H given in the above equations is graphically displayed in Figure 2.8. A fixed value of the Higgs mass m_H in the standard model defines a straight line in the $m_t - m_W$-plane. The area labelled as SM shows the allowed range for the masses of the W and the top for a Higgs mass between 114 GeV and 400 GeV. The outer blue ellipse shows the today's measured values of m_W and m_t with a confidence level of 90%. The black ellipse demonstrates how with the LHC the results can be refined in the future. A future lepton collider could improve the measurement as illustrated by the most inner red ellipse by exploring W and top production at its threshold.

As can be seen in the figure, the actual data agree best with a small Higgs mass close to or even below 114 GeV, the lower limit set by LEP for the direct Higgs search. The result of a standard model fit including all corrections is displayed in Figure 2.2 and indicates also a most probable value in the LEP-excluded mass range. The different fit curves correspond to different sets of input data [34]. In a supersymmetric theory with more contributing processes and free parameters, the allowed area for the Higgs mass is shifted. This is displayed by the upper area shaded in green. There is also a small region in which both theories are possible.

2.3.5 Influence on BSM Searches

The top quark plays a role for the experimental searches and proofs in many extensions of the standard model. In particular, the question arises if the top quark itself is in some way responsible for this symmetry breaking as theories like Topcolor and composite Higgs models suggest because the top mass is close to the scale of the electroweak symmetry breaking [40]. But also for the search of a hypothetical fourth generation, the study of top quark decays can serve as a useful tool. Although decays into exotic particles would affect the physical width of the top, this circumstance can not be used to search for new

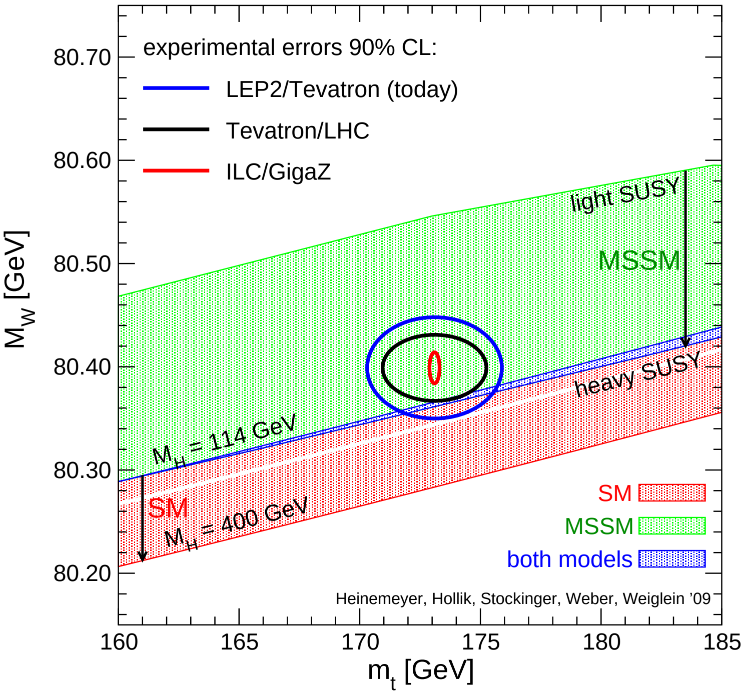

Figure 2.8: Measured W mass vs. top mass and anticipated precision for present (Tevatron, LHC) and future (ILC/GigaZ) experiments [61].

physics since the width of the top quark is dominated by the experimental resolution, at least in hadron collisions.

At the Tevatron where protons and anti-protons are collided, a forward–backward asymmetry of the $t\bar{t}$ production is predicted by the standard model which can be measured [62]. A hypothetical Z' resonance decaying into a $t\bar{t}$ pair would change this asymmetry. The measurement at the LHC, which is a proton–proton machine, is more complicated but also possible. If a $t\bar{t}$ pair is created in quark–antiquark annihilation, the pair is usually boosted into the direction of the ingoing quark since the quark is in most cases a valence quark while the antiquark is always a sea quark [63]. A resonance could also show up as a bump in the invariant mass spectrum of $t\bar{t}$ pairs [57]. A Z' occurs e.g. in Topcolor theories where it interacts with quarks of the third generation and is 'leptophobic' while a Z' as a Kaluza–Klein excitation of the standard model Z^0 would also decay into leptons and could be found more easily in dilepton events. Heavy neutral resonances are predicted also in supersymmetric models and could be found in the same way.

In the same theories that deal with Z' bosons also W' bosons can exists. These could well be detected in the analysis of single top quark production. If these bosons exist, they contribute to all of the single top production graphs shown in Figure 2.6 where they can replace, respectively interfere, with the normal standard model W boson. In the s-channel, the interference between W and W' could in principle increase as well as decrease the cross section for single top production whereas the models under study predict an increasing cross section [64]. The invariant mass of the top and the bottom quark would show a resonant increase near the W' mass. In contrast, the exchange of a W' with a high mass can be neglected in the t-channel because these contribution would be suppressed by $1/M_{W'}^2$. If enough centre of mass energy is available, a on-shell W' could even be produced, as illustrated in the two lower diagrams in Figure 2.6.

The existence of a fourth generation mixing with the third one would also strongly affect the production of single top quarks since all production graphs contain a Wtb vertex with a coupling proportional to $|V_{tb}|^2$. In such a model, $|V_{tb}|^2$ would significantly deviate from unity, so the cross section for single top quarks would be lower than in standard model calculations. On the other hand, a high value for $|V_{ts}|^2$ could also be possible in a model with four generations leading to a higher cross section in the t-channel. $|V_{tb}|^2$ is also measured in $t\bar{t}$ pair production by comparing the measured cross section in analysis with and without b tagging to get the fraction of top quarks decaying into light flavour quarks.

It is also possible to look for new physics in top quark decays. Today's data still allow a branching ratio into exotic particles with up to some percent [57]. These exotic decays could produce e.g. charged Higgs bosons or other particles that appear in supersymmetric theories. It is also looked for flavour changing neutral current decays like $t \rightarrow Zc$, which is forbidden in the standard model.

2.3.6 Experimental Results at the Tevatron

The Tevatron publications [3] that stated the discovery of the top quark and gave a rough cross section estimate and a first mass measurement were based on a few tens of events in $\mathcal{O}(100)\,\mathrm{pb}^{-1}$ of data. Mainly lepton plus jet events had been selected but also a few dilepton events. Since then, both experiments have recorded about 10 fb^{-1} and all decay channels have been exploited. This subsection gives an overview about the latest and most precise results.

Cross Section CDF has published a value for the $t\bar{t}$ production cross section based on $4.6\,\mathrm{fb}^{-1}$ of data [65]. It is a best linear unbiased estimate calculated from four separate measurements in the dileptonic, fully hadronic and single lepton channel, where the single lepton channel has been analysed with two complementary methods using different properties of $t\bar{t}$ events. One analysis used topological properties of the events, the other one a secondary vertex algorithm for b tagging. The resulting combined result is

$$\sigma_{t\bar{t}} = 7.50 \pm 0.48\,\mathrm{pb} \tag{2.20}$$

assuming a top mass of 172.5 GeV. The result depends on the top mass because the detector acceptance increases with a higher mass.

Figure 2.9 shows the results for the single measurements and the combined results and also a comparison to theoretical predictions. As can be seen, these are in good agreement with the data.

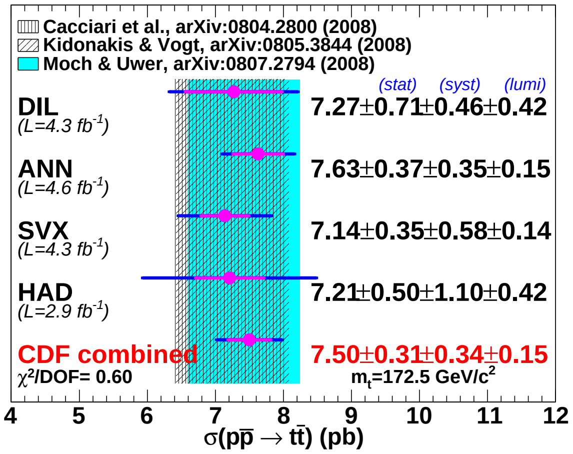

Figure 2.9: Top quark cross sections from CDF [65].

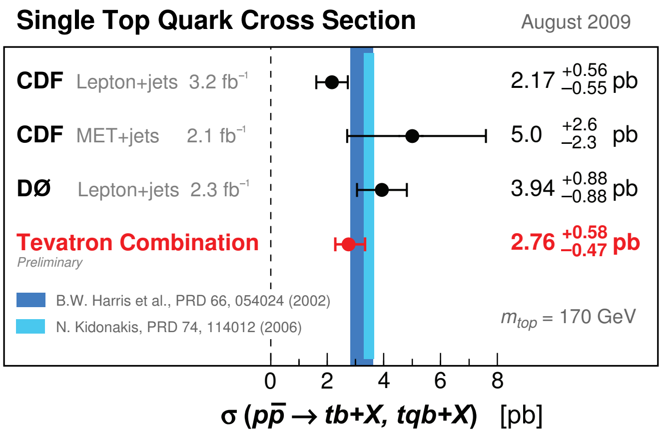

Figure 2.10: Combined single top production cross section [66].

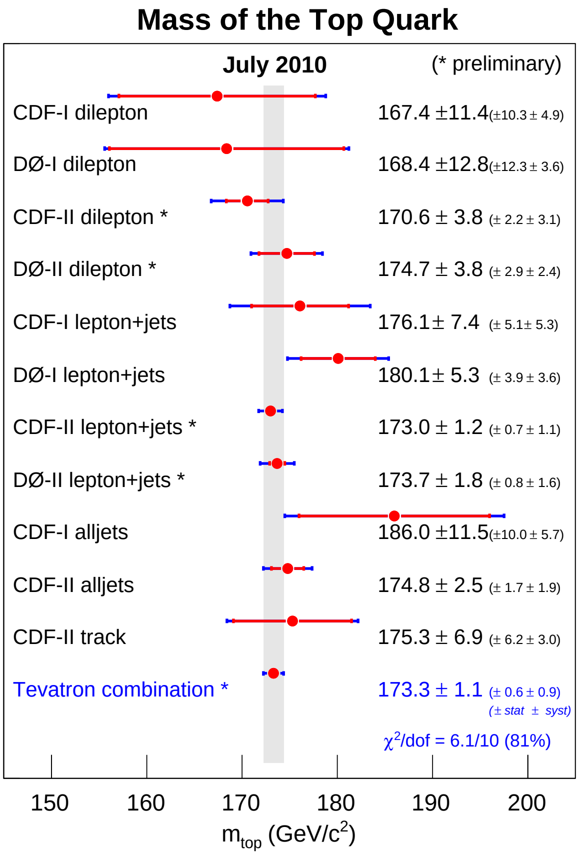

Figure 2.11: Top mass measured by the Tevatron experiments. The values and their errors are shown separately for both experiments, both run periods, and different decay channels. The combined value of all measurements is dominated by systematic errors.

A corresponding combined value exists also for single top production [66]. The combined result which is displayed in Figure 2.10 is

$$\sigma_t = 2.76^{+0.58}_{-0.47}\,\mathrm{pb} \tag{2.21}$$

assuming a top mass of 170 GeV. Attempts to measure the cross section for single top production in the s-channel and t-channel separately still have large errors since both processes are hard to distinguish from each other [67]. Associated production of top quarks and W bosons has not been observed yet.

Mass The top mass has been measured in all decay modes. The results are shown in Figure 2.11. The combined value [68] calculated from eleven separate measurements in a similar way as for the cross section is

$$m_t = 173.32 \pm 0.56\,(\mathrm{stat.}) \pm 0.89\,(\mathrm{syst.})\,\mathrm{GeV}. \tag{2.22}$$

While in the fully hadronic and single lepton case a kinematic fit can be applied, in the dilepton channel further assumptions are needed, e.g. [69] or [70]. Since the systematic errors of all traditional measurement techniques are dominated by the jet energy scale, at CDF also a method has been used that determines the top mass from the lepton momentum and the average b decay length similar to the method described in [71].

Charge Although all quarks in the standard model have a charge of -1/3 e or +2/3 e, the combination of a W and a b jet also allows an exotic charge of -4/3 e for the top quark since it is non-trivial which W to combine with which b jet. The study [72] discriminates the b and $\bar{b}$ jet by measuring the charges and momenta of the tracks inside the jet cones. The exotic charge could be excluded with at a confidence level of 92%.

Forward–Backward Asymmetry The Tevatron is a proton–antiproton collider, so a forward–backward asymmetry $A_{\mathrm{FB}} = (N_{\mathrm{F}} - N_{\mathrm{B}})/(N_{\mathrm{F}} + N_{\mathrm{B}})$ of the $t\bar{t}$ production can be defined. The observable is the difference $\Delta\eta = \eta_t - \eta_{\bar{t}}$ of the pseudorapidities $\eta = -\ln(\tan(\vartheta/2))$ of the top and the antitop quark. NLO effects lead to a value different from zero. The measured value of $A_{\mathrm{FB}} = 0.42 \pm 0.15 \text{ (stat.)} \pm 0.05 \text{ (syst.)}$ at the CDF experiment is higher than the predicted standard model value of 0.088 [73].

Production mechanism There are several approaches to get information about the $t\bar{t}$ production mechanism. The first method makes use of the fact that the spin of the top and antitop quark are strongly correlated. Depending on the production mechanism, the angular momentum state of the $t\bar{t}$ pair is ${}^3S_1$ for $q\bar{q}$ annihilation, respectively ${}^1S_0$ for gluon–gluon fusion. Because the top quark decays before it can hadronise, the spin information is conserved and can be observed in the angular distribution of the top's decay products. Large statistics are needed to get reasonable results using this method.

The other approach is to distinguish between the two production mechanisms by the fact that in gluon–gluon events the number of low-momentum tracks is expected to be higher than in $q\bar{q}$ events. The combined result of both methods is that the fraction of gluon created top pair events is $0.07^{+0.15}_{-0.07}$ which is in agreement with the prediction of 0.15 ± 0.05 [74].

CKM-Matrix element V_{tb} Two different approaches for the measurement of V_{tb} exist. One is to compare the measured cross sections for $t\bar{t}$ production with and without b tagging. This requires of course a good understanding of the b tagging performance. The second method used at the Tevatron is to compare the measured cross section for single top production in the s- and t-channel with the cross section calculated from QCD where V_{tb} is kept as a free parameter. Since the single top measurements are still dominated by large statistical errors, the first method provides the more meaningful result. A value of $|V_{tb}| > 0.89$ is found at 95% confidence level [75].

Chapter 3

The Experiment

3.1 Large Hadron Collider

3.1.1 Accelerator

The Large Hadron Collider (LHC) [77] is a proton–proton and heavy-ion collider at CERN near Geneva. It is constructed in the tunnel of the former LEP collider which has a circumference of 26.7 km and lies between 45 m and 170 m below the surface. It is designed to accelerate protons to an energy of up to 7 TeV at a maximum luminosity of $10^{34}\,\mathrm{cm}^{-2}\,\mathrm{s}^{-1}$.

At the nominal energy, a magnetic field of more than 8 T is needed to keep the proton beams in their orbit. Superconducting dipole magnets that are cooled with helium are used to achieve this. An important difference to former superconducting accelerators like HERA, Tevatron, or RHIC, which are all run just below 4.2 K, the LHC makes use of the larger heat conductance of superfluid helium II and therefore has to be run at a temperature below 2 K.

To save space in the preset tunnel that has an inner diameter of only 3.7 m, the twin-bore-magnet technique is used, i.e. both beam pipes are embedded into the same magnets. This has the advantage of saving costs and space at the detriment of a lower flexibility to steer the beams since they are magnetically coupled.

Although the LHC is designed to achieve a maximum centre of mass energy of $\sqrt{s} = 14$ TeV for proton–proton collisions, the first longer run period in 2010 was performed at only 3.5 TeV energy per beam corresponding to a centre of mass energy of $\sqrt{s} = 7$ TeV. This was done for safety reasons, especially to avoid magnet quenches, which could damage the machine. Attempts to achieve the nominal energy are planned to be made after a longer maintenance and upgrade shutdown in 2013.

The luminosity $\mathcal{L}$ of a collider machine is defined by the ratio of the rate dN/dt of a process and its cross section σ:

$$\frac{dN}{dt} = \mathcal{L} \cdot \sigma. \tag{3.1}$$

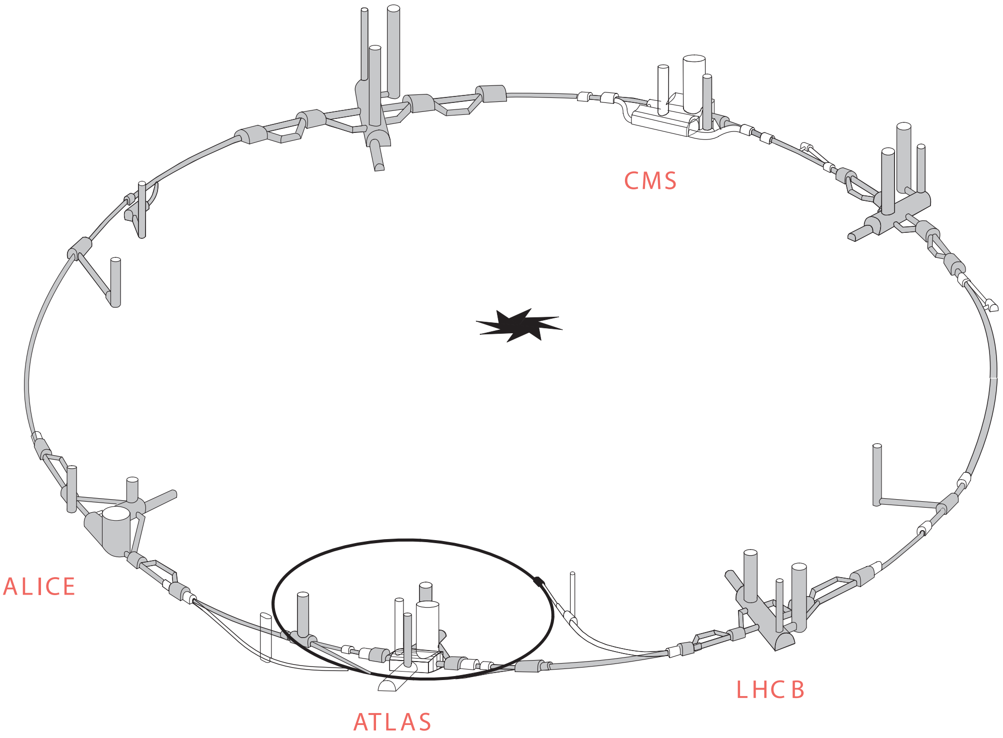

Figure 3.1: Schematic illustration of the Large Hadron Collider [76].

Integrating this over time gives the integrated luminosity

$$L = \int dt\, \mathcal{L} = \frac{N}{\sigma}. \tag{3.2}$$

From the technical point of view the luminosity can also be written as

$$\mathcal{L} = \frac{N_b^2\, n_b\, f \gamma}{4\pi\epsilon_n\, \beta^*} F \tag{3.3}$$

with N_b being the number of protons per bunch, n_b the number of bunches per beam, f the revolution frequency, the relativistic factor $\gamma = 1/\sqrt{1 - v^2/c^2}$, ϵ_n the normalised transverse beam emittance, β^* the value of the accelerator's β-function at the interaction point, i.e. the focusing of the beam in that point, and F a geometric factor which reduces the luminosity. F is given by the size and shape of the beams and their crossing angle.

The technical parameters, especially the number of bunches, lay during the first data taking substantially below the design values. The luminosity was slowly increased up to a maximum value of $2 \cdot 10^{32}\,\mathrm{cm}^{-2}\,\mathrm{s}^{-1}$ which is still much below the design luminosity of $10^{34}\,\mathrm{cm}^{-2}\,\mathrm{s}^{-1}$.

Figure 3.1 shows an illustration of the LHC accelerator with its four main experiments. The black ring at the bottom side of the picture illustrates the Super Proton Synchrotron SPS which serves as preaccelerator for the LHC and accelerates the protons to the LHC injection energy of 450 GeV.

3.1.2 Experiments

The LHC experiments are situated in four caverns along the LHC tunnel. The ALICE [78] and LHCb [79] experiments use the caverns of the former L3 and DELPHI experiments at LEP. For the ATLAS [80] and CMS [81] experiments new, larger caverns had to be excavated. The forward physics experiments LHCf [82] and TOTEM [83] are located in the same caverns as ATLAS and CMS respectively.

The ATLAS detector is a multipurpose detector and with a length of 44 m and a diameter of 25 m by its spacial dimensions the largest of the experiments. The detector design is in many aspects complementary to the design of CMS. The magnetic field is generated by large toroid magnets and only one small solenoid. The most important advantage of ATLAS over CMS is the much better energy resolution of the hadronic calorimeter, however the momentum resolution of the tracking detectors is worse.

While most of the LHC experiments are optimised to analyse proton–proton collisions, the ALICE detector is optimised for high track multiplicities from heavy-ion collisions. Additionally to a silicon pixel detector and a transition radiation detector, a time projection chamber is used that can resolve many tracks in one event but is not designed for the high event rates which are achieved in proton collisions.

The LHCb experiment is designed for the study of heavy-flavour physics, especially CP violation and rare charm and beauty meson decays. In contrary to the experiments described above, the LHCb detector is a one-arm spectrometer that covers only a small angle in one direction along the beam line. At the LHC centre of mass energy charm and beauty mesons are predominantly produced in the forward and backward directions with small angles with respect to the beam line.

The physics goal of the LHCf experiment is to improve the understanding of hadron interactions at very high energies, which is needed to calibrate Monte Carlo simulations of high energy cosmic radiation. The experiment consists of two calorimeters installed 140 m downstream in both directions from the ATLAS interaction point.

TOTEM is also an experiment designed for forward physics and technically integrated into the CMS experiment. Its main goal is a luminosity independent measurement of the total proton–proton cross section based on the optical theorem.

3.2 Compact Muon Solenoid Detector

The Compact Muon Solenoid (CMS) experiment [81] is a multi-purpose detector and, with a length of 21.6 m and a diameter of 14.6 m, by its volume much more compact than the ATLAS detector although its mass of about 12 500 tons is much larger. A schematic overview of the apparatus and most of its

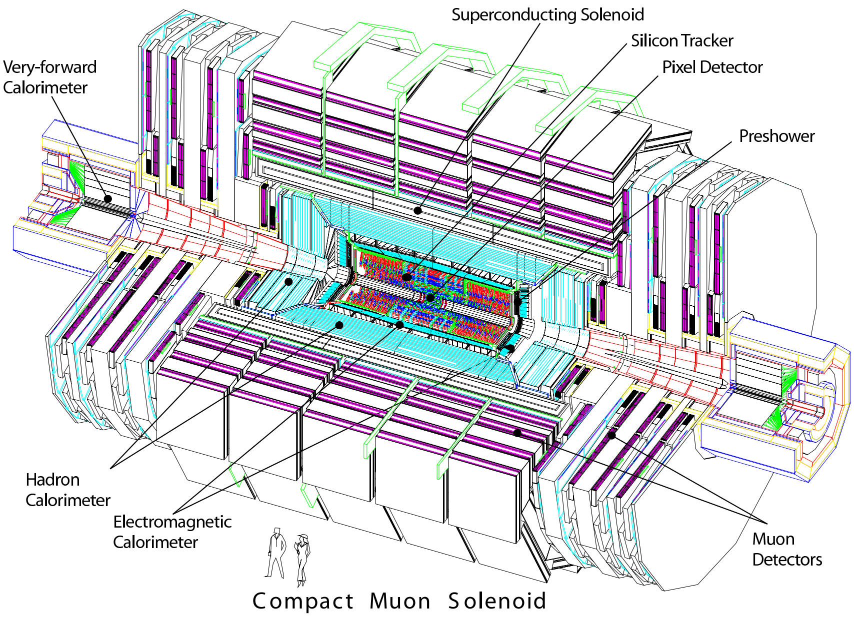

Figure 3.2: The CMS detector.

subdetector components is shown in Figure 3.2. The name-giving component of CMS is the 13 m long superconducting coil which generates a magnetic field of up to 4 T parallel to the beamline and homogeneous over the whole volume of the tracking detector. During the data taking in 2010, the magnet was run at 3.8 T. Because of the Lorentz force, the magnetic field bends the tracks of charged particles in the plane perpendicular to the beamline, so their transverse momenta can be measured using the relation $R = p/eB$ between the track radius R, the momentum p, and the magnetic field B. The return flux of the magnetic field is led through an iron yoke, which is instrumented with the outer muon detectors. This iron yoke makes up by far the largest contribution to the detector's mass. It consists of five barrel rings around the coil and three endcap discs on each side. Its total mass is about 10 000 t. The silicon tracking detectors and the largest part of the calorimeter system are installed in the coil's inner bore with a diameter of 5.9 m. The calorimeters for the very forward direction, CASTOR and ZDC, are not displayed in Figure 3.2.

CMS uses a coordinate system with the origin at the nominal interaction point in the centre of the detector, in which the x-axis points horizontally inwards to the centre of the LHC ring and the y-axis points upwards. Hence, the z-axis is parallel to the beam axis at the interaction point with the positive direction in the anti-clockwise direction of the ring. The angle ϕ is defined as the angle in the x-y plane starting from the x-axis. The angle ϑ is defined as the angle to the positive z-axis. Also in the following the transverse distance from the z-axis is denoted with r.

Most of the subdetectors consist of a barrel part installed cylindrically around the beam axis to detect particles with small absolute values of the pseudorapidity $\eta = -\ln(\tan(\vartheta/2))$ and an endcap on each side for particles at

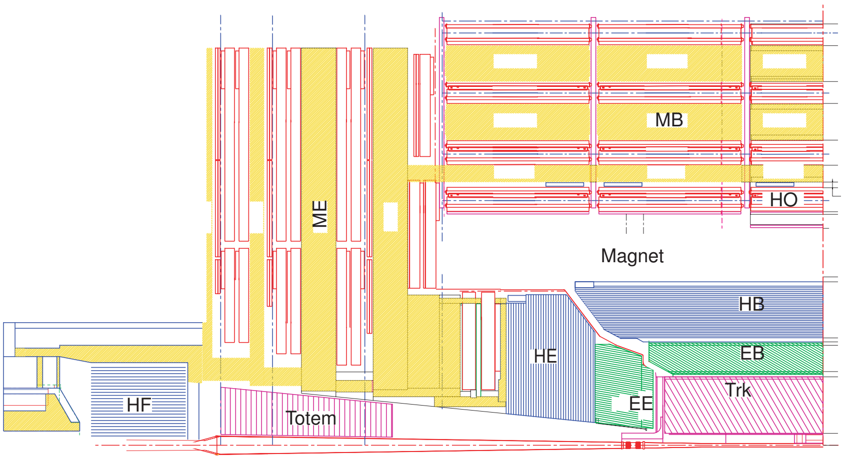

Figure 3.3: Cut through a quadrant of the CMS detector in the r-z plane with its most important subsystems. The tracker (Trk), the barrel (EB) and endcap (EE) of the electromagnetic calorimeter, and the barrel (HB) and endcap (HE) of the hadronic calorimeter are located inside the magnet coil. Further hadronic calorimeters are the HO encompassing the magnet and the forward calorimeter HF. In front of the later one a tracking detector of the TOTEM experiment is installed. Also the muon system consists of a barrel (MB) and endcaps (ME).

higher η. In Figure 3.3 a cut view through a quadrant of the detector is shown. The components which are important for the top analysis are described in the following in more detail starting from the interaction point and going outward.

3.2.1 Silicon Tracking System

Several requirements had to be taken into account for the tracking detector of the CMS experiment. Because of the high track multiplicities of up to $\mathcal{O}(1000)$ particles per bunch crossing at the design luminosity, the detector has to have a fine granularity. The high frequency of the bunch crossings of 40 MHz makes a fast response and readout of the detector necessary. For this reason, the whole tracking system is implemented using silicon detector technology. An efficient cooling is needed for the electronics directly installed on the silicon chips, which leads to a high material budget in the tracking detector. Because too much material in the tracking detector is adverse for the measurement of particles, a compromise between granularity and material budget had to be found. Also, potential damages due to radiation directly from the beam–beam interactions had to be considered in the tracker design.

The layout of the CMS tracking system is displayed in Figure 3.4. Next to the interaction point, the silicon pixel detector is installed around the beam pipe. It consists of three cylindrical layers of silicon in the barrel region with radii between 4.4 cm and 10.2 cm and two layers in each endcap mounted as

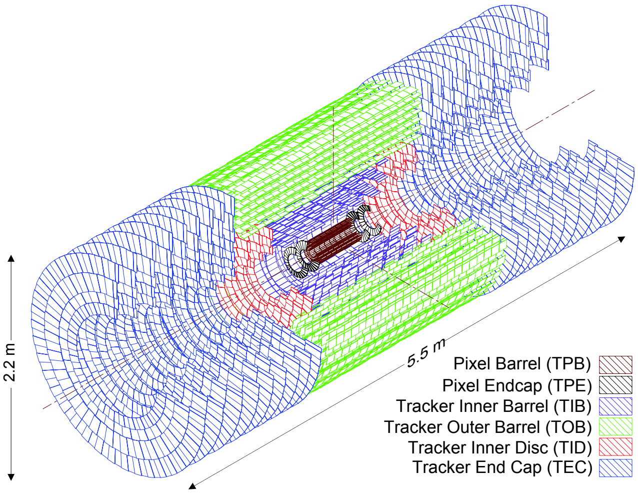

Figure 3.4: The CMS tracking system.

discs perpendicular to the z-axis. he pixel detector is composed of 1440 pixel modules with 66 million pixels in total.

The silicon strip detector is installed around the pixel detector and consists of 15 148 silicon strip modules. Like the pixel detector, the strip detector consists of barrel layers in the central region and discs in the r-ϕ plane in the endcaps. Furthermore, the strip detector is divided into inner and outer subdetectors. The inner part of the tracker barrel (TIB) consists of four layers where the inner two are double layers. The endcaps (TID) of the inner part of the strip tracker consist each of three discs. The radius of the inner detector extends up to 55 cm. The outer barrel (TOB) comprises six layers of silicon strips up to a radius of 110 cm. Also here, the inner two layers are double layers. The tracker endcaps (TEC) have nine discs on each side. The overall length of the tracking detector is 5.5 m. It covers the whole solid angle up to $|\eta| = 2.5$, whereby tracks with $|\eta| > 2.4$ cross only few layers.

The silicon pixels achieve a spatial resolution of 15–20 μm. The resolution in the strip detector is a little lower but still about the same order of magnitude. The momentum resolution of tracks is of the order of 1% for tracks with a momentum of 100 GeV. For tracks from particles below 1 TeV the charge of the particle can be identified unambiguously. Even before the first collisions the alignment of the tracking detector was calibrated using muons from cosmic radiation during several cosmic ray runs [84]. For this reason even in the very first collision data the alignment was well understood. Plots showing the performance of b tagging are shown later in this work.

3.2.2 Electromagnetic Calorimeter

The next subdetector enclosing the tracking system is the electromagnetic calorimeter ECAL. The barrel part EB covers the pseudorapidity range $|\eta| <$

1.479, the endcaps EE the range $1.479 < |\eta| < 3.0$. The ECAL consists of 75 848 lead tungstate ($PbWO_4$) crystals which serve as absorber as well as scintillator. Each crystal covers a solid angle of $(\Delta\eta, \Delta\phi) = (0.0174, 0.0174)$. The advantage of using this material is the short radiation length of only 0.89 cm and a small Molière radius of 2.2 cm resulting in a fine granularity. Also, the scintillation decay time is short enough to separate showers originating from different bunch crossings since about 80% of the scintillation light is emitted within 25 ns. This light, which is emitted in the visible spectrum with a maximum between 420 and 430 nm, is detected by avalanche photodiodes in the barrel part and vacuum phototriodes in the endcaps. The total thickness of the ECAL is more than 25 radiation lengths X_0.

In front of the endcaps, the preshower detectors are installed covering an angle of $1.653 < |\eta| < 2.6$. These are sampling calorimeters that have the main purpose to identify neutral pions but also improve the position measurement of electromagnetic showers from electrons and photons. For this purpose, each layer is equipped with silicon strip sensors.

The resolution of the ECAL is given by

$$\left(\frac{\sigma}{E}\right)^2 = \left(\frac{2.8\%}{\sqrt{E}}\right)^2 + \left(\frac{0.12}{E}\right)^2 + (0.30\%)^2 \tag{3.4}$$

with the energy given in GeV. The first term is a stochastic term, the second one is due to noise from the electronics, digitisation or pile-up, and the constant term arises from leakage of energy, non-uniformity of the light collection and calibration errors.

3.2.3 Hadronic Calorimeter

The hadronic calorimeter system HCAL consists of the barrel (HB), the endcaps (HE), the outer barrel (HO), and the forward calorimeters (HF). The position of all these subsystems is displayed in Figure 3.3. The HB is located between the ECAL barrel and the magnet, which constrains the available space. The thickness of the absorber material in the central region at $\eta = 0$ sums up to only 5.82 hadronic interaction lengths λ_I. With larger pseudorapidities, the thickness increases with $1/\sin\vartheta$ and reaches about 10 λ_I at the rim of the barrel at $\eta = \pm 1.3$. The material of the ECAL crystals adds further 1.1 interaction lengths. The thickness of the HE is also around 10 λ_I. It covers the the solid angle in the range $1.3 < |\eta| < 3.0$. The HF extends the range of the HCAL to $|\eta| = 5.2$. Because of the low material budget in the very central region, the HO is installed outside the magnet as tail catcher to detect hadrons that cross the HB and even punch through the magnet from late starting hadron showers. It increases the thickness to more than 10 radiations lengths except of a small gap between the HB and HEs.

The barrel is organised in towers each covering a $(\Delta\eta, \Delta\phi)$ range of about $(0.087, 0.087)$ so that one tower of the HCAL matches with 5×5 crystals

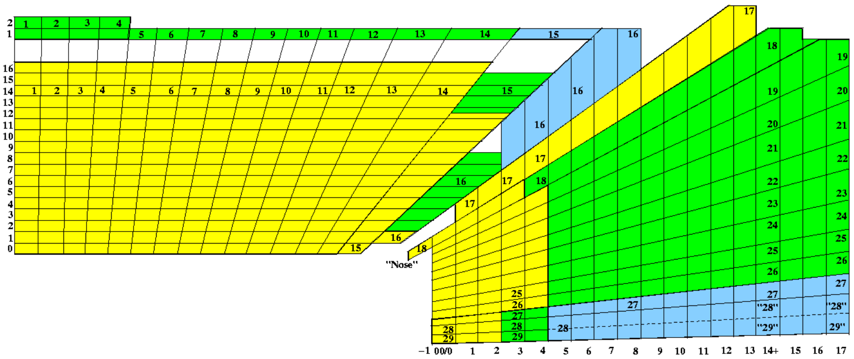

Figure 3.5: Tower structure of the CMS HCAL in the r-ϕ view [85].

of the ECAL. In total, the barrel is segmented into 32 towers in η times 18 towers in ϕ. Figure 3.5 shows the tower structure of the HB, HO and HE for a quadrant of the detector. Each tower contains 16 absorber layers, where the first and the last one are made of steel while all other absorber plates are made of brass. Plastic scintillator tiles are installed between these absorber layers. The scintillation light is led through wavelength-shifting fibre cables and detected by hybrid photodiodes.

The HEs cover an important range of the solid angle, which contains about one third of all particles being produced. The setup of the HEs is structured in towers and layers similar to the HB as shown in Figure 3.5.

The main purpose of the HO is to compensate the lack of material in the HB especially in the very central region. Like the iron yoke it is structured into five barrel rings. The central ring containing eight rings of towers has two layers of scintillator tiles while each of the other ones contains only one layer.

The HF is expected to absorb the largest part of the particle flux, hence the layout is geared to radiation hardness. Quartz fibres are used as active medium in the HF. The absorber plates consist of iron. For the analysis described in this work the HF is only used for the measurement of the luminosity as described in Section 5.2.

The energy resolution of the calorimeter jets reconstructed from combined ECAL and HCAL information in the pseudorapidity region and energy range relevant for the analysis described in this work can be parametrised by

$$\left(\frac{\sigma}{E}\right)^2 = \left(\frac{100\%}{\sqrt{E}}\right)^2 + (5\%)^2 \tag{3.5}$$

with the energy given in GeV [85].

3.2.4 Muon System

Muons are well suited to distinguish interesting collision events from background. For this reason, the ability to identify muons reliably and to measure their momenta is an important factor considered in the CMS design. The muon tracking detectors are installed outside the magnet coil on and inside the iron reflux yoke. Figure 3.6 shows a schematic illustration of the CMS muon system. There are three different types of detectors: drift tubes (DT) in the barrel covering the pseudorapidity range $|\eta| < 1.2$, cathodic strip chambers (CSC) in the endcap covering the range $0.9 < |\eta| < 2.4$, and resistive plate chambers (RPC) as well in the barrel as in the endcaps going to $|\eta| = 1.6$.

The DTs are installed in and on the wheels of the iron yoke. For this reason, the length of the anode wires parallel to the beam line is constrained by the width of the yoke wheels which is about 2.4 m. In the muon barrel, the reflux of the magnetic field gives a homogeneous field strength of about 2 T bending the muon tracks in the opposite direction as in the silicon tracker. The DTs are filled with a mixture of 85% CO_2 and 15% Ar as quenching gas. The maximum drift distance is 2.1 cm corresponding to a drift time of 380 ns. The DT system is divided into twelve azimuthal sectors each comprising four stations. The first station in each sector is installed on the inner side of the yoke barrel rings, the second and third one in cavities inside the yoke, and the fourth one on the outside. The drift tubes are organised in superlayers each consisting of four layers with parallel anode wires. The drift cells have a rectangular profile and are staggered by half a cell to each other. Each of the three inner stations is equipped with two superlayers with anode wires in z-direction to measure the azimuthal angle ϕ of muon tracks and a superlayer with wires orthogonal to the beam line and the radial direction to measure the z-component, respectively η, of tracks. The setup of such a drift tube chamber with three superlayers is shown in Figure 3.7(a). The fourth stations on the outside of the detector are equipped only with two superlayers for the ϕ-coordinate and none for the z-coordinate. The superlayers of one station achieve a combined resolution of about 100 μm.

CSCs are used in the endcaps to detect muon tracks. They can be run reliably in the strong and inhomogeneous magnetic field in this region. The CSCs are organised in ring discs in the r-ϕ plane. The chambers are trapezoidal multiwire proportional chambers and cover angles of 20° in ϕ in the inner ring disc, respectively 10° in the outer rings. A schematic drawing of a CSC is shown in Figure 3.7(b). As can be seen in Figure 3.6, the CSCs are organised in such a way that a particle with $|\eta| > 1.2$ going only through the endcap and not through the barrel overlap region crosses three or four CSCs. Each chamber comprises seven layers of cathode panels that are oriented in the radial direction. The anode wire layers run in azimuthal direction between these strip layers. The ϕ-position of a passing particle is determined from the distribution of charge induced on the cathode strips. Because of the small distances of the wires of 3.12 mm, the drift times are short so that about 99% of all tracks can be associated to the correct bunch crossing.

The timing of the muon crossing is improved by the RPCs in the whole barrel region and in the endcaps in the region $|\eta| < 1.6$. There are two layers of RPCs in each of the two inner muon stations in the barrel while the outer two

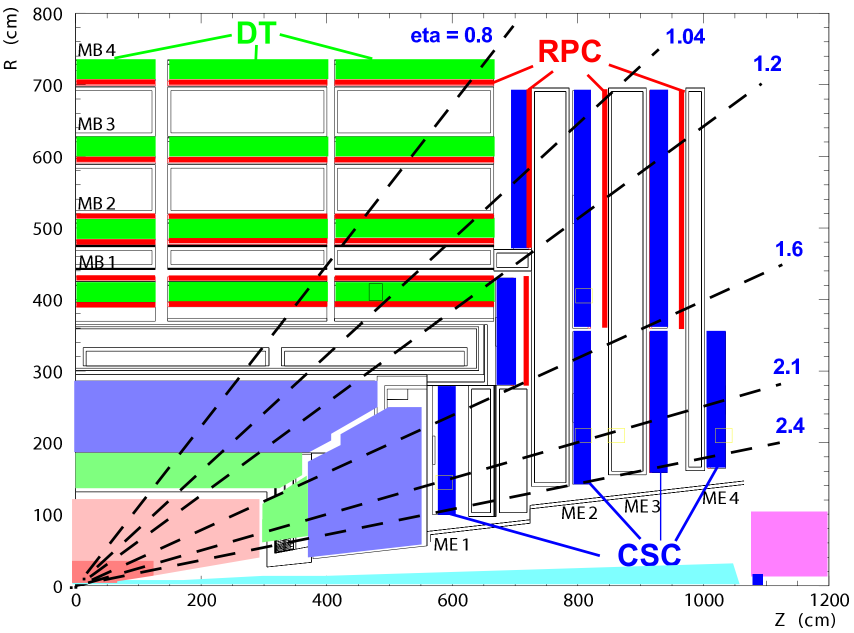

Figure 3.6: The CMS muon system illustrated for a quadrant of the CMS detector.

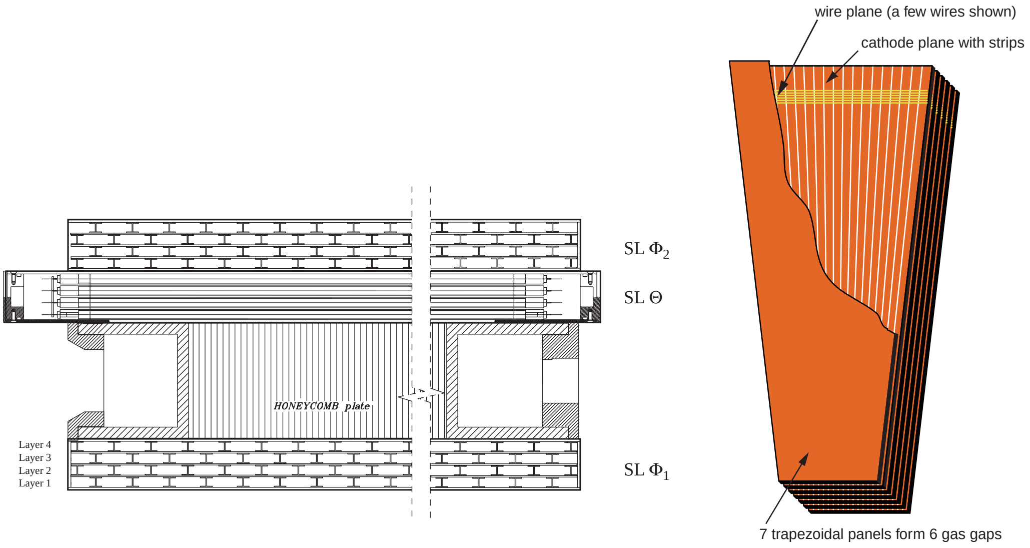

(a) DT superlayer

(b) CSC

Figure 3.7: Schematic view of a DT station used in the muon barrel and a CSC used in the endcaps [85]. The DT station on the left side is displayed in the r-ϕ cut perspective. The superlayers at the bottom and the top denoted as SL Φ_1 and SL Φ_2 have wires running in the z-direction, the SL Θ is equipped with azimuthal wires. On the right side, a CSC is shown in parallel r-ϕ perspective.

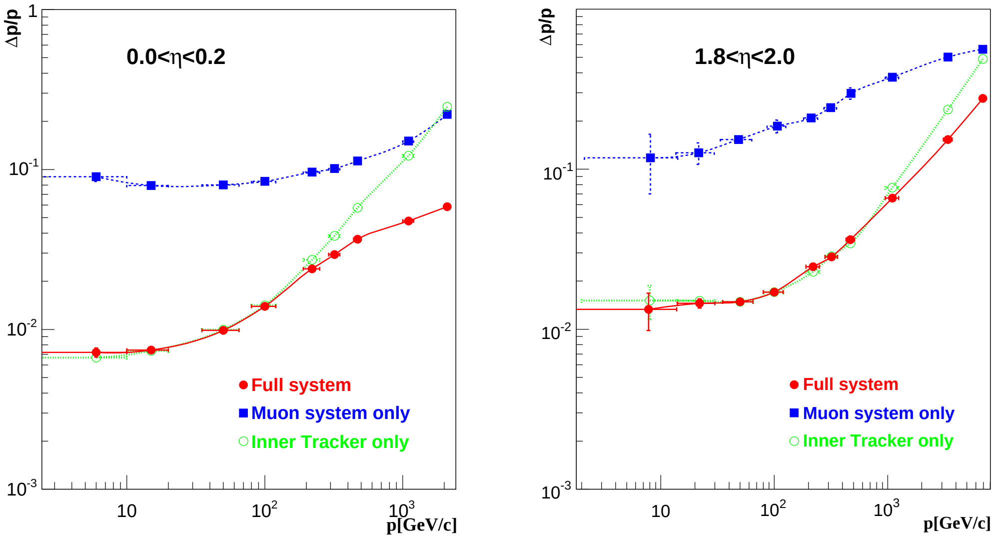

Figure 3.8: Momentum resolution of tracks using only the silicon tracker, the muon system, and the combined system in two different regions of the pseudorapidity [85].

stations are each equipped with only one layer as can be seen from Figure 3.6. In the endcaps, there is one layer of RPCs behind each CSC. A RPC consists of a gas filled volume (gap) between two resistor plates in an electric field. A passing ionising particle causes a charge avalanche, which is measured by readout strips. The RPCs used at CMS are double-gap chambers with common readout strips. Because the width of the gaps is only two millimetres, the timing is very fast and the association of ionising events to the correct bunch crossing is no problem. On the other hand, the spatial resolution is not as precise as that of the other muon detectors. The purpose is to combine the complementary information of the different muon detectors and to use the RPCs primarily to improve the triggering.

The global track reconstruction combining the silicon tracking detector and the muon system improves the precision of the momentum measurement with respect to the tracker-only reconstruction, especially for muons with high transverse momentum. This is shown in Figure 3.8.

Chapter 4

Event Simulation

4.1 Monte Carlo Method

Computer simulations are used in high energy physics to predict and understand the processes that occur in particle collisions and to model the distributions of the emerging decay particles. Especially the modelling of expected background processes in analyses is important. The complex final states that occur in hadron–hadron collisions with high particle multiplicities cannot be calculated analytically, so a numerical approach is chosen. The underlying technique is the Monte Carlo method.

The Monte Carlo method is a numerical integration method based on (pseudo-)random numbers. An integral F on a function $f(x)$ defined in a volume Ω with arbitrary dimension can be written as

$$F = \int_{\Omega} f(x)\, d^n x = V \, \langle f(x) \rangle, \tag{4.1}$$

where V is the n-dimensional volume of Ω and $\langle f(x) \rangle$ is the mean value of $f(x)$ in the given volume. This integral can be approximated by

$$F \approx F_i = V \frac{1}{N} \sum_{i=1}^{N} f(x_i) \tag{4.2}$$

with x_i being randomly chosen points inside V. Regarding to the law of large numbers, F_i converges against F for large N. It can be deduced from the central limit theorem that the error of F_i is proportional to $1/\sqrt{N}$. While in low-dimensional problems there are faster and better numerical algorithms, the Monte Carlo method converges faster in high-dimensional cases.

The generation of a collision event is fulfilled in factorised steps. The hard process is calculated first. The matrix elements of the process are calculated with the momenta of the ingoing partons being randomly chosen based on input PDFs and the momenta of the outgoing partons being randomly distributed in the available phase space. In each part $d\Omega$ of the phase space the corresponding differential of the cross section $d\sigma$ is proportional to the square $|\mathcal{M}|^2$ of the calculated matrix element. The total generated cross section is given by the integral over the phase space Ω.

Most of the common event generators calculate matrix elements only in leading order. After the calculation of the hard process, higher order QCD effects are added using parton shower models. Partons can emit gluons before and after the hard process. This is called initial state radiation (ISR) and final state radiation (FSR), respectively. The evolution of the partons during parton showering is governed by the DGLAP equations 2.8.

For the hadronisation of the partons, different hadronisation models are used. Since hadronisation happens at energy scales of about Λ_{QCD}, these processes cannot be calculated in perturbation theory. Hadronisation models are exclusively phenomenological and can be tuned to measured data. The most common models are the cluster model and the string model. In the first, one gluons are first split into two quarks. Quarks that are close to each other in phase space are combined to clusters that are colour singlets. These clusters are then decayed isotropically in their rest frame into hadrons. In contrast, the interaction between two colour connected quarks in the string model is modelled with a field string between them, which corresponds to the physical colour field of the strong interaction. Gluons that carry colour charge and anti-colour charge are connected to two other particles. This field has an energy content proportional to the length of the string. If the distance of the quark pair exceeds a certain limit, a new $q\overline{q}$ pair is created between them and the connecting field string breaks into two separate ones. This process is iteratively repeated until all remaining colour connected quark pairs correspond to on-shell mesons. Also two quark pairs can be produced the same time in one string break-up, which leads to the production of baryons. Also the underlying event and multiple interactions emerging from the coloured remnants of the colliding hadrons have to be taken into account for the hadronisation process. Subsequently, the decay of unstable hadrons to stable particles is simulated.

With the 2010 collision data, physics quantities on generator level like e.g. the jet multiplicity could be tuned to data to reduce deviations [86]. For all generation steps, several different implementations are available. Those of them used for this work are described in the following sections.

4.2 Pythia

Pythia [87] is an event generator project going back to the 1970s. The simulated samples used in this work are produced with Pythia6, which is written in Fortran. Pythia is a multi-purpose generator that can fulfil all steps of the simulation described in the previous section. It is capable to simulate all standard model processes as well as processes in theories beyond the standard model. Matrix elements are calculated in leading order. Additional jets in the final state cannot be calculated analytically with Pythia. These can only be generated via parton showering.

4.3 MadGraph

MadGraph [88] calculates matrix elements on tree level. In contrary to Pythia, the radiation of hard gluons in ISR and FSR is also calculated on matrix element level, i.e. the matrix elements for the hard process + 0, 1, 2, …jets are calculated separately. These processes are then combined via matching. This way, the process is simulated with the correct LO cross section and the radiation of hard, well separated jets simulated on matrix element level. It is important for the combination with parton showering to avoid double counting, i.e. to use the same element of the phase space twice with the same jet generated on matrix element level and via parton showering. Both methods of generating jets have to be separated using phase space thresholds.

MadGraph is specialised on proton–proton and proton–antiproton collisions. For the simulation of parton showering and hadronisation, MadGraph has to be interfaced to other generator programs like Pythia. The agreement of the hard jet multiplicity in MadGraph is modelled in better agreement to the data than in Pythia. For this reason, mainly samples with the hard processes calculated by MadGraph are used in this work.

4.4 Tauola

Tauola [89] is a dedicated package for the simulation of τ lepton decays. It has been applied for all simulated event samples used in this study. Tauola takes into account spin information and QED corrections in the calculation of the τ decays.

4.5 Detector Simulation with GEANT

The event generators only model the physics of the interaction, i.e. the production of particles in collisions and subsequent possible decays. The interaction of the final particles with the material of the detector is modelled afterwards in a separate step. The software used for this simulation step is Geant [90]. It provides the simulation of all relevant interactions of particles with different materials and thus models bremstrahlung of charged particles, electromagnetic showering, multiple scattering, but also hadronic interactions.

Geant provides also tools to simulate the geometry of the experiment. The complete CMS detector including all sensitive parts as well as the supporting structure are rebuilt in the simulation [91]. After the interaction of the passing particles with the detector, the response of the detector is simulated in the digitisation step. The output of this step has a format identical to the output from the real detector and subsequently the same reconstruction algorithms are run on the simulated events like on the real collision events. Hence, the simulation output can be directly compared to data. Deviations between data and the simulation are tried to be minimised by correcting the simulation to the data. Even before the detector was composed in its cavern, the interaction with the material was tuned using test beam data from the single subsystems.

Chapter 5

Event Reconstruction Process

5.1 Trigger and Data Acquisition

With the full LHC luminosity, the time between two bunch crossings in the CMS detector can go down to 25 ns, usually producing some tens of proton–proton interactions each. Since the data size of one event is in the order of 1 MByte, recording all data would result in a data flow of tens of TByte/s which is not achievable in practise. For this reason, an efficient trigger system decides online, i.e. during data taking, which events to record. The CMS trigger system reduces the event rate from initially 40 MHz down to $\mathcal{O}(100)$ Hz. Its technical implementation consists of the Level-1 trigger (L1 trigger) that uses custom-designed hardware and reduces the event rate by about three orders of magnitude and the high-level trigger (HLT) that is implemented in form of a computing farm with $\mathcal{O}(10^3)$ commercial processors. Since the L1 trigger has to make decisions very fast, it is implemented close to the detector and uses only coarsely reconstructed information from the calorimeters and the muon system. The detector front-end electronics store the detector output for 3.2 μs in pipelined memories. During this time an L1 trigger decision has to be made. If an event passes the L1 trigger, it is read out and the HLT makes use of the complete event information from all subsystems.

The architecture of the L1 trigger is structured in local, regional, and global trigger components as shown in Figure 5.1. In the muon DTs and CSCs, track segments are reconstructed locally. On the regional trigger level, the source track segments are combined to tracks using track finder algorithms. This is done separately in the DTs and CSCs. In parallel, Muon candidates are reconstructed in the RPCs independently of the DT and CSC track finders. The global muon trigger then combines the information of all three subsystems. Redundancies among the subsystems reduce the background of the muon trigger. Additional information about isolation and minimum-ionising particle signatures from the calorimeters is used by the global muon trigger. The calorimeter trigger has a similar logical structure as the muon trigger. In the calorimeters, physics objects like electron, photon, or jet candidates are reconstructed. Furthermore, global quantities like missing transverse energy $\not\!\!E_{\mathrm{T}}$ and the scalar

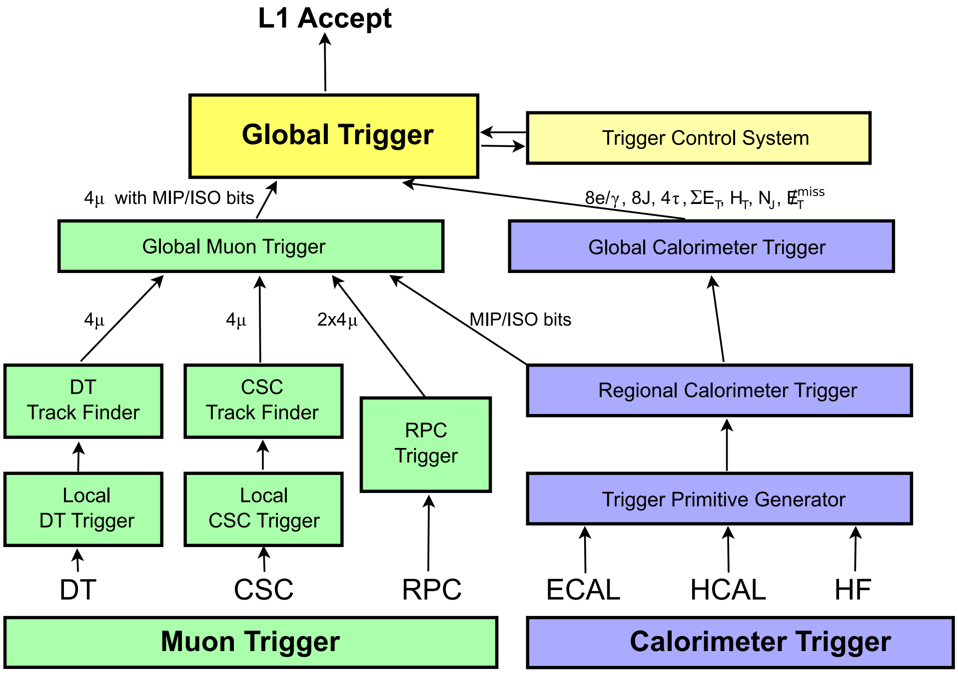

Figure 5.1: Architecture of the L1 trigger. Reproduction from [81].

sum of the jet energies H_{T} are evaluated. The information from the global muon and calorimeter triggers are sorted and ranked by the global L1 trigger. The decision if an event is kept is based on the reconstructed trigger objects and quantities but also on the readiness of the sub-detectors and data acquisition system (DAQ). This information is delivered by the trigger control system (TCS) [81].

If an event is accepted by the L1 trigger, the complete event information is copied from the pipelined memories to the HLT computer farm. The ingoing event rate of about 10 kHz corresponds to a data flow of about 100 GByte/s and is reduced by the HLT by another three orders of magnitude. Special versions of the reconstruction algorithms are utilised for fast reconstruction of physics objects. For reasons of time optimisation, the data processing is structured in virtual trigger levels, and objects on higher trigger levels have to be seeded by reconstructed objects on the lower level.

The trigger system is organised in trigger paths, which can contain several trigger filters in sequence. Several trigger paths for single muons or for two muons are used at CMS with different p_{T} thresholds and prescale factors. A prescale factor of n for a certain trigger path means that only one out of n events that fires the trigger is recorded. This is needed for trigger paths with an event rate that is too high to record all events.

As an example, the `HLT_mu15_v1` trigger path, which is used later in this work, consists of two filters on HLT level. The parameters of the L1 muon candidates are used to seed the reconstruction of a L2 standalone muon, i.e. a muon reconstructed only in the muon system. On these L2 candidates a filter is applied that requires at least one muon with a transverse momentum $p_{\mathrm{T}} > 7\,\mathrm{GeV}$. Having passed the L2 filter, on Level 3 the muon candidates are reconstructed globally including also information from the tracking detector. The L3 filter requires one muon with $p_{\mathrm{T}} > 15\,\mathrm{GeV}$ [92].

If an event is accepted also by the HLT, it is stored permanently and the offline reconstruction algorithms are run to reconstruct the physics objects that are used for later analysis. In parallel, a data stream for online data quality monitoring (DQM) is created. The DQM system fills several histograms giving information about the status of each subsystem and different physics objects. These histograms are used to evaluate the quality of the data. Only data for that all relevant subsystems are certified as good are used for analysis.

The data recorded at CMS are structured in runs and luminosity blocks. A run is a longer period of data taking that can endure up to several hours. A luminosity block is a shorter segment of data corresponding to a fixed number of about $\mathcal{O}(10^6)$ beam orbiting periods.

5.2 Luminosity Measurement

A precise determination of the integrated luminosity is mandatory for cross section measurements since the error of the luminosity directly affects the final result. The luminosity at CMS is measured online in the forward calorimeters HF [93] but several offline methods are also used to cross check the online measurement.

The online measurement makes use of the relation of empty HF towers to the number of proton–proton interactions per bunch crossing. This method is called zero counting. Another way to measure the luminosity with the HF is the linear dependency of the luminosity on the deposed transverse energy. In order to gain the best linearity, only the region $3.5 < |\eta| < 4.2$ is used. At the relatively low luminosity during 2010 data taking, the first method offered a better performance and thus it was used as default. The relation between $\mathcal{L}$ and transverse energy was used offline. Counting the number of vertices per bunch crossing gives an offline cross check with independent systematic uncertainty. All methods give consistent results for measuring the time dependence of the luminosity.

The absolute calibration is achieved via van der Meer scans [94]. For these scans, the beams are moved transversely to each other and the interaction rate is measured as a function of the beam separation. Shape and and size of the interaction region can be measured this way. They determine the factor F in Formula 3.3 and hence the instantaneous luminosity can be calculated.

The relative error on the luminosity, which translates directly into the luminosity-caused uncertainty of measured cross sections, was reduced to 4% [95]. The most important uncertainties are the measurement of the beam currents and variations between different fills. During 2010 data taking, the

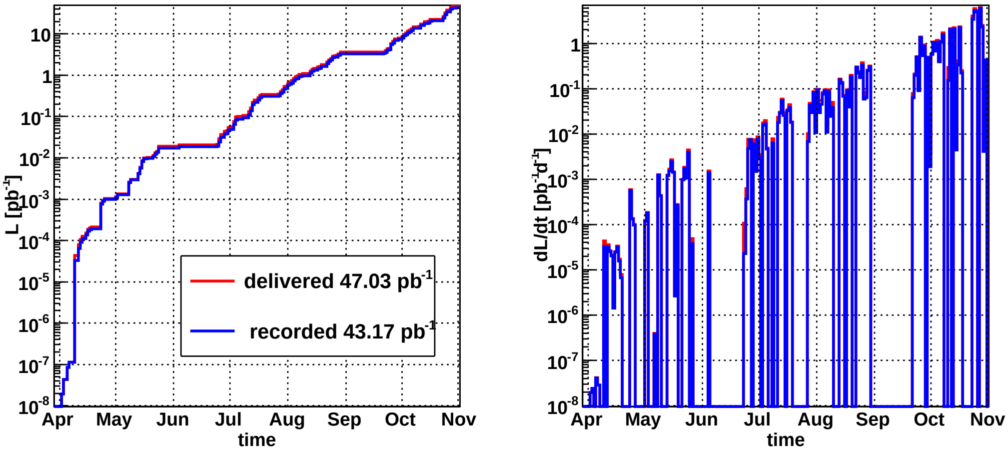

Figure 5.2: Delivered and recorded luminosity in 2010. The left plot shows the total integrated luminosity as a function of time. The right plot shows the luminosity taken per day. The first collisions took place on March 30th. During the data taking the instantaneous luminosity was increased constantly over several orders of magnitude. Data were taken until the end of October. Plot produced with raw data from [96].

LHC delivered an integrated luminosity of $47\,\mathrm{pb}^{-1}$ for the CMS experiment with a maximum instantaneous luminosity of $2 \times 10^{32}\,\mathrm{cm}^{-2}\,\mathrm{s}^{-1}$. However, only $43\,\mathrm{pb}^{-1}$ of that were recorded by the DAQ system and only $35.9\,\mathrm{pb}^{-1}$ were certificated as good for analysis by DQM inspections. The two plots in Figure 5.2 show the delivered and recorded total integrated luminosity and integrated luminosity taken per day, respectively.

As an alternative to the methods described above, it is also possible to measure a cross section in proportion to the production cross section of W or Z bosons. This way, the counted number of vector bosons in combination with their theoretical production cross sections is used to measure the luminosity.

5.3 Physics Object Reconstruction

Corresponding to the underlying interactions, different kinds of particles leave signatures in different parts of the detector. The trajectories of charged tracks can be measured in the tracking detectors, electrons and photons produce showers and loose their energy in the ECAL while hadrons mainly depose their energy in the HCAL. Physics objects are reconstructed by combining information from different subsystems, e.g. an electron is reconstructed by matching a track in the inner tracking system to a cluster of deposed energy in the ECAL. In the following, the reconstruction algorithms of physics objects used for this analysis are elucidated. These are muons, hadronic jets and missing transverse energy.

5.3.1 Muon Reconstruction

High-energy muons pass all detector subsystems of the CMS detector. Their tracks can be reconstructed as well in the silicon tracking detector as in the muon system. Regarding to the Bethe formula [97] [98], they are expected to depose only a small amount of energy in the calorimeters. This minimum ionising particle (MIP) signature can be used for muon identification.

Based on the tracks reconstructed in the silicon tracker and in the muon system, there are two algorithms used to reconstruct muons at the CMS experiment. These are the global muon reconstruction (outside-in) and the tracker muon reconstruction (inside-out) [99].

The reconstruction of a global muon starts with a track reconstructed in the muon system. This is extrapolated to the silicon tracker. If a matching silicon track exists, a global muon track is fitted using the hits in the silicon tracker as well as those in the muon system. The global fit improves the momentum resolution for high-momentum muons with $p_{\mathrm{T}} \gtrsim 200\,\mathrm{GeV}$ compared to the tracks reconstructed only from silicon tracker. This can be seen in Figure 3.8.

Tracker muons are reconstructed starting from a silicon track that is extrapolated to the muon system. All tracks with $p_{\mathrm{T}} > 0.5\,\mathrm{GeV}$ and $p > 2.5\,\mathrm{GeV}$ are treated as potential muon candidates for this algorithm. The extrapolation takes into account the expected energy loss in the material between the tracker and the muon system as well as the uncertainty due to multiple scattering. If the extrapolated track can be matched to at least one track segment in one DT or CSC chamber within the uncertainty, it is considered as a tracker muon.

A small fraction of about 1% of all muons from collisions are only reconstructed in the muon system. This can happen if the inner track in the silicon detector cannot be reconstructed or the matching track is not found by the algorithm. These muon are called standalone muons. Most muons from cosmic radiation are reconstructed as standalone muons because of the small geometrical acceptance of the silicon tracker for cosmic muons. For this reason the ratio between muons from collisions and cosmic muons is a factor 10^4 to 10^5 lower for standalone muons than for tracker and global muons.

5.3.2 Jet Reconstruction

Due to hadronisation, the irradiation of single quarks or gluons leads to the creation of many hadrons. Because of momentum conservation, these hadrons are close to the direction of the original particle. Such a collimated bundle of hadrons is called a hadronic jet.

Jet Algorithms For the reconstruction of jets, i.e. the attribution of hadrons to an initial quark of gluon, several algorithms are used at CMS. These algorithms can be run on several reconstructed input entities like calorimeter towers, particle candidates or tracks. Important requirements for jet algorithms are infrared safety and collinear safety. Infrared safety means that the jets have to be insensitive to addition of soft particles, collinear safety means stability of the jet finding if one hard particle is split into two or more softer ones. Another performance criterion, especially on trigger level, is the speed of the algorithm [100]. On trigger level, the iterative cone algorithm is used because of its fast and predictable runtime.

Jet algorithms can be categorised in two classes. Cone algorithms like SISCone or Iterative Cone try to maximise the energy flow within a cone with a given radius R in η and ϕ [101]. Clustering algorithms sequentially combine entities based on their distances to each other. A distance d_{ij} between two entities and a quantity d_i for each entity are defined for these algorithms. The algorithm searches the smallest of these distances and if it is a d_{ij} the two entities i and j are merged. If instead d_i is found to be the smallest distance, i is called a jet and removed from the list of entities. This procedure is repeated until all entities of the initial collection are merged to jets.

The most important difference between the clustering algorithms is the way the distances d_{ij} and d_i are defined. The definition

$$d_{ij} = min(k_{\mathrm{T}i}^{2p}, k_{\mathrm{T}j}^{2p})\frac{\Delta_{ij}^2}{R^2}, \tag{5.1}$$

$$d_i = k_{\mathrm{T}i}^{2p} \tag{5.2}$$

ist often used with $k_{\mathrm{T}i}$ being the transverse momentum, $\Delta_{ij}^2 = (y_i - y_j)^2 + (\phi_i - \phi_j)^2$ being the angular distance of entities i and j in rapidity y and ϕ and R and p being free parameters of the algorithm. The parameter R is a size parameter to weight the distances d_{ij}. The behaviour of the algorithm does strongly depend on the value of p that sets the power of the momentum scale. Important are the cases $p = 1$ which is called the k_{T} algorithm, $p = 0$ which is the Cambridge–Aachen algorithm, and the case $p = -1$. Because of the negative power, the latter one is called the anti-k_{T} algorithm. It fulfils the requirements of infrared and collinear safety and shows to produce jet with boundaries which are resilient with respect to soft radiation. Therefore, the anti-k_{T} algorithm is the default algorithm for most physics analyses at CMS [102].

Jet Types All of the algorithms can be run on several input quantities. They can be directly applied on generated particles in the simulation to produce generator jets. On reconstruction level, there are four different types of jets [103]. One approach is to reconstruct jets only using the energy deposits in the calorimeters (calo jets). As the energy resolution of the calorimeters, especially of the HCAL, is not sufficient for most analysis purposes, the energy measurement can be improved by matching tracks from the silicon tracker

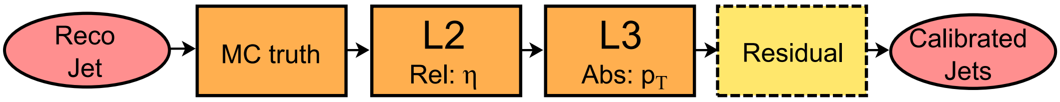

Figure 5.3: Jet energy correction scheme. The residual corrections are applied only to collision data.

to the calo jets and making use of the excellent momentum resolution of the tracking detector. These track corrected calo jets are called JPT jets.

A different approach is the concept of particle flow (PF) [104]. Particle flow means that all stable particles in the event are tried to be reconstructed. In the first step of the particle flow algorithm, fundamental elements like tracks and calo clusters are reconstructed. These are then linked to each other in blocks based on their position in η and ϕ. In the last step, particles are reconstructed from these blocks that can contain several particles. For example, charged hadrons are reconstructed from tracks in the inner detector and clusters in the HCAL while neutral hadrons are reconstructed from HCAL clusters without a track. If the clusters of charged and neutral hadrons overlap in the HCAL, the neutral hadrons can be identified from the overplus of deposed energy with respect to the track of the charged particle. Particle flow jets are afterwards reconstructed with the algorithms described above running on the list of PF particles as input.

The last type of jets are the track jets which use only the tracks from the silicon tracking detector as input. These jets are at CMS only used as cross check to compare with other jet types since the systematic uncertainties of their energy scale is complementary to those of the calo jets. In this work, anti-k_T PF jets with a size parameter of $R = 0.5$ based on are used.

Jet Energy Correction After the jets have been reconstructed, their measured energy is calibrated in several sequential steps in order to bring it in accordance with the energy of the original particle [105]. Figure 5.3 shows the jet correction scheme applied for the analysis described here. The first step[1] is applied using a QCD Monte Carlo simulation. The same jet algorithm that is used for the event reconstruction is also run on the simulated particles on generator level. The jets of the reconstructed events are matched to these generator jets and the measured energy is compared to the true level value. The ratio between these quantities is the calibration factor which is measured as a function of p_T and η. Because the simulation of the detector does not describe the real detector perfectly, additional p_T and η dependent corrections are applied, which can be calibrated using input from data.

The second step (L2 correction) is to confirm the flatness of the calibrated energy response in η. For this correction, the p_T balance of dijet events is used.

---

[1] This correction must not be mixed up with the Level-1 offset correction in older descriptions like [100]. The Level-1 correction was not applied on the data used for this work.

This method uses transverse momentum conservation in events with two hard jets which are back to back, where one jet is in the central region and the other one at arbitrary η. Jets with higher absolute values of η are corrected with respect to jets in the central region. This can be done with simulated dijet events as well as with selected ones from real data. For this work still simulation-based correction factors are used.

The L3 correction is an absolute scaling making use of the p_{T} balance of γ+jet events. Since the photon is measured in the ECAL which has a much better energy resolution than the HCAL, its energy is determined slightly precise in comparison to that of the recoil jet. This method can be applied with real data as well. However, for this analysis the calibration was not finished and is still done with a simulated sample.

Because the correction steps described above are calibrated with simulated samples, there is still a deviation between data and simulation after the L3 correction. While for small values of $|\eta|$ there is a good agreement between data and simulation, the deviation for higher $|\eta|$ goes up to 10%. Hence, for the collision data an additional p_{T} and η dependent correction is applied on top of the L2 and L3 corrections [106]. The approach to apply residual corrections on top of the simulation-based calibrations leads to a smaller systematic uncertainty as a calibration completely on the available data would achieve. Several additional correction steps are foreseen but are not yet sufficiently well understood and hence not used, e.g. corrections taking into account the electromagnetic fraction or the flavour of the parton that has initiated the jet.

5.3.3 Missing Transverse Energy

The missing transverse energy of a collision event, abbreviated with MET or $\not\!\!E_{\mathrm{T}}$, is the imbalance of the measured particle momenta in the transverse plane, which can be caused by weakly interacting particles that are produced and leave the detector unobserved. A part of this $\not\!\!E_{\mathrm{T}}$, however, is faked due to measuring inaccuracy of the observable particles, mainly of the jets. Nevertheless, conclusions can be made about particles like neutrinos or exotic particles, which are produced in the event but do not interact with the detector, by measuring this imbalance .

Corresponding to the different types of jets described in the previous subsection, also $\not\!\!E_{\mathrm{T}}$ can be reconstructed using either the energy deposits in the calorimeters, the tracks, or the particle flow candidates. The $\not\!\!E_{\mathrm{T}}$ used for this analysis is reconstructed using particle flow objects. The missing transverse energy is reconstructed by simply calculating the vectorial sum of the transverse momenta of all PF candidates in the event and taking the negative value as $\not\!\!E_{\mathrm{T}}$ [104].

Chapter 6

Event Selection

6.1 Signature of Signal Events

The decay channel under study in this work is the dimuon $t\bar{t}$ decay mode

$$t\bar{t} \rightarrow b\bar{b}\,W^+W^- \rightarrow b\bar{b}\,\mu^+\mu^- + \text{ neutrinos} \tag{6.1}$$

where both, the top and the antitop quark, decay into a b, respectively $\bar{b}$ quark, and a W boson. Subsequently, the two W bosons decay into two muons and neutrinos. Hence, the signature of these events is given by two b jets resulting from the hadronisation of the b and the $\bar{b}$ quarks, two oppositely charged muons which are spatially isolated from hadronic activity and missing transverse energy $\not{E}_\mathrm{T}$ due to the neutrinos that leave the detector unobservably. The decay channel where both W bosons go directly into one muon and a corresponding neutrino

$$t\bar{t} \rightarrow b\bar{b}\,W^+W^- \rightarrow b\bar{b}\,\mu^+\mu^-\nu_\mu\,\bar{\nu}_\mu \tag{6.2}$$

is the most important one for this analysis and makes a fraction of about 1.2% of all $t\bar{t}$ decays. Because the event signature is the same for $t\bar{t}$ decays

$$t\bar{t} \rightarrow b\bar{b}\,W^+W^- \rightarrow b\bar{b}\,\tau^\pm\mu^\mp\nu_\tau\,\bar{\nu}_\mu \rightarrow b\bar{b}\,\mu^+\mu^- + 4 \text{ neutrinos} \tag{6.3}$$

or

$$t\bar{t} \rightarrow b\bar{b}\,W^+W^- \rightarrow b\bar{b}\,\tau^+\tau^-\nu_\tau\bar{\nu}_\tau \rightarrow b\bar{b}\,\mu^+\mu^- + 6 \text{ neutrinos} \tag{6.4}$$

where one or both of the W bosons decay tauonically and the τ leptons subsequently decay to muons and neutrinos also these decays are treated as signal. With these channels, the branching fraction increases to 1.6%.

Figure 6.1 shows an event display of a typical candidate of a $t\bar{t}$ dimuon event selected in the 2010 data. In the r-ϕ view two isolated muons with transverse momenta of 40 GeV and 90 GeV can be seen pointing to the upper left and downwards. The yellow cones inside the calorimeter illustrate reconstructed PF jets. There are two hard jets pointing upwards and to the right with transverse momenta of 66 GeV and 95 GeV. The $\not{E}_\mathrm{T}$ vector points to the left and amounts to 39 GeV.

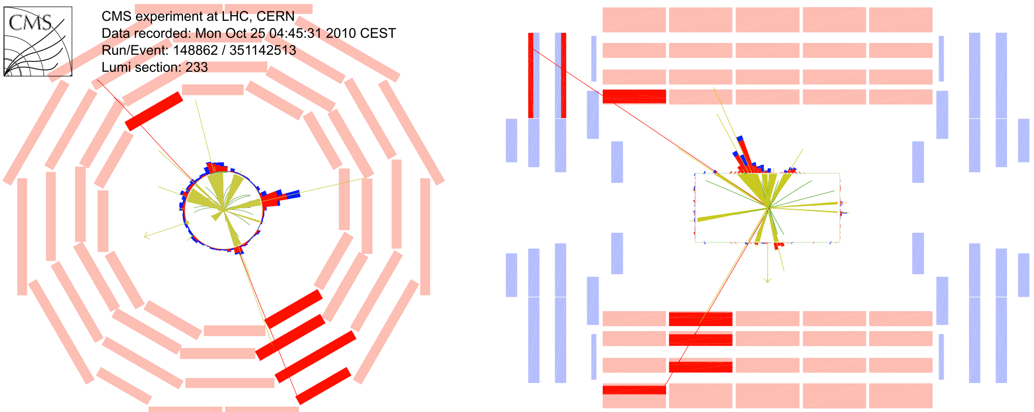

(a) r-ϕ view

(b) r-z view

Figure 6.1: Event Display of a $t\bar{t}$ candidate recorded on October 25th 2010 by the CMS detector.

6.2 Data and Simulation Samples

In this analysis detector data corresponding to an integrated luminosity of $35.9\,\mathrm{pb}^{-1}$ are used. The input data set is a muon skim, i.e. selected with a logical or of all muon trigger paths [107].

Monte Carlo samples are used for the simulation of background processes, for the estimation of the signal selection efficiency, and to compare selected signal events to the data. The mass of the generated top quarks in the signal samples is 172.5 GeV. Most samples used for this analysis were generated without the simulation of pile-up events. However, for systematic studies that are presented in the next chapter also a pile-up samples and other $t\bar{t}$ samples with varied settings are used.

The presence of two hard isolated muons is best suited to separate signal-like events from the overwhelming QCD background since muons from the decays of lighter quarks are usually inside hadronic jets. Hence, the most important background processes to be considered are those that also produce isolated muons from the decay of weak gauge bosons.

Processes that can produce two isolated muons are Drell–Yan events (DY) $Z/\gamma^\star \to \mu^+\mu^-$or $Z/\gamma^\star \to \tau^+\tau^-$where both τ leptons decay to muons and neutrinos, production of two vector bosons WW, WZ, ZZ, and also associated production of a single top quark and a W boson as shown in Figure 2.6.

For intermediate control distributions, also simulation samples of processes with only one muon are used. This is mainly W boson production but also QCD background is taken into account by using a QCD sample which is enriched with hard muons ($p_\mathrm{T} > 15\,\mathrm{GeV}$) because of the large cross section of these QCD processes. However, the contribution of these samples turn out to be negligible after the selection requirement of two hard isolated muons.

process	$\boldsymbol{\sigma^{\mathrm{NLO}}}$ **[pb]**
$t\bar{t}$	157.50
tW	10.60
$Z/\gamma^\star \to \mu^+\mu^-(m_{\mu\mu} > 10\,\mathrm{GeV})$	6139.00
$Z/\gamma^\star \to \tau^+\tau^-(m_{\tau\tau} > 10\,\mathrm{GeV})$	6139.00
$WW \to \ell\ell\nu\nu$	4.51
$WZ \to \ell\ell\ell\nu$	0.61
ZZ	7.40
$W \to \mu\nu_\mu$	10438.00
$W \to \tau\nu_\tau$	10438.00
QCD (μ enriched, $p_{\mathrm{T}}(\mu) > 15\,\mathrm{GeV}$)	84679.30

Table 6.1: Cross sections of the processes relevant for this study [108]. The QCD cross section is in leading order. All other values are calculated in NLO.

For the control distributions where data and simulation are compared the simulation samples are scaled using their NLO cross section σ^{NLO}. This means each histogram entry is multiplied with a weight

$$w = \frac{L\,\sigma^{\mathrm{NLO}}}{N_{\mathrm{evts}}} \tag{6.5}$$

where L is the integrated luminosity of the data and N_{evts} the number of events in the simulation sample. The only exception is the cross section of the QCD sample, which is in leading order. The used cross sections of the processes are shown in Table 6.1.

6.3 Trigger Selection and Event Cleaning

For the trigger selection several single muon trigger paths are used on data. Because the instantaneous luminosity increased during the 2010 data taking, also the p_{T} threshold for the muon trigger had to be raised for later data. For the first $3.2\,\mathrm{pb}^{-1}$ the trigger threshold was at 9 GeV on HLT level, for the next $5.0\,\mathrm{pb}^{-1}$ it was at 11 GeV and finally it was at 15 GeV for the remaining $27.7\,\mathrm{pb}^{-1}$. For all these trigger paths, a HLT muon has to be seeded by a L1 trigger muon with $p_{\mathrm{T}} > 7\,\mathrm{GeV}$.

In the simulation throughout the whole analysis the HLT_Mu9 path is used. The deviation between these different kinds of trigger selection is taken into account and compensated in the calculation of the $t\bar{t}$ cross section as explained in Subsection 7.1.1.

Some additional cleaning requirements are applied for the data. In order to reject background events like interactions between beam protons and rest gas in the beam pipe, a minimum of 25% high purity tracks is required if there are more than 10 tracks in the event. Events with a significant amount of noise in the HCAL are also rejected. Events have to have at least one good primary vertex with $N_{\mathrm{dof}} \geq 4$ which is close to the nominal interaction point with $|z| < 24\,\mathrm{cm}$ and $r < 2\,\mathrm{cm}$. However, these quality criteria are loose enough so that their impact on the cross section measurement can be neglected. Only about 1.7‰ of the events in data are rejected.

6.4 Muon Selection

In order to make the simulation comparable to the data as early as possible, the first steps of the event selection concern the muons. Muon candidates selected for the analysis are required to have a transverse momentum of $p_{\mathrm{T}} > 20\,\mathrm{GeV}$ and to be within the pseudorapidity region $|\eta| < 2.4$. Further, it is required that at least one of the muons lies inside the fiducial trigger region of $|\eta| < 2.1$.

The following muon identification requirements are applied to the candidates. The muons have to be reconstructed by both muon reconstruction algorithms described in Subsection 5.3.1, i.e. by the tracker and the global algorithm. In order to select only tracks of a sufficient quality and to remove muons from decay-in-flight processes, the selection requires a minimal number of silicon tracker hits associated with the global muon ($N^{\mathrm{trk}}_{\mathrm{hits}} > 10$) and a transverse impact parameter of the muon track with respect to the beam spot $|d_0^{\mathrm{BS}}| < 0.02\,\mathrm{cm}$. To further increase the purity of prompt muons, the global track fit (combination of tracker and muon detector hits) should have a good quality ($\chi^2/N_{\mathrm{dof}} < 10$) and at least one hit in the muon detector. The muons selected in this way are denoted as *high-purity muons* in the following.

After the selection of one high-purity muon, the data can be compared to the simulation for the first time. Figure 6.2 and 6.3 show the relevant distributions for the further muons in the events after the selection of the first one. Figure 6.4 shows distributions of all muons that fulfil the high-purity muon selection criteria after the requirement of a first muon. In Subfigure 6.4(d), the number of all selected high purity muons per event is shown. As can be seen, the contribution of events with three or more high-purity muons is completely negligible.

In the next selection step a second high-purity muon is required. Both muons are required to be associated to the same primary vertex. For this reason, both muon candidates should have a maximum z distance of 1 cm to the same primary vertex. After the selection of a second muon, the invariant mass of the selected muon pair is calculated. Events with an invariant mass of $m_{\mu\mu} < 12\,\mathrm{GeV}$ are removed in order to reject QCD background events with two muons, especially heavy flavour resonances like J/ψ or Υ. Anyhow, in the low mass region almost no signal is expected. Since signal events have two muons of opposite charge, only these events are kept for signal selection. However,

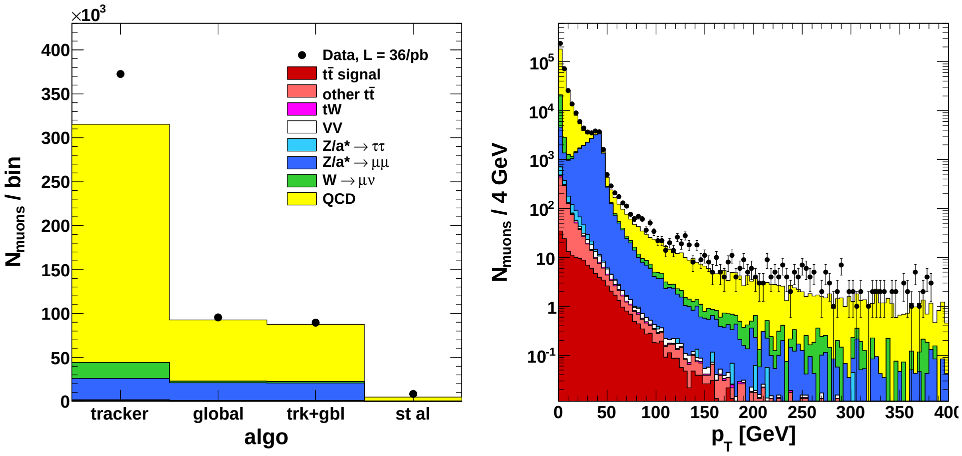

(a) number of muons reconstructed by the different algorithms (b) transverse momentum

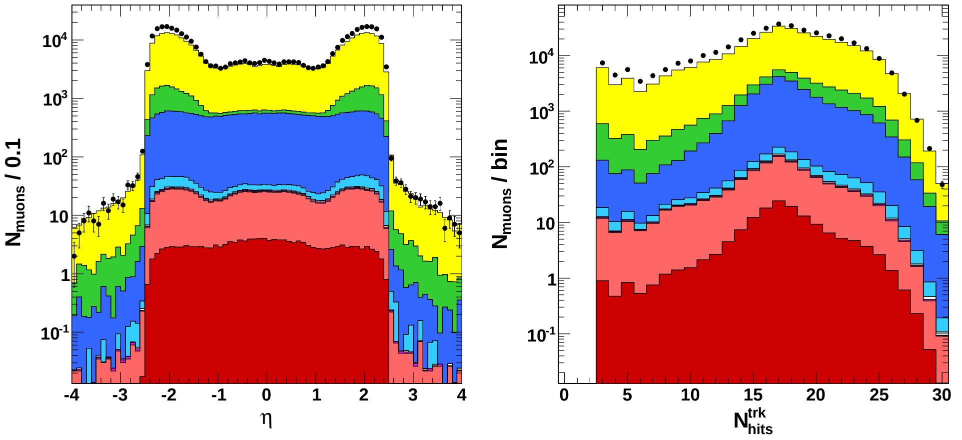

(c) pseudorapidity (d) number of tracker hits

Figure 6.2: Muon Distributions. In (a) the number of additional muons reconstructed with the available algorithms after the selection of a first high-purity muon is shown. The number of global and standalone muons is in agreement between data and simulation. The excess of tracker muon candidates is probably caused by misidentified tracks from pile-up events, since in the very first data this discrepancy is much smaller.
The other histograms show distributions for all these additional muon candidates. For the muon momentum there is a good agreement in shape. In summary, there seems to be an excess of tracks with few hits at high absolute values of η due to pile-up.

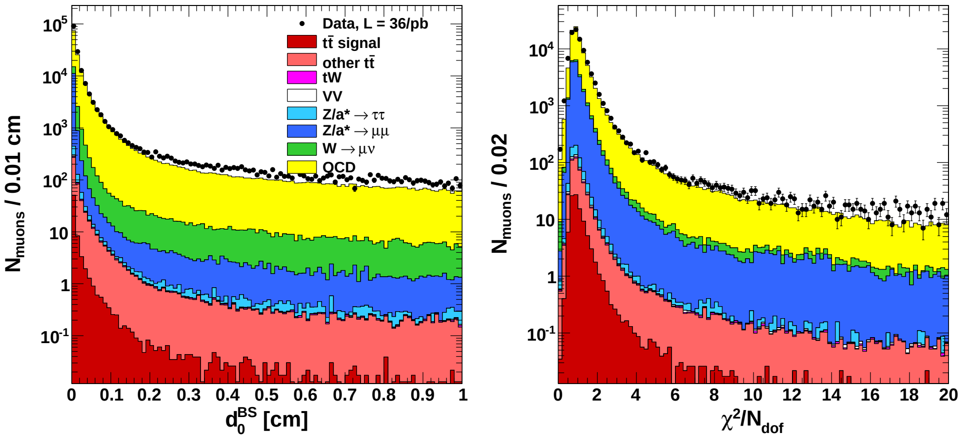

(a) transverse impact parameter (b) normalised χ^2 of global muons

Figure 6.3: Muon Distributions. In (a) the transverse impact parameter of additional muons with respect to the beam spot is shown after the selection of a first high-purity muon. The surplus of muons with high impact parameter might be from the excess of tracker muons with few hits in the track. Plot (b) shows the normalised χ^2 of the global muons tracks.

also the few events with two equally charged muons are kept separately for later background estimation as detailed in Section 7.2.1.

Muon isolation is defined as the sum of the transverse momentum of the tracks reconstructed in the tracker (I_{trk}), respectively the amount of transverse energy deposits in the calorimeters (I_{ECAL} and I_{ECAL} for the ECAL and HCAL, respectively), inside a cone in η-ϕ space of $\Delta R \equiv \sqrt{\Delta\eta^2 + \Delta\phi^2} < 0.3$ around the muon. For the tracker isolation the track of the muon is excluded from this sum. In the calorimeters there are veto cones defined around the interpolated muon track with $\Delta R = 0.08$ in the ECAL and $\Delta R = 0.1$ in the HCAL. The energy deposed in these veto cones is also excluded from the corresponding isolation sum and instead associated to the muon candidate itself. In the analysis, muons are considered to be isolated if they have $I_{\mathrm{comb}} < 0.15$, where I_{comb} is the combined relative isolation defined as

$$I_{\mathrm{comb}} = \frac{I_{\mathrm{trk}} + I_{\mathrm{ECAL}} + I_{\mathrm{HCAL}}}{p_{\mathrm{T}}(\mu)}. \tag{6.6}$$

The contributions from QCD, W and non-dimuon $t\bar{t}$ events are not visible in the plots anymore after the selection of two isolated muons. In the later histograms they are hence not listed in the legend.

In Figure 6.5 the invariant dimuon mass is shown after the requirement of two high-purity muons and after the requirement of two isolated muons. In order to get rid of the large background from DY events near the Z^0 peak,

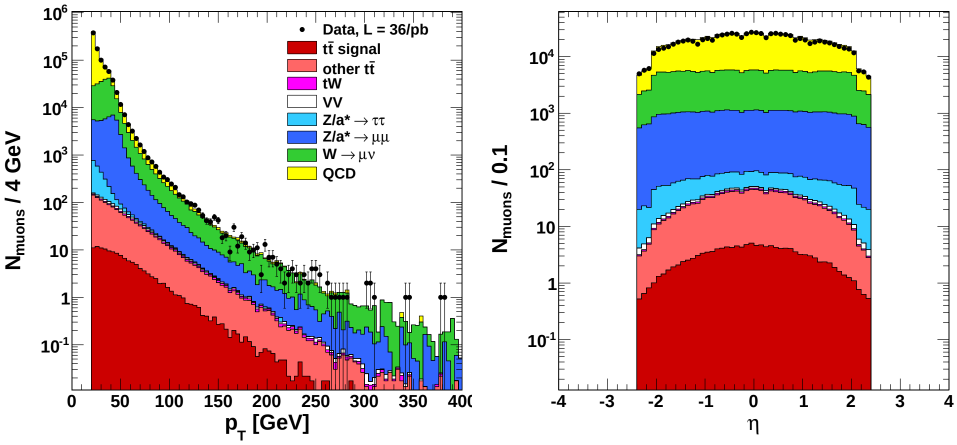

(a) transverse momentum

(b) pseudorapidity

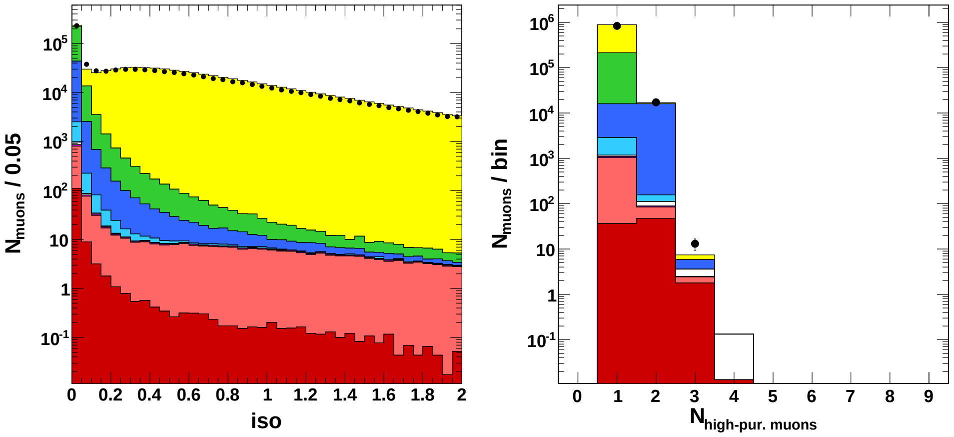

(c) isolation of all high-purity muons

(d) high-purity muons per event

Figure 6.4: Muon Distributions for all high-purity muons. In (a) the transverse momentum of all muons with respect to the beam spot is shown after the selection of a first high-purity muon. Plot (b) shows pseudorapidity of the high-purity muons. In the lower left histogram (c) the combined isolation variable is illustrated. The multiplicity of high-purity muons in data and simulation in the lower right plot is in very good agreement.

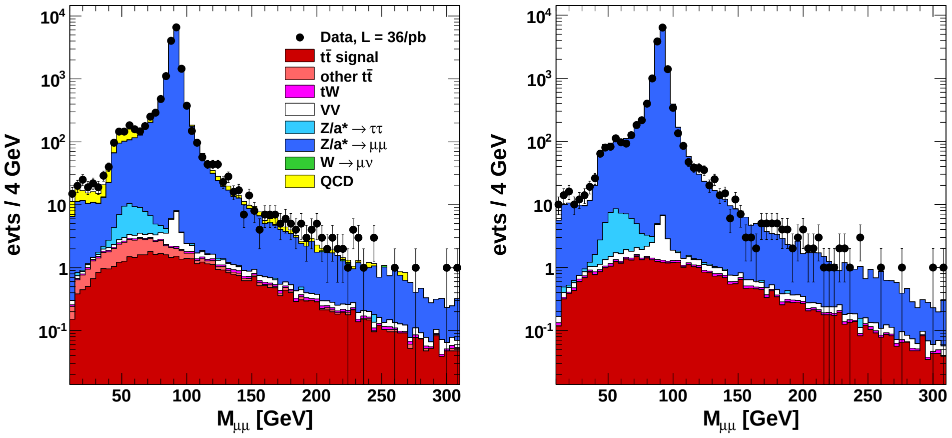

(a) high-purity muons (b) isolated muons

Figure 6.5: Invariant Dimuon Mass. The left histogram shows the reconstructed invariant dimuon mass of the two leading muons for all events were these two muons are oppositely charged. The right plot shows the same distribution after the requirement of muon isolation.

events are removed if the dimuon mass is compatible with the nominal Z^0 mass. The requirement for signal selection is

$$|m_{\mu\mu} - m_Z| > 15\,\mathrm{GeV}. \tag{6.7}$$

Events inside the veto region around the Z^0 peak are also kept separately to estimate the contribution of DY events in the later selection steps. This is described in Section 7.2.2.

6.5 Jet and MET Selection

The $t\bar{t}$ signal is characterised by the presence of energetic hadronic jets originating from the b quarks and softer jets from initial and final state radiation. Most background events are not expected to have such hadronic activity. Therefore, the requirement of jets in the event selection further suppresses the background contribution.

The jets used in this analysis are PF jets reconstructed with the anti-k_T algorithm. On all jets, the relative η-dependent and the absolute p_T-dependent jet energy scale correction are applied in the data as well as in the simulation. Residual corrections are used subsequently for the detector data, as explained in Subsection 5.3.2.

Since also leptons are reconstructed as PF jets, the first step in the jet selection is a cleaning of the jet collection. Jets are removed from the collection if they match one of the isolated muons within $\Delta R < 0.4$. In order to reject

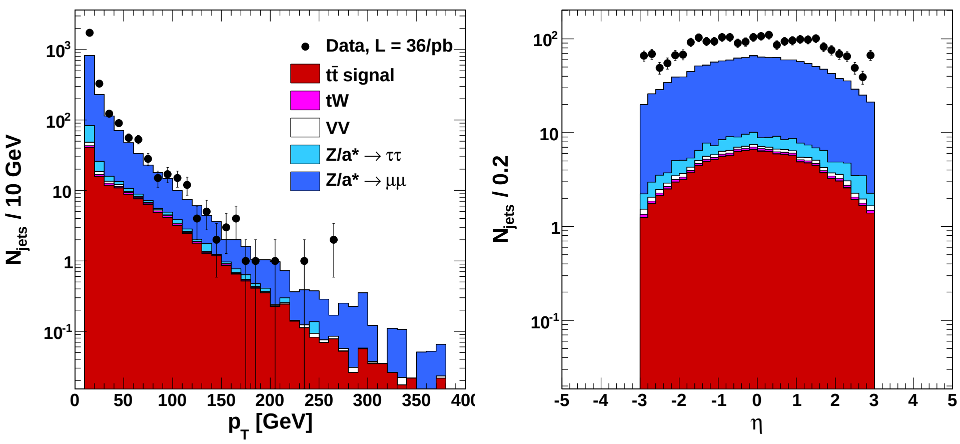

(a) p_{T} of jets with $|\eta| < 3.0$ (b) η of jets with $p_{\mathrm{T}} > 10\,\mathrm{GeV}$

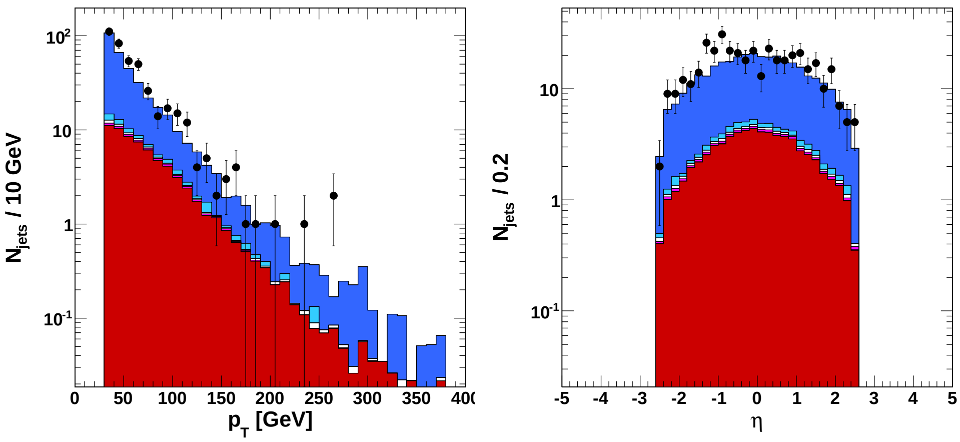

(c) p_{T} of selected jets (d) η of selected jets

Figure 6.6: Jet distributions after Z^0 mass veto. Only jets with $p_{\mathrm{T}} > 10\,\mathrm{GeV}$ and $|\eta| < 3.0$ are filled in the upper histograms. Plot (a) shows the transverse momentum of all jets which fulfil the jet identity selection. The upper right histogram shows the η distribution for these jets. There is an excess of jets at low p_{T}. A comparison of different run ranges with different instantaneous luminosities leads to the conclusion that these additional low-p_{T} jets are from pile-up events. In the lower plots the p_{T} and η distributions of the jets fulfilling the full selection criteria are shown. The agreement between data and simulation is much better after the removal of jets with $p_{\mathrm{T}} < 30\,\mathrm{GeV}$.

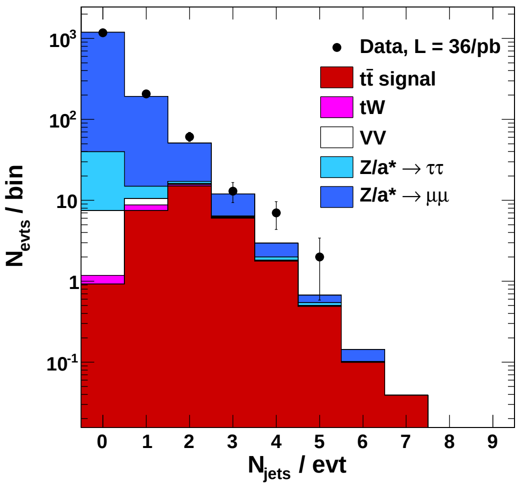

Figure 6.7: Jet multiplicity after Z^0 mass veto. Only the jets which fulfil the selection criteria for jet identity, p_{T} and η are shown in this plot.

fake jets from detector noise, loose jet identity selection criteria are required for all jet candidates. These are basically the requirement of more than one constituent in the jet where at least one of the particles has to be charged [109].

For the signal, two jets are required with $p_{\mathrm{T}} > 30\,\mathrm{GeV}$ and $|\eta| < 2.5$. Although there should be two b jets in the event signature, the default selection does not include b tagging because of its large systematic uncertainty in first data. The feasibility to improve the cross section measurement by requiring one b-tagged jet is investigated in Chapter 10.

Control distributions concerning the jets are shown in Figure 6.6. There is a surplus of soft jets at low p_{T}, which is caused by pile-up events, as can be seen in the upper left histogram. The agreement for jets that fulfil the selection criteria, which are shown in the lower plots, is much better. This can also be seen in Figure 6.7 where the multiplicity of selected jets after the Z^0 veto is displayed.

In order to reject remaining background events, especially from $Z/\gamma^\star \to \mu^+\mu^-$, in the last selection step events are required to have a missing transverse energy $\not\!\!E_{\mathrm{T}} > 30\,\mathrm{GeV}$. In consequence to the use of PF jets, also the $\not\!\!E_{\mathrm{T}}$ used for the selection is reconstructed with the particle flow algorithm. The distribution of $\not\!\!E_{\mathrm{T}}$ is shown in the next chapter in Figure 7.5.

6.6 Event Yields

The number of observed events in data compared to the expected events from the simulation is given in Table 6.2 after each sequential selection step described above:

- 1 muon: events with at least 1 muon passing the trigger, p_{T} , η and muon identification requirements.

sample	**1 h.-pur. muon**	**2 h.-pur. muons**	**2 isolated muons**	**Z^0 veto**	**1 jet**	**2 jets**	**$\not{E}_\mathrm{T}$**
$t\bar{t}$ signal	85.3	47.7	41.2	31.7	30.8	23.4	19.7
other $t\bar{t}$	1037.8	19.9	0.2	0.1	0.1	0.1	0.1
tW	71.1	4.0	3.0	2.3	2.1	0.8	0.7
diboson	91.6	23.6	22.1	8.7	2.4	0.6	0.3
W	196765.1	13.7	0.7	0.6	0.2		
DY→ $\tau\tau$	1756.1	44.4	41.1	38.0	5.6	1.3	0.6
DY→ $\mu\mu$	28952.9	15784.0	15120.9	1364.4	217.7	40.5	3.0
QCD	679701.8	523.9	0.3	0.3	0.1		
Sum	908462	16461	15230	1446	259	67	24.3
Data	854708	16472	15057	1463	290	83	28

Table 6.2: Number of expected signal and background events, compared to the event yields in the $35.9\,\mathrm{pb}^{-1}$ data, after each selection step. Since the QCD sample used in the analysis is already preselected on generator level for muons with $p_\mathrm{T} > 15\,\mathrm{GeV}$, the comparison between data and simulation is performed only after the muon identification requirement.

- 2 muons: events with at least 2 oppositely-charged high-purity muons and $m_{\mu\mu} > 12$ GeV.
- 2 isolated muons: dimuon events surviving the isolation requirements.
- Z^0 veto: events passing the full dimuon selection, including the veto on the Z^0 mass.
- 1 jet: fully selected dimuon events with at least 1 jet fulfilling the jet ID, p_T and η requirements.
- 2 jets: same as the previous one, but requiring at least 2 jets.
- $\not\!\!E_\mathrm{T}$: events surviving the full selection, including the requirement on the missing transverse energy.

There is a good agreement between data and the sum of simulated samples, which further improves after applying a correction to the Drell–Yan background contribution. The selection efficiency for signal events in the simulation is 20.8%. In the next chapter it is investigated for which effects this efficiency has to be corrected and what the systematic uncertainties are.

Chapter 7

Systematic Studies

7.1 Effects on Signal Selection

7.1.1 Trigger Efficiency

For all trigger paths mentioned in Section 6.3, the single-muon trigger efficiency is determined by using the tag-and-probe method on the Z^0-mass peak.

For this study, events containing two oppositely charged muons are selected, for which the same single-muon criteria hold true as described in the previous section. However, the requirement for a minimal transverse muon momentum is lowered to 5 GeV, allowing for a study of the trigger thresholds. Additionally, an invariant mass of the muon pair between 81 GeV and 101 GeV is required.

The HLT muons are matched to the reconstructed muons within a radius of 0.2 in η-ϕ. Events are rejected in which the matching is ambiguous or more than two muon candidates are present. At least one of the two reconstructed muons is required to give rise to a positive trigger decision by matching an L3 muon of the corresponding trigger path. The trigger efficiency is then calculated from the fraction of events in which both muon candidates have matching L3 muons, and those in which only one of the two muon candidates matches an L3 muon.

Figure 7.1 shows the integrated trigger efficiency as well as its distributions as functions of the muon p_{T}, the pseudo-rapidity η, and the number of jets in the event, for simulated and collision data triggered by the individual trigger paths. The trigger efficiencies in the simulation are higher than those obtained from data. Furthermore, the efficiencies are constant functions of the muon p_{T} and do not depend on the number of jets. The trigger efficiency is highest in the barrel region and decreases beyond approximately $|\eta| = 2.1$, where there is no coverage by RPC modules. In the barrel–endcap transition region a slight decrease of the efficiency can be observed.

For $|\eta| < 2.1$ and $p_{\mathrm{T}} > 20\,\mathrm{GeV}$ a trigger efficiency of

$$\epsilon_{\mathrm{trig}} = 91.1 \pm 0.2\% \tag{7.1}$$

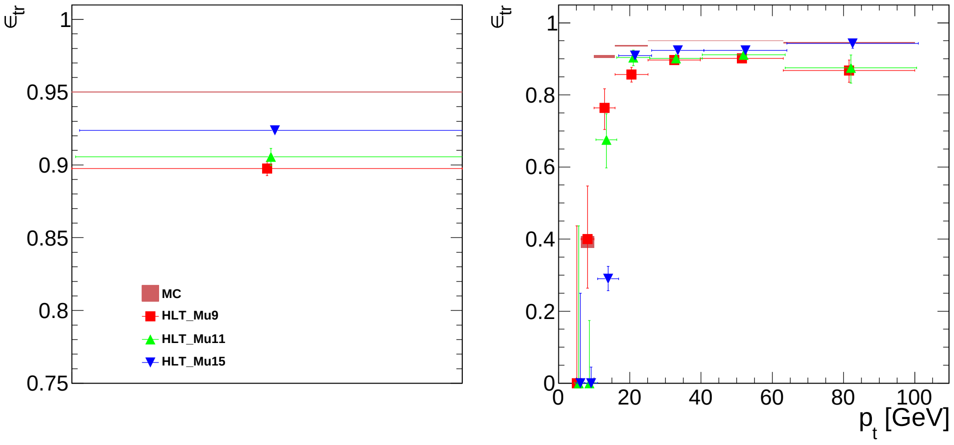

(a) total trigger efficiencies

(b) trigger efficiency in p_{T}

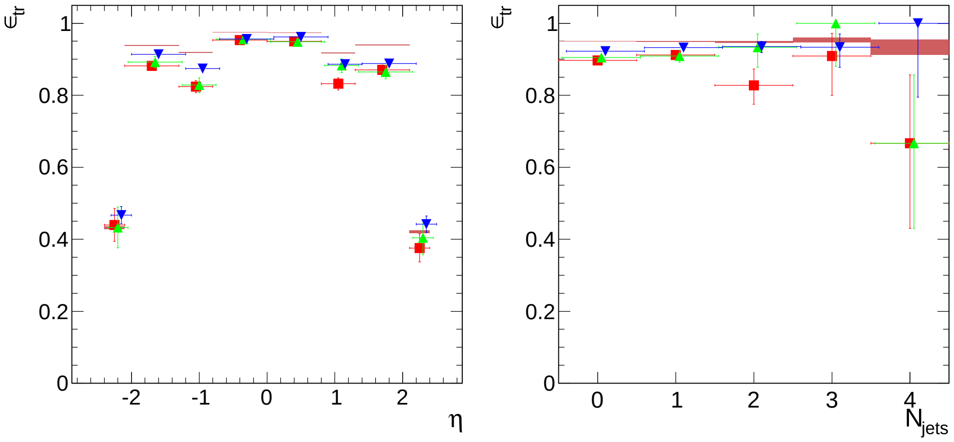

(c) trigger efficiency in η

(d) trigger efficiency in N_{jets}

Figure 7.1: Muon trigger efficiencies in data (markers) and simulation (band).
(a) integrated efficiency for muons with $p_{\mathrm{T}} > 20$ GeV and $|\eta| < 2.1$.
(b) efficiency as a function of p_{T} for muons with $|\eta| < 2.1$.
(c) efficiency as in η for muons with $p_{\mathrm{T}} > 20$ GeV.
(d) efficiency for $p_{\mathrm{T}} > 20$ GeV and $|\eta| < 2.1$ as a function of the number of hard jets in the event. No significant dependency on the number of hard jets is observed.

is obtained for single muons. The efficiencies of the three triggers are weighted with the integrated luminosities of the run period in which the corresponding trigger is used. The simulation yields

$$\epsilon_{\text{trig}}^{\text{MC}} = 95.00 \pm 0.03\%. \tag{7.2}$$

The deviations between the triggers used in data and the simulation are taken as a correction factor to the signal selection efficiency determined from simulation, which enters the $t\bar{t}$ production cross section calculation. Since the shape in η and p_{T} above 20 GeV is the same for all trigger paths, the correction is applied by using a global correction factor. The deviation between the trigger efficiency in data and simulation is also taken as systematic uncertainty. This is more conservative than taking the statistical errors of the single measurements, but nevertheless small. However, the difference of 3.9% between the single muon efficiencies translates into only a small correction if the trigger is required for only one of the two muons in the event.

According to [110], an additional effect has to be taken into account that cannot be evaluated using the tag-and-probe method. For some events, the L1 initialises the event read-out for the bunch crossing earlier than when the actual collision occurred. This is called pre-firing. In this case, all muon hits are lost for the event. A correction factor of $\epsilon_{\text{pre}} = 0.990 \pm 0.006$ has therefore to be applied to the total trigger efficiency in data.

The total correction factor for events with two muons is calculated using

$$\mathcal{C}_{\text{trig}} = \epsilon_{\text{pre}} \frac{1-(1-\epsilon_{\text{trig}})^2}{1-(1-\epsilon_{\text{trig}}^{\text{MC}})^2} = 0.986 \pm 0.007 \tag{7.3}$$

resulting in a correction of about 1.4% to the efficiency of the signal selection.

7.1.2 Muon Efficiencies

For the muon selection efficiency, results from [111] are used which are also applied for the upcoming publication [8]. A tag-and-probe method similar to the one described in the previous section is used for the determination of these corrections. The scale factor per muon is found to be

$$\mathcal{C}_{\mu} = 0.9920 \pm 0.0054 \tag{7.4}$$

taking into account reconstruction, identification, and isolation efficiency. The efficiency for the isolation is measured in Z^0 events, which have a topology different from that of the $t\bar{t}$ signal. Because the result has to be transferred from Z^0 to $t\bar{t}$ events, an additional error of 2% per muon is assumed.

This leads to a global correction factor of

$$\mathcal{C}_{\mu\mu} = 0.984 \pm 0.011\,(\text{tag-and-probe}) \pm 0.040\,(\text{isolation}) \tag{7.5}$$

for both muons.

7.1.3 Pile-Up

The presence of pile-up events, additional proton–proton collisions in the same bunch crossing as the collision under study, leads to several effects that have to be taken into account. Pile-up events depose extra energy in the calorimeter and affect in this way the isolation of the muons, the jet energy scale, and the missing transverse energy.

The effect on the muon isolation is already considered in the muon efficiency and its uncertainty, which is measured with the tag-and-probe method. The influence on the jet energy scale is also taken into account by adding additional uncertainty to it. The background is estimated from data as discussed in the next section. In this subsection, the influence of pile-up events on the selection efficiency of the signal is discussed.

In order to correct the signal selection efficiency for pile-up effects, the result from [112] is used. The $\not{E}_{\mathrm{T}}$ distributions of $Z \to \mu^+\mu^-$events in data and simulation are compared in that study. Since there are no neutrinos expected in these events and hence no source for real missing energy, the measured $\not{E}_{\mathrm{T}}$ is exclusively from pile-up and mismeasurement of the jet energies. The missing transverse energy in the simulated events is then shifted and smeared to match the $\not{E}_{\mathrm{T}}$ in the real data events. Smearing is done as a function of the number of hard jets or the total sum of deposed energy in the calorimeters.

After an appropriate smearing has been found for DY events, the same smearing is applied on the non-neutrino contribution of $\not{E}_{\mathrm{T}}$ in simulated signal events. In the dimuon $t\bar{t}$ simulation, the transverse momenta of the generated neutrinos are subtracted from the reconstructed $\not{E}_{\mathrm{T}}$ and the smearing is applied on the remaining part of $\not{E}_{\mathrm{T}}$. After that, the neutrino momenta are added again. This way a simulation sample with a realistic description of fake-$\not{E}_{\mathrm{T}}$ is obtained. The total signal selection efficiency in this pile-up corrected sample is about 1.1% higher than in the original sample.

This result is cross checked by using another simulation sample in which pile-up is simulated. Figure 7.2 shows the number of primary vertices per bunch crossing in data, in the simulation without pile-up, and in the simulation with pile-up. As can be seen, the pile-up simulation overestimates the number of proton–proton collisions per bunch crossing. The signal selection efficiency in this sample is about 1.5% higher than in the simulation without pile-up. This is consistent with the result above.

Hence, for the calculation of the cross section a correction factor of

$$\mathcal{C}_{\mathrm{PU}} = 1.011 \pm 0.011 \tag{7.6}$$

on the selection efficiency is used. The size of the correction is also assumed as uncertainty.

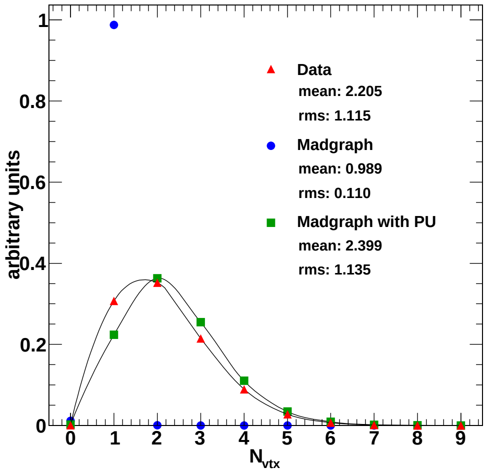

Figure 7.2: Number of primary vertices in data, default simulation samples and samples with extra pile-up events.

7.1.4 Jet Energy Scale

In order to determine the uncertainty due to the jet energy scale (JES), the p_{T}- and η-dependent JES uncertainties provided by the CMS jet group [105] are used, which are of the order of few percent for high energy jets. Additional uncertainties are subsequently added in quadrature: an uncertainty of 5% is assumed for the b jet scale, 1% uncertainty for pile-up, and 1.5% uncertainty due to the different software version used to determine the energy corrections. The simulation is run with the jet four-momenta being scaled up and down by the quadratic sum of all these uncertainties. The vectorial changes of the jet momenta are propagated to the missing transverse energy. The JES variation affects the selection efficiency of the signal as well as those of the backgrounds. With the rescaled simulation samples, the signal selection efficiency is recalculated and the difference to the original efficiency is taken as systematic uncertainty of the JES.

However, this procedure does not take into account the $\not{E}_{\mathrm{T}}$ uncertainty from calorimeter energy that is not clustered in jets, which has to be treated separately. For this reason, the $\not{E}_{\mathrm{T}}$ from unclustered energy is scaled up and down by 10% and the impact of this scaling on the signal selection efficiency is added in quadrature to the one from the jet scaling. However, the uncertainty due to unclustered missing transverse energy is much lower than that from the JES variation and therefore negligible.

The uncertainties on the selection efficiency from JES uncertainty are shown in Table 7.1.

scaling	**default**	**JES up**	**JES down**	**$\not{E}_{\mathrm{T}}^{\mathrm{uncl}}$ up**	**$\not{E}_{\mathrm{T}}^{\mathrm{uncl}}$ down**
ϵ_{sig}	0.2081	0.2171	0.1966	0.2073	0.2082
σ_{JES}		+0.0440	-0.0550	-0.0035	+0.0004

Table 7.1: JES uncertainties. The selection efficiencies ϵ_{sig} for signal events are shown as well as the relative deviations from the unscaled efficiency.

7.1.5 Other Uncertainties

The additional uncertainties on the signal selection efficiency are small. The theoretical uncertainties due to initial and final state radiation, the hadronisation and renormalisation scale Q^2, and the the matrix-element/parton-shower matching threshold of MadGraph are investigated using special simulation samples with the corresponding quantities being varied up and down by a factor of two with respect to their default values [8] [113].

The effect of varying the amount of initial and final state radiation is found to be about 3%. The uncertainty from the Q^2 scale of the hard process gives 2% uncertainty, the variation of the matching gives the same result.

Another source of systematic uncertainty is the ingoing parton distribution functions. Regarding to external studies done for [8], this uncertainty is smaller than 1% and hence negligibly small. For those studies, the simulated signal events have been reweighted according to the uncertainties of the PDF values of their interacting partons.

The mass of the top quark is a quantity that affects the angular distributions of the $t\bar{t}$-decay products and hence the geometrical acceptance of the signal. In order to study this effect, two simulation samples with generated top quark masses of 166.5 and 178.5 GeV have been used, i.e. 6 GeV less respectively more than the default mass of 172.5 GeV used in this analysis. An uncertainty of 7.4% is found for this variation of the top quark mass. Because the mass variation of 6 GeV is much higher than the uncertainty of the measured mass from Tevatron (see Subsection 2.3.6), an uncertainty of only 2.5% is assumed for the acceptance.

The branching fractions for $W \to \ell\nu$ and $\tau \to \mu\nu\nu$ are taken from [10]. The branching fraction of $b_{W\to\ell\nu} = 0.1080 \pm 0.0009$ is taken for the muon and for the tau decay fraction. The branching fraction for tauons decaying into a muon is given by $b_{\tau\to\mu\nu\nu} = 0.1772 \pm 0.0005$. With this values, the inclusive branching fraction of $t\bar{t}$ events into final states with two muons is

$$b_{t\bar{t}\to\mu\mu X} = 0.01616 \pm 0.00023. \tag{7.7}$$

The relative error on the cross section from the uncertainty of this branching fraction is 1.5%.

7.2 Background

7.2.1 QCD and Fake Muon Background

The *wrong-charge method* is used to determine the contribution from events with wrongly identified muons (punch-through, decay-in-flight, ...) or muons from heavy quarks which are coincidentally isolated. It is based on the number of selected events with two equally charged muons. The method covers all

selection	**default**	**loose**	**very loose**
p_T	$> 20\,\mathrm{GeV}$	$> 20\,\mathrm{GeV}$	$> 20\,\mathrm{GeV}$
$\|\eta\|$	< 2.4	< 2.4	< 2.4
isGlobalMuon	true	-	-
isTrackerMuon	true	true	true
$N_\mathrm{trk\ hits}$	> 10	> 10	> 10
$N_\mathrm{muon\ hits}$	> 0	-	-
$\|d_0^{BS}\|$	< 0.02	-	-
χ^2/ndof	$< 10.$	-	-
$m_{\mu\mu}$	$> 12\,\mathrm{GeV}$	$> 12\,\mathrm{GeV}$	$> 12\,\mathrm{GeV}$
I_{comb}	< 015	< 0.15	< 0.30

Table 7.2: Comparison between the default selection used for the cross section measurement and the “loose” selection used for the background estimation. A “very loose” selection with a diminished isolation requirement is also shown.

processes which are not expected to produce two oppositely charged isolated muons. In the following, events with equally charged muons are referred to as *wrong-charge events* while events with oppositely charged muons (as produced in the signal events) are denoted as *right-charge events*.

Only one event with two isolated muons of same charge is observed in the 2010 data, which, however, fails to fulfil the 2-jet requirement. Therefore, only an upper limit to the number of QCD events and background events with wrongly reconstructed muons of opposite charge, $\mathrm{N}^\mathrm{BG}_\mathrm{right}$, can be calculated. This requires as a first step an estimate for the upper limit of the number of wrong-charge events, $\mathrm{N}^\mathrm{BG}_\mathrm{wrong}$.

In order to estimate the efficiencies of the jet and $\not\!\!E_\mathrm{T}$ selections, a “looser” selection with diminished muon quality requirements is applied. This is justified by the expectation that the hadronic activity in the event is uncorrelated with the properties of the wrongly reconstructed muons. A comparison between the “loose” selection and the default selection is shown in Table 7.2. Two isolated tracker muons with p_T and η requirements as described in the previous section and corresponding tracks with at least ten hits in the tracker are selected. The “loose” selection increases the yield of wrong-charge events by approximately a factor of five. The number of selected events is shown in Table 7.3. The number of events passing all requirements of the “loose” selection is still zero after the selection of two jets, such that the efficiency of the $\not\!\!E_\mathrm{T}$ requirement cannot be determined.

According to Poissonian statistics, the 1σ upper limit for the number of events in a counting experiment with a result of zero is 1.148. In order to reduce this value for the default selection, it is multiplied by the ratio of the numbers of wrong-charge events in both default and “loose” selections. Thus, the upper limit for the number of wrong-charge events is given by

$$N^\mathrm{bg}_\mathrm{wrong} < 1.148 \times \frac{278}{1260} = 0.253 \quad \text{with } 68\%\ \mathrm{C.\,L.} \tag{7.8}$$

selection	**default**	**loose**	**very loose**
2 muons, $m_{\mu\mu} > 12\,\text{GeV}$	278	1260	1260
2 iso muons	1	4	13
Z^0 veto	1	2	9
1 jet	1	2	9
2 jets	0	0	5
$\not{E}_\text{T}$	0	0	0

Table 7.3: Number of events with two equally charged (*wrong-charge*) muons in data for the default analysis selection, a selection with looser muon requirements, and a very loose selection with $\text{I}_\text{comb} < 0.3$.

In order to finally obtain an estimate for the number of QCD and fake-muon background events, $\text{N}^\text{BG}_\text{right}$, the ratio $R^\text{MC}_\text{r,w}$ between the number of right-charge and wrong-charge events in the QCD muon-enriched simulated sample before the muon isolation requirement is calculated. A value of

$$R^\text{MC}_\text{r,w} = 2.38 \tag{7.9}$$

is found in the simulation sample. This value can be seen as an upper limit, since in data this ratio should be lower. Since the simulated sample is already muon-enriched on generator level, in most of the events after the selection of two muon candidates both candidates should match to two generator muons with partially correlated charge. Events with two fake muons that are not simulated would lower this ratio. This is due to the fact that in those events one would expect the charge of the muons to be almost uncorrelated and the ratio between the number of right-charge and wrong-charge events to be close to one.

Muons with wrongly identified charge, which would also lower the ratio, can be neglected in the simulation. If the charge identification in data is worse than in the simulation, this would lead to a larger number of wrong-charge events and therefore to a higher upper limit on the expectation value. This would then result in an even more conservative estimation.

The plausibility of the ratio $R^\text{MC}_\text{r,w}$ can be verified from the distributions in Figure 7.3, which are mostly dominated by QCD background. For the isolation variable (right-charge events), distributions from data and simulation are well in agreement while for the invariant mass (wrong-charge events), there is a small excess of data events with respect to the simulation, possibly due to double-fake events. Since this excess is small, it can be concluded that at least for non-isolated muons the ratio between right-charge and wrong-charge events in data is only slightly smaller than in the simulation. Thus, the deviation of $R_\text{r,w}$ between data and simulation should be small.

The upper limit for the number of selected QCD and fake muons events with oppositely charged muons becomes

$$N^\text{bg}_\text{right} < 1.148 \times \frac{278}{1260} \times 2.38 = 0.60 \quad \text{with } 68\%\ \text{C. L.} \tag{7.10}$$

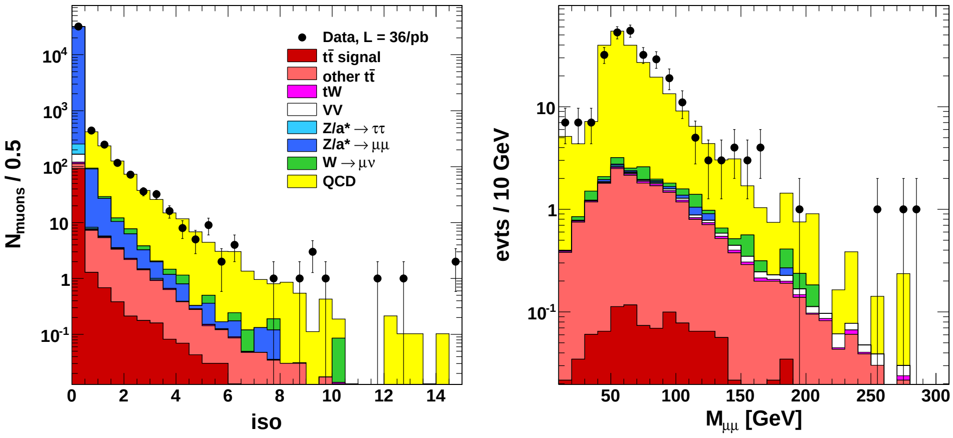

(a) muon isolation for events with a right-charge muon pair

(b) invariant mass of wrong-charge di-muon pairs mass

Figure 7.3: QCD dominated Plots. Left: relative muon isolation distribution for events with two oppositely charged muons before the isolation requirement. Right: invariant dimuon mass distribution for wrong-charge events before the isolation requirement.

It must be pointed out that this is the upper limit for the number of background events before applying the $\not{E}_T$ requirement, for which no efficiency can be calculated. The right column of Table 7.2 shows the values for a "very loose" selection for which the isolation requirement is released from 0.15 to 0.30. The corresponding event numbers are given in Table 7.3. In this case, applying the $\not{E}_T$ requirement reduces the number of wrong-charge events from five to zero. Therefore, it can be assumed that this requirement further reduces the QCD and fake muon background by almost one order of magnitude, which implies $N^{\mathrm{bg}}_{\mathrm{right}} \lesssim 0.1$. However, for this work the value of $N^{\mathrm{bg}}_{\mathrm{right}} < 0.60$ is chosen as a conservative background estimate because the muon isolation is expected to be correlated with the missing transverse energy. This limit will be improved when more data become available and unbiased statements about the implications of the $\not{E}_T$ requirement can be made.

The method described above can only be deployed if no wrong-charge events pass all requirements. Otherwise, the mean value of the background expectation can also be calculated; the current estimate of $R^{\mathrm{MC}}_{\mathrm{r,l}}$ must then be considered as an overestimation of the background and should instead be extracted from data.

7.2.2 Drell–Yan Background

The Drell–Yan contribution to the background is normalised to the data using events with an invariant dimuon mass in the Z^0 veto region between 76 GeV and 106 GeV, which is excluded for signal selection. From the selected data, all

cut	**Z^0 veto**	**1 jet**	**2 jets**	**$\not{E}_T$**
$\mathcal{C}_{\rm DY}$	0.986 ± 0.009	1.059 ± 0.024	1.162 ± 0.060	2.931 ± 0.549
$R^{\rm MC}_{\rm out/in}$	0.099 ± 0.001	0.115 ± 0.002	0.117 ± 0.004	0.241 ± 0.031

Table 7.4: Scaling factors $\mathcal{C}_{\rm DY}$ and ratio $R^{\rm MC}_{\rm out/in}$ between simulated events outside and inside the Z^0 veto region for $Z/\gamma^\star \to \mu^+\mu^-$.

simulated contributions are subtracted except for $Z/\gamma^\star \to \mu^+\mu^-$ (Drell–Yan events from $Z/\gamma^\star \to \tau^+\tau^- \to \mu^+\mu^-\ 4\nu$ can be neglected in this invariant mass region). The simulated Z^0 peak is subsequently scaled to this distribution so that the integral over both distributions is equal. This effectively means that the $Z \to \mu^+\mu^-$ contribution is rescaled with a correction factor $\mathcal{C}_{\rm DY}$ to match with the data while the other contributions stay fixed. The DY contribution outside the Z^0-mass veto region is estimated by applying the same correction factor on the simulated DY background outside the veto region.

The most important distribution to be subtracted is the $t\bar{t}$ signal, which has to be weighted using an assumed cross section. Since this cross section is exactly the quantity which is to be measured, one cannot take the calculated NLO cross section to determine the weight since this would bias the final result. For this reason, the NLO $t\bar{t}$ cross section is taken only as initial estimate to get a first measured value. This value is then used to reweight the $t\bar{t}$ contribution iteratively. After only few iterations the difference between the new and the previous value of the $t\bar{t}$ cross section is on the per mille level.

The correction factors $\mathcal{C}_{\rm DY}$ after different selection steps are shown in the first line of Table 7.4. While during the first selection steps the correction factor inside the Z^0 mass region is of the order of few percent, it becomes larger with the requirements of jets and missing transverse energy. After the full jet selection, a correction factor of 1.162 ± 0.060 is found. The requirement on the $\not{E}_T$ increases the value to 2.931 ± 0.549. The large error of the correction factor after the complete selection is mainly caused by the small yield in data, since only 43 events pass the $\not{E}_T$ selection. Additional uncertainties contributing to the correction factor are the non-DY contributions that are subtracted from the data. This is mainly the $t\bar{t}$ contribution that is taken from the simulation but weighted with the measured cross section.

It has to be assumed for this method that the shape of the invariant dilepton mass is well described by the simulation. This is verified in [114] after the selection of two isolated muons. In that analysis note, the cross section for Z^0 production is measured in the invariant mass window between 60 GeV and 120 GeV. If signal events are only selected between 76 GeV and 106 GeV and the simulation is used to extrapolate to the wider mass window, then the measured cross section differs by only 0.3% with respect to the selection in the whole mass window due to the difference between data and simulation.

However, the shape of the DY mass spectrum does also depend on the subsequent selection of jets and $\not{E}_T$. The ratio $R^{\rm MC}_{\rm out/in}$ between DY events outside and inside the Z^0 veto region changes from 0.099 ± 0.001 to 0.241 ± 0.031

in the simulation if the jet and $\not\!\!E_{\mathrm{T}}$ requirements are applied after the selection of two isolated muons. This effect shows up to be the main source of uncertainty of this method. The values $R^{\mathrm{MC}}_{\mathrm{out/in}}$ after different selection steps are shown in the second line of Table 7.4.

There are several reasons why DY events can pass the $\not\!\!E_{\mathrm{T}}$ requirement although there is no natural source of $\not\!\!E_{\mathrm{T}}$ in these events. Missing energy can be faked by wrong jet energy scaling, by pile-up events, or by momentum mismeasurement of the muons. The latter effect might be the reason for the dependency of $R_{\mathrm{out/in}}$ on the $\not\!\!E_{\mathrm{T}}$ requirement. If one of the muon momenta is determined wrongly, this mismeasurement is directly propagated to the $\not\!\!E_{\mathrm{T}}$ value. For this reason, DY events preferentially survive the event selection where the momentum of at least one muon is measured incorrectly although in general the momentum resolution is excellent and the contribution of these events might be small. Simultaneously, the reconstructed dimuon mass $m_{\mu\mu}$ is shifted in these events. This effect leads to a migration of events out of the Z^0 mass region, resulting in an increase of $R_{\mathrm{out/in}}$ after the $\not\!\!E_{\mathrm{T}}$ selection.

It is not yet clear if this effect is correctly modelled in the simulation and where the mismeasurement of the muon momentum comes from. It is either possible that the muon tracks in these events are not measured sufficiently well or that these muons are from the tails of the dE/dx-Landau distribution and lose energy by emitting hard photons while crossing the calorimeter material. This has to be studied in the future. For this reason, a 50% uncertainty on the DY background after the selection of $\not\!\!E_{\mathrm{T}}$ is assumed, which is in agreement with other CMS analyses like [110] and [5]. The large correction factor of almost three after the selection of $\not\!\!E_{\mathrm{T}}$, which cannot be explained with a statistical fluctuation, is evidence that the modelling of fake $\not\!\!E_{\mathrm{T}}$ in the simulation is not understood well enough. The uncertainty on the DY background is by far the largest systematic uncertainty on the $t\bar{t}$ cross section.

The $Z/\gamma^{\star} \rightarrow \mu^+\mu^-$ events are corrected with the correction factor calculated after the full selection requirement while for the $Z/\gamma^{\star} \rightarrow \tau^+\tau^-$ events the correction factor after the requirement of two jets (without $\not\!\!E_{\mathrm{T}}$ requirement) is assumed to be the best choice. This different treatment is motivated by the presence of neutrinos from tau decays in the final state which give a source of natural missing transverse energy. The invariant mass distribution with the corrected Drell–Yan contribution is displayed in Figure 7.4 for data and simulation after the full event selection. In Figure 7.5 the distribution of the missing transverse energy after the two-jet selection is shown before (left) and after applying the correction (right). The agreement in the DY dominated region at low $\not\!\!E_{\mathrm{T}}$ increases after the correction.

Table 7.5 shows the event yields for data and simulation with the corrected Drell–Yan contributions after each selection step. The agreement between the event numbers in data and in the summed simulation samples improves after applying the correction, as compared to the uncorrected event numbers given in Table 6.2.

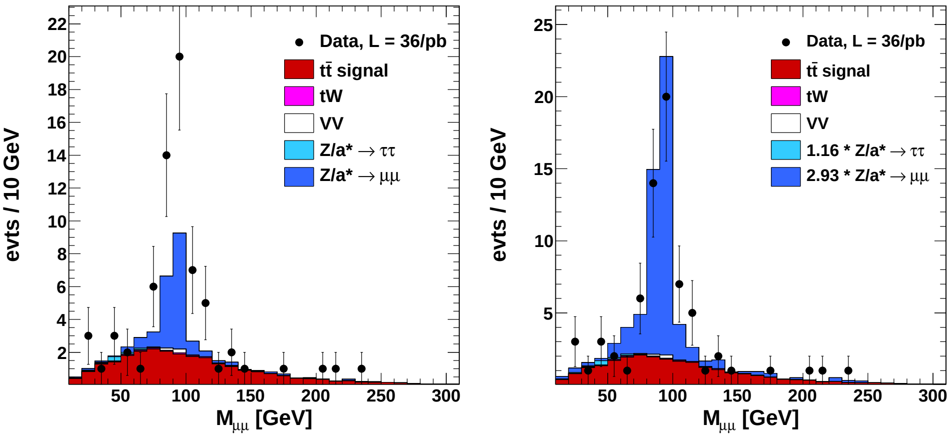

(a) before correction (b) after correction

Figure 7.4: Invariant dimuon mass distribution for events surviving the full event selection in 35.9 pb^{-1} of integrated luminosity (dots), compared to the simulation prediction (histograms). The $Z/\gamma^\star \rightarrow \mu^+\mu^-$ contribution is scaled up by a factor of 2.93 and the $Z/\gamma^\star \rightarrow \tau^+\tau^-$ by a factor of 1.16.

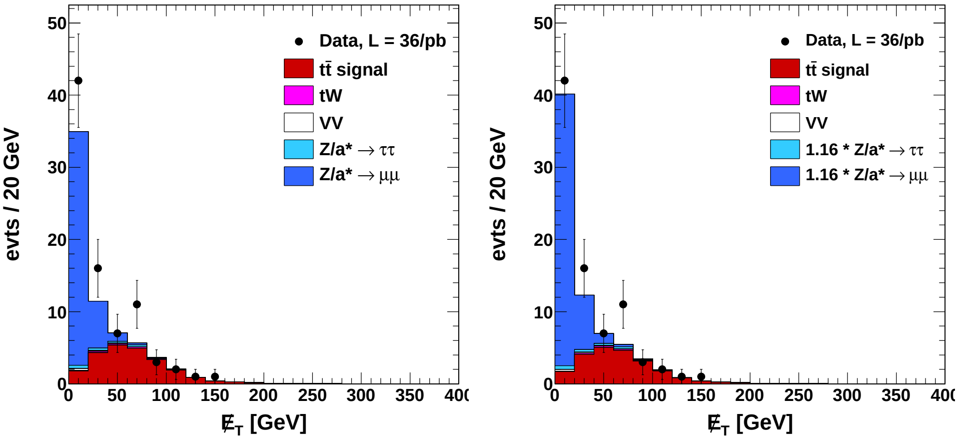

(a) before correction (b) after correction

Figure 7.5: Missing transverse energy for events surviving the jet selection criteria in 35.9 pb^{-1} of integrated luminosity, compared to the simulation prediction. The simulated distributions are shown before and after applying the correction of the Drell–Yan contribution.

sample	**1 h.-pur. muon**	**2 h.-pur. muons**	**2 isolated muons**	Z^0 **veto**	**1 jet**	**2 jets**	$\not\!\!E_\mathrm{T}$
$t\bar{t}$ signal	85.3	47.7	41.2	31.7	30.8	23.4	19.7
other $t\bar{t}$	1037.8	19.9	0.2	0.1	0.1	0.1	0.1
tW	71.1	4.0	3.0	2.3	2.1	0.8	0.7
diboson	91.6	23.6	22.1	8.7	2.4	0.6	0.3
W	196765.1	13.7	0.7	0.6	0.2		
DY→ $\tau\tau$	1756.1	44.4	40.6	37.5	6.0	1.5	0.6
DY→ $\mu\mu$	28952.9	15795.1	14943.9	1345.7	230.6	47.1	8.9
QCD	679701.8	523.9	0.3	0.3	0.1		
Sum	908462	16472	15052	1427	272	73	30.2
Data	854708	16472	15057	1463	290	83	28

Table 7.5: Number of expected signal and background events, compared to the event yields in the 35.9 pb^{-1} data, after each selection step. The correction for the DY contribution is taken into account. Since the QCD sample used in the analysis is already preselected on generator level for muons with $p_\mathrm{T} > 15\,\mathrm{GeV}$, the comparison between data and simulation is performed only after the muon identification requirement.

7.2.3 Other Background Processes

For the remaining background processes that are expected to produce pairs of isolated muons, the simulation is used to estimate the contributions after the full events selection. These backgrounds are associated single top production and production of two gauge bosons W^+W^-, $W^\pm Z^0$, and Z^0Z^0. However, the cross sections and hence also the contributions of all these processes are small. There are only 0.95 expected events after the whole selection. For these contributions a systematic uncertainty of 30% is assumed. Like the estimated uncertainty on the Drell–Yan background, this estimate is in agreement with other studies [8] [110].

Chapter 8

Cross Section Calculation

8.1 Calculation of the Mean Value

After the selection of two isolated oppositely charged muons, two jets, and missing transverse energy, there are 28 candidate events left in data. From this number of observed events N_{obs}, the amount of estimated background events N_{bg}, the signal selection efficiency ϵ_{sig}, the decay branching fraction of $t\bar{t}$ pairs into two-muon final states $b_{t\bar{t}\to\mu\mu X}$, and the integrated luminosity L the production cross section for top–antitop pairs $\sigma_{t\bar{t}}$ is calculated. It is assumed that the number of signal event N_{sig} is given by the excess of selected events over the expected background. As a control distribution Figure 8.1 shows the jet multiplicity for selected events.

Regarding to the formulae 3.1 and 3.2, the cross section $\sigma_{t\bar{t}}$ is given by the ratio of produced $t\bar{t}$ pairs $N_{t\bar{t}}$ and the integrated luminosity. The number $N_{t\bar{t}}$ can be calculated from known quantities:

$$\sigma_{t\bar{t}} = \frac{N_{t\bar{t}}}{L} = \frac{N_{\mathrm{sig}}}{b_{t\bar{t}\to\mu\mu X}\, L} = \frac{N_{\mathrm{obs}} - N_{\mathrm{bg}}}{\epsilon_{\mathrm{sig}}\, b_{t\bar{t}\to\mu\mu X}\, L}. \tag{8.1}$$

The estimated number of background events determined with the methods described in the previous chapter is summarised in Table 8.1. The background amounts to 10.43 events with an uncertainty around 45%. For the error of the background the 50 % uncertainties on the Drell–Yan background are added linearly since they have been determined with the same method. Also the background uncertainties for diboson and associated single top W production which are taken from simulation are summed up. The uncertainties of the DY background and the backgrounds taken from simulation are then added in quadrature. All remaining background contributions are covered by the wrong-charge method. The upper limit of 0.6 events is also added to the positive uncertainty of the background in quadrature.

The selection efficiency is taken from the simulated signal sample and is corrected for the trigger and muon selection efficiencies and for pile-up effects

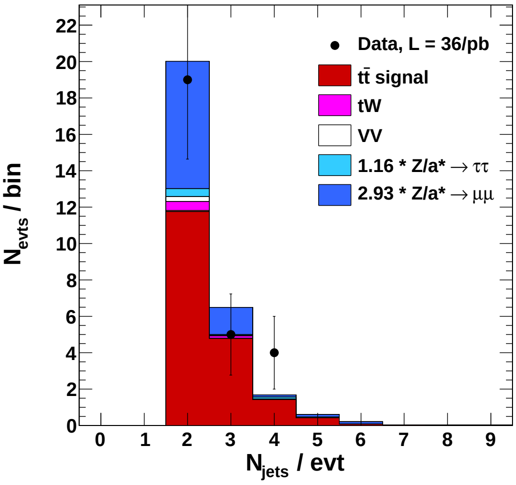

Figure 8.1: Jet multiplicity for selected events. The Drell–Yan contribution has been corrected using the method described in Subsection 7.2.2.

background	contribution [evts]
$Z/\gamma^\star \to \mu^+\mu^-$	8.86 ± 4.43
$Z/\gamma^\star \to \tau^+\tau^-$	0.63 ± 0.32
tW	0.65 ± 0.20
VV	0.29 ± 0.09
other	$0.00\ ^{+0.60}_{-0.00}$
sum	$10.43\ ^{+4.79}_{-4.75}$

Table 8.1: Background summary.

on the $\not{E}_{\mathrm{T}}$ distribution. The corrected efficiency with all systematic uncertainties given by

$$\epsilon_{\mathrm{sig}} = \epsilon_{\mathrm{sig}}^{\mathrm{MC}} \times \mathcal{C}_{\mathrm{trig}} \times \mathcal{C}_{\mu\mu} \times \mathcal{C}_{\mathrm{PU}} = 0.204\ ^{+0.017}_{-0.016} \tag{8.2}$$

is about 2% lower than the value from the simulation.

With the luminosity of 35.9 pb and a branching fraction of 1.616%, a mean value of 148.4 pb is obtained for the $t\bar{t}$ production cross section.

8.2 Summary of Systematics

A summary of all uncertainties discussed in the previous chapter is given in Table 8.2. The total error is still dominated by the statistical uncertainty due to the small number of observed events. The largest systematic uncertainty is the amount of background, which is predominantly from Drell–Yan events. The $\not{E}_{\mathrm{T}}$ uncertainty due to pile-up in the table contains only the impact on the signal acceptance. Pile-up effects on the backgrounds are already contained in their individual uncertainties. The trigger uncertainty includes the uncertainty from the tag-and-probe measurement as well as the pre-firing uncertainty. The uncertainty on the muon efficiency is dominated by the error on the muon isolation which is extrapolated from Drell–Yan events to signal events.

source	**value [%]**	**value [pb]**
statistics	±30.1	±44.7
background	$+27.1/-27.3$	$+40.1/-40.5$
JES	$+5.5/-4.4$	$+8.2/-6.5$
$\not\!\!E_{\mathrm{T}}$ from PU	±1.1	±1.6
trigger	±0.7	±1.1
muons	±4.2	±6.2
mass	±2.5	±3.7
Q^2 scale	±2.0	±3.0
ISR/FSR	±3.0	±4.5
ME/PS thresh.	±2.0	±3.0
$b_{t\bar{t}\to\mu\mu X}$	±1.5	±2.2
luminosity	±4.0	±5.9

Table 8.2: Overview of all uncertainties after default selection of two isolated muons, two jets and $\not\!\!E_{\mathrm{T}}$. The uncertainties are given in per cent of the $t\bar{t}$ cross section and in pb.

The result for the cross section after the event selection is

$$\sigma_{t\bar{t}}^{\mathrm{default}} = 148 \pm 45\ (\mathrm{stat.}) \pm 42\ (\mathrm{syst.}) \pm 6\ (\mathrm{lumi.})\,\mathrm{pb}. \tag{8.3}$$

The total relative uncertainty of the result is 42%.

Chapter 9

Kinematic Event Reconstruction

9.1 Method

In order to validate the top-like topology of the selected events and to obtain a discriminator for the top quark mass, a kinematic reconstruction algorithm [115] is applied on all selected events with two isolated muons, jets, and missing transverse energy. Since a solution of the event kinematics is not guaranteed for all events, the feasibility of using this method to further reject background events and improve the significance of the signal is investigated.

It turns out that the probability of finding a kinematic solution is higher for signal than for background events. A cross section value is calculated from the number of events that have a solution which is compared to the one obtained with the default selection.

9.1.1 Calculation of Mass Solutions

The masses of the top quark and the antitop quark are given by the four-momenta of their decay products:

$$\begin{aligned} m_t^2 &= (E_{\ell^+} + E_\nu + E_b)^2 - (p_{\mathrm{x},\ell^+} + p_{\mathrm{x},\nu} + p_{\mathrm{x},b})^2 \\ &\quad -(p_{\mathrm{y},\ell^+} + p_{\mathrm{y},\nu} + p_{\mathrm{y},b})^2 - (p_{\mathrm{z},\ell^+} + p_{\mathrm{z},\nu} + p_{\mathrm{z},b})^2 \qquad (9.1) \\ m_{\bar{t}}^2 &= (E_{\ell^-} + E_{\overline{\nu}} + E_{\overline{b}})^2 - (p_{\mathrm{x},\ell^-} + p_{\mathrm{x},\overline{\nu}} + p_{\mathrm{x},\overline{b}})^2 \\ &\quad -(p_{\mathrm{y},\ell^-} + p_{\mathrm{y},\overline{\nu}} + p_{\mathrm{y},\overline{b}})^2 - (p_{\mathrm{z},\ell^-} + p_{\mathrm{z},\overline{\nu}} + p_{\mathrm{z},\overline{b}})^2. \qquad (9.2) \end{aligned}$$

Due to the presence of the two neutrinos, which cannot be observed in the detector, the event kinematics of the $t\bar{t}$ system are underconstrained. The six missing momentum components can partly be compensated by additional boundary constraints. Assuming that the missing transverse energy is entirely caused by the two neutrinos, one obtains

$$\begin{aligned} \not{E}_{\mathrm{x}} &= p_{\mathrm{x},\nu} + p_{\mathrm{x},\overline{\nu}} \\ \not{E}_{\mathrm{y}} &= p_{\mathrm{y},\nu} + p_{\mathrm{y},\overline{\nu}} \end{aligned} \tag{9.3}$$

which eliminates two missing variables. In addition, the four-momenta of each muon and the corresponding neutrino from the same top branch give the W boson mass of 80.4 GeV. This provides two additional constraints:

$$\begin{aligned} m^2_{W^+} &= (E_{\ell^+} + E_\nu)^2 \\ &\quad -(p_{\mathrm{x},\ell^+} + p_{\mathrm{x}.\nu})^2 - (p_{\mathrm{y},\ell^+} + p_{\mathrm{y},\nu})^2 - (p_{\mathrm{z},\ell^+} + p_{\mathrm{z},\nu})^2 \qquad (9.4) \\ m^2_{W^-} &= (E_{\ell^-} + E_{\overline{\nu}})^2 \\ &\quad -(p_{\mathrm{x},\ell^-} + p_{\mathrm{x},\overline{\nu}})^2 - (p_{\mathrm{y},\ell^-} + p_{\mathrm{y},\overline{\nu}})^2 - (p_{\mathrm{z},\ell^-} + p_{\mathrm{z},\overline{\nu}})^2. \qquad (9.5) \end{aligned}$$

Finally, it is assumed that the masses of the top and the antitop quark are the same:

$$m_t = m_{\overline{t}}. \tag{9.6}$$

The equalisation of the masses further eliminates a variable from the system of kinematic equations.

However, even after imposing these five boundary conditions the system of equations is still underconstrained. To find solutions, the system of equation is transformed. It is assumed that the $t\overline{t}$ system is balanced in the transverse plane, i.e. possible initial transverse momenta of the interacting partons are neglected as well as initial state radiation. Further, the approximations

$$m^2_\mu \ll m^2_b \tag{9.7}$$

and

$$m^2_b \ll m^2_t \tag{9.8}$$

are used. With these assumptions, the system of equations can be transformed into a single equation, which is a fourth order polynomial in one of the neutrino momentum components and can be written as

$$0 = \sum_{i=0}^{4} c_i(m_t, p_{\ell^+}, p_{\ell^-}, p_b, p_{\overline{b}})\, p_{\mathrm{x}}(\overline{\nu})^i \tag{9.9}$$

where, without loss of generality, $p_{\mathrm{x}}(\overline{\nu})$ has been chosen as the variable. The coefficients of this equation depend on the four-momenta of the observable particles and the top mass. Therefore, for a given value of the top mass parameter the equation can be solved analytically with a fourfold ambiguity.

In order to solve this equation, the top mass parameter is varied in steps of 1 GeV between 100 GeV and 300 GeV. For each value of the parameter it is checked if the equation has a real solution. This is done for both combinations of the two leading muons and two leading jets. For a single event and even for a single lepton–jet combination many solutions can exist.

9.1.2 Weighting of Solutions

The kinematic solutions that are found by the method are subsequently weighted by comparing the calculated neutrino energies to a reference model spectrum. For this reference spectrum 10 000 dileptonic $t\bar{t}$ events have been generated with PYTHIA. The same phase space cuts on p_{T} and η of the leptons and jets and on $\not{E}_{\mathrm{T}}$ that are also used in the event selection of reconstructed events are also applied on the generated events. The spectrum of the neutrino energies of the remaining events is subsequently fitted with a two-dimensional Landau distribution using an unbinned maximum likelihood fit. The reference spectrum is displayed in Figure 9.1.

Of all solutions in the event, the one with the highest weight, i.e., the highest probability of the neutrino energies, is chosen and the corresponding value of the top mass parameter is taken as the top mass discriminator value of the event.

9.2 Performance

The reference neutrino energy spectrum is generated assuming a fixed top mass of 172.5 GeV. Because this assumption about the top mass is used as input for the mass reconstruction, the result of this method might be biased. Nevertheless in [116] a linear dependency between true top mass and reconstructed mass is observed on generator level. However, for an independent mass measurement there are several different methods with no prior assumption about the mass. For the purpose of validating the topology of the selected events and reducing the background, this drawback does not matter since the mass can be assumed as already known.

In Figure 9.2, the correlation between the x momentum component of the antineutrino in generated and reconstructed signal events is shown. Although the reconstructed momenta are smeared with respect to the true values, a linear interdependency can be observed.

The efficiencies for finding at least one kinematic solution per event are shown for different samples in Table 9.1. The efficiency is highest for all samples containing missing transverse energy from neutrinos. For signal events the efficiency is 0.76 with no difference between events where the W bosons decay directly into muons and events where the decays are via a τ lepton. For the most important background, $Z/\gamma^{\star} \rightarrow \mu^{+}\mu^{-}$, the efficiency is significantly lower.

Hence, the requirement of the kinematic mass reconstruction as event selection criterion can be used to improve the signal over background ratio. The estimated number of signal events N_{sig} is the difference between the number of observed events N_{obs} and the expected background N_{bg}. It turns out that the ratio $N_{\mathrm{sig}}/N_{\mathrm{bg}}$ increases from 1.68 to 2.48 in comparison to the default selection if also a valid mass reconstruction is required. However, the significance,

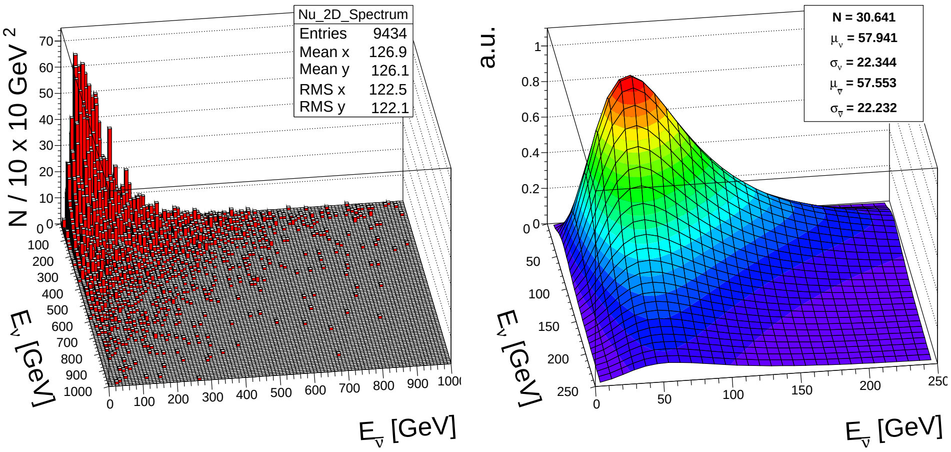

(a) generated energies (b) two-dimensional fit

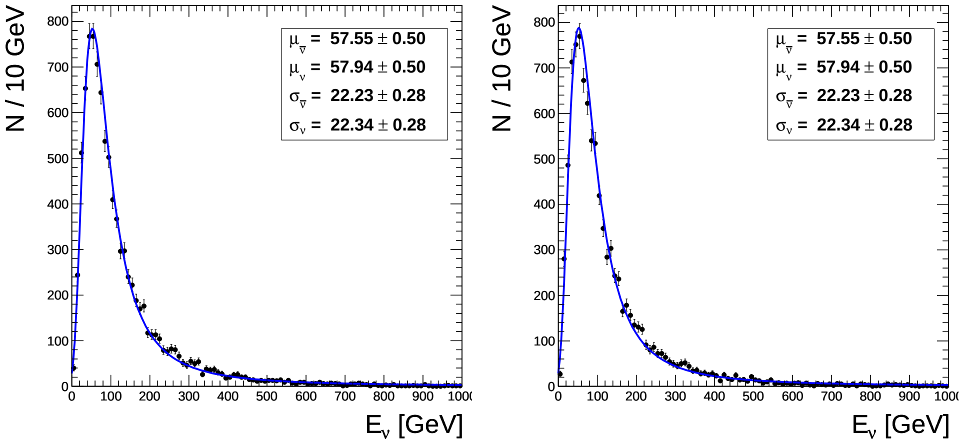

(c) fit of E_ν (d) fit of $E_{\overline{\nu}}$

Figure 9.1: Model neutrino energy spectrum generated with PYTHIA. The values for the localisation parameters μ_ν and $\mu_{\overline{\nu}}$, the width of the distribution σ_ν and $\sigma_{\overline{\nu}}$, and the normalisation factor N are given in the figures.

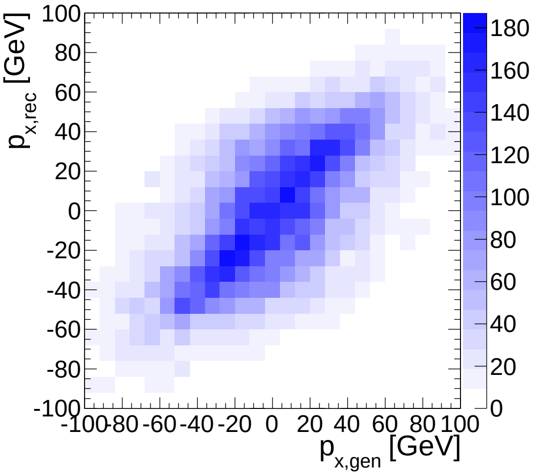

Figure 9.2: Generated vs. reconstructed $p_{x,\overline{\nu}}$ for simulated events $t\overline{t} \rightarrow b\overline{b}\ \mu^+\mu^-\nu\overline{\nu}$. A clear correlation between generated and reconstructed momentum can be seen.

sample	contr. before	efficiency	contr. after
data	28	0.68 ± 0.09	19
signal	19.8	0.76 ± 0.01	15.1
DY$\rightarrow \mu\mu$	8.9	0.49 ± 0.06	4.3
DY$\rightarrow \tau\tau$	0.6	0.76 ± 0.13	0.5
tW	0.7	0.69 ± 0.02	0.5
diboson	0.3	0.69 ± 0.04	0.2

Table 9.1: Efficiencies for Event Reconstruction in different samples

defined by $N_{\text{sig}}/\sqrt{N_{\text{sig}} + N_{\text{bg}}}$, decreases from 3.32 to 3.11 with the effect that the relative statistical error increases. Because the Drell–Yan background is reduced by a factor of two, also the systematic of this background is reduced drastically. It has to be studied if other systematics do increase instead if the kinematic mass reconstruction is used.

9.3 Results

Although the statistical error is larger if only mass-reconstructed events are used for the cross section calculation, the systematic uncertainty goes down because the Drell–Yan background is suppressed by a factor of two. The reconstructed top mass distribution is shown in Figure 9.3. The agreement between data and simulation looks quite good, especially the fraction of non-solvable events is the same. Also, both distributions have their maximum close to the nominal top mass.

An overview of the systematics is shown in Table 9.2. Surprisingly, the efficiency of the mass reconstruction algorithm does not depend strongly on the mass of the top. Instead, a strong dependence on the amount of initial and final state radiation Q^2 scale can be observed.

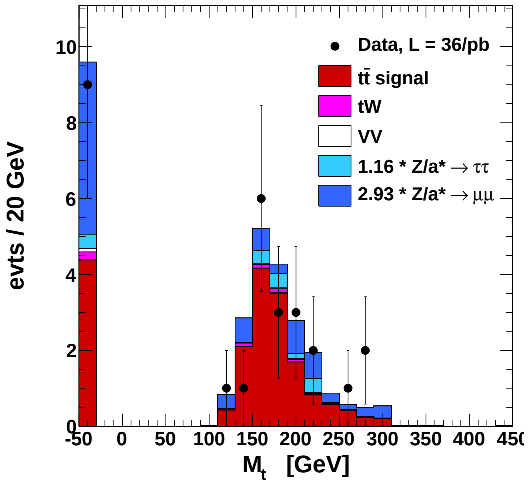

Figure 9.3: Reconstructed Top Mass. The left very left bin contains the events for which no kinematic solution is found.

source	**value** [%]	**value** [pb]
statistics	±32.2	±48.2
background	$+17.7/-18.1$	$+26.6/-27.1$
JES	$+5.9/-4.7$	$+8.9/-7.1$
$\not\!\!E_{\mathrm{T}}$ from PU	±1.1	±1.7
trigger	±0.7	±1.1
muons	±4.2	±6.2
mass	±2.5	±3.8
Q^2 scale	±7.0	±10.5
ISR/FSR	±11.0	±16.5
ME/PS thresh.	±3.0	±4.5
$b_{t\bar{t}\to\mu\mu X}$	±1.5	±2.3
luminosity	±4.0	±6.0

Table 9.2: Overview of all uncertainties after selection of two isolated muons, two jets and $\not\!\!E_{\mathrm{T}}$ and subsequently applied kinematic mass reconstruction.

The cross section using only reconstructed events is found to be

$$\sigma_{t\bar{t}}^{\mathrm{kin}} = 150 \pm 48\ (\mathrm{stat.}) \pm 35\ (\mathrm{syst.}) \pm 6\ (\mathrm{lumi.})\,\mathrm{pb} \tag{9.10}$$

which is in remarkably good agreement with the first result from Formula 8.3. The total relative uncertainty of the value is 40%.

The mass reconstruction method can thus be used as a complement to b tagging since it also reduces the background contribution but has a different systematic uncertainty.

Chapter 10

b Tagging Studies

10.1 b Tagging at CMS

Most methods to distinguish *b* jets from lighter jet flavours make use of the relatively long lifetime of the *b* quark. The mean lifetime of mesons containing *b* quarks lies typically between one and two picoseconds. This corresponds to a decay length of about half a millimetre times the relativistic γ of the meson. So the particles can travel a macroscopic distance before they decay, which can be resolved by tracking detectors. Two different algorithms based on the *b* decay length are examined in the following. The efficiencies and correction factors are taken from [117]. The values given there are based on the first $3\,\mathrm{pb}^{-1}$ of 7 TeV collision data recorded by the CMS detector. The efficiencies for *b* jets are obtained from jets which contain a muon with a high relative p_T with respect to the jet axis and are therefore clearly recognisable as *b* jets. The mistagging rates are estimated from the number of tracks with negative impact parameters inside the jet, respectively from jets with negative reconstructed decay lengths.

Track Counting Algorithm The track counting approach uses the significance of the impact parameters of the tracks that are associated to the jets. All tracks are ordered by the significance by which their impact parameters deviate from the primary vertex. The high efficiency version of the track counting algorithm (TCHE) uses the impact parameter significance of the second track as discriminator. For the high purity version (TCHP), the third track is used.

Several working points are defined for the TCHE algorithm. For this study, the loose working point is used requiring a discriminator value of at least 1.7 to identify a jet as a *b* jet. This means that the jet must have at least two tracks with an impact parameter significance of at least 1.7 (TCHEL). The identification efficiency for *b* jets in simulated events is given with 0.494 ± 0.003, however, the efficiency in data is lower. A correction factor of 0.88 ± 0.19 has to be applied per jet.

The probability to misidentify a jet from a gluon or a lighter quark flavour as a b jet is given by 0.062 ± 0.002 in the data. The correction factor between data and simulation is obtained to be 0.91 ± 0.03.

Simple Secondary Vertex Algorithm Another method to use the long lifetime for b jet identification is to try to reconstruct a secondary vertex from which the tracks of the jet originate. Like for the track counting algorithm, there are a high efficiency and a high purity version of the simple secondary vertex algorithm. The high efficiency version (SSVHE) requires that at least two tracks are associated to the secondary vertex, the high purity version (SSVHP) requires three tracks. The discriminator value for both algorithms is a monotonous function of the three-dimensional distance between the secondary and the primary vertex.

Here, the SSVHE algorithm is used with the medium working point at 1.74 (SSVHEM). The efficiency in the simulation for this working point is given by 0.417 ± 0.003 in [117] with a scale factor of 0.97 ± 0.19 to data. The mistagging rate is given by 0.0087 ± 0.0006 in the data with a scale factor of 0.87 ± 0.08 between data and simulation.

10.2 Results

At least one b-tagged jet is now required for the event selection in addition to the default selection described in Chapter 6. This gives a higher selection efficiency and a smaller systematic uncertainty than the requirement of two b-tagged jets would do. The correction factors from the previous section are used for the efficiencies of the two algorithms. The correction factors for mistagging are neglected since the background is small anyway.

In the histograms in Figure 10.1, the distributions for both b tagging discriminators are shown as well as the number of b-tagged jets per event. It can be seen that for both algorithms there are more b-tagged jets in data than expected from the simulation. Taking into account the given scale factors of 0.88 ± 0.19 and 0.97 ± 0.19 for the TCHEL and SSVHEM, the deviation between data and simulation becomes even worse. This disagreement can be due to statistical fluctuations. However, it also cannot be excluded that the correction factors, which are based on only a small fraction of the statistics, are not valid for the whole run range or that the systematic uncertainties are underestimated.

Calculating the cross section with the two algorithms, one obtains

$$\sigma_{t\bar{t}}^{\mathrm{TCHEL}} = 196 \pm 48\ (\mathrm{stat.}) \pm 33\ (\mathrm{syst.}) \pm 8\ (\mathrm{lumi.})\,\mathrm{pb} \tag{10.1}$$

with the TCHEL and

$$\sigma_{t\bar{t}}^{\mathrm{SSVHEM}} = 181 \pm 47\ (\mathrm{stat.}) \pm 32\ (\mathrm{syst.}) \pm 7\ (\mathrm{lumi.})\,\mathrm{pb} \tag{10.2}$$

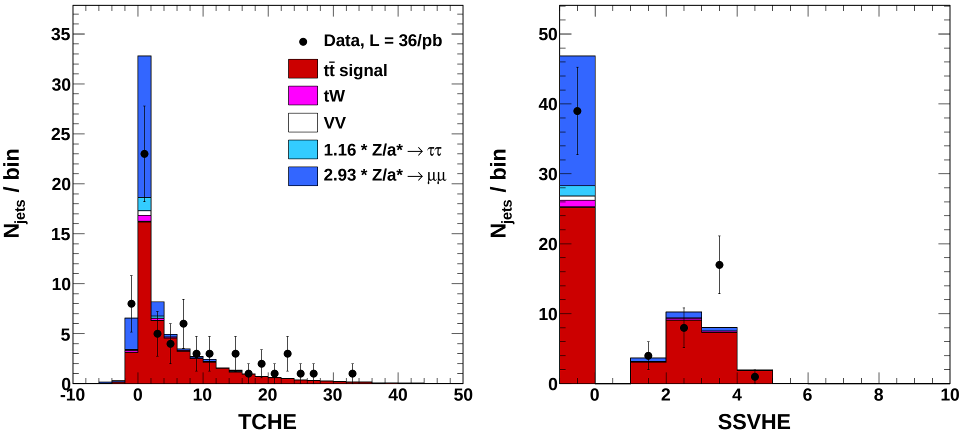

(a) TCHE discriminator

(b) SSVHE discriminator

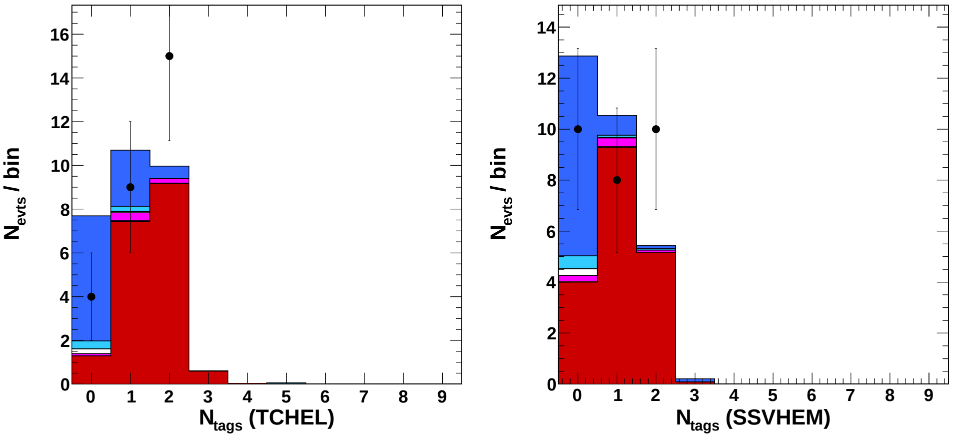

(c) multiplicity of jets with an TCHE discriminator > 1.7

(d) multiplicity of jets with an SSVHE discriminator > 1.74

Figure 10.1: b tagging distributions after default event selection of two isolated muons, two jets, and $\not\!\!E_{\mathrm{T}}$.
The upper plots show the b tagging discriminators for both algorithms, the lower ones the number of b tagged jets per event. The negative first bin in (b) contains the events with no reconstructed secondary vertex.

source	**value** [%]	**value** [pb]
statistics	± 24.4	± 47.7
background	$+8.2/-8.6$	$+16.0/-16.8$
JES	$+4.4/-5.2$	$+8.6/-10.2$
b tagging	± 12.0	± 23.5
$\not\!\!E_{\mathrm{T}}$ from PU	± 1.1	± 2.2
trigger	± 0.7	± 1.4
muons	± 4.2	± 8.1
mass	± 2.5	± 4.9
Q^2 scale	± 2.0	± 3.9
ISR/FSR	± 3.0	± 5.9
ME/PS thresh.	± 2.0	± 3.9
$b_{t\bar{t}\to\mu\mu X}$	± 1.5	± 2.9
luminosity	± 4.0	± 7.8

Table 10.1: Overview of uncertainties after selection using TCHEL.

source	**value** [%]	**value** [pb]
statistics	± 25.8	± 46.6
background	$+3.5/-4.5$	$+6.3/-8.1$
JES	$+5.0/-4.2$	$+9.0/-7.6$
b tagging	± 15.0	± 27.1
$\not\!\!E_{\mathrm{T}}$ from PU	± 1.1	± 2.0
trigger	± 0.7	± 1.3
muons	± 4.2	± 7.5
mass	± 2.5	± 4.5
Q^2 scale	± 2.0	± 3.6
ISR/FSR	± 3.0	± 5.4
ME/PS thresh.	± 2.0	± 3.6
$b_{t\bar{t}\to\mu\mu X}$	± 1.5	± 2.7
luminosity	± 4.0	± 7.2

Table 10.2: Overview of uncertainties after selection using SSVHEM.

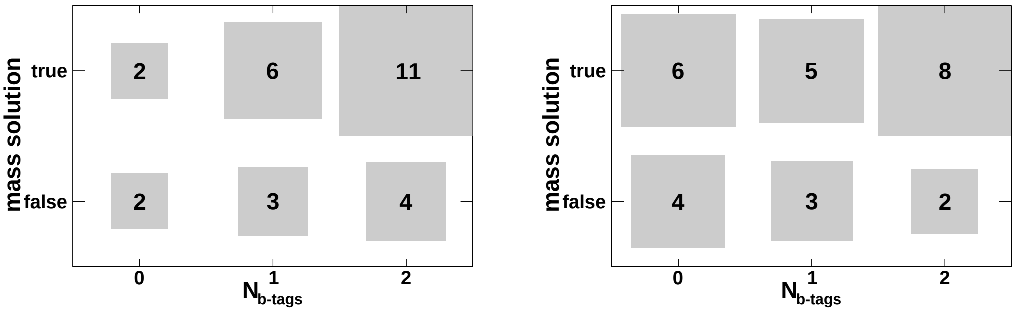

(a) TCHE discriminator

(b) SSVHE discriminator

Figure 10.2: Correlation between b tagging and mass reconstruction. On the horizontal axis the number of b-tagged jets is displayed. The vertical axis has two bins for events with and without kinematic event solution, respectively.

using the SSVHEM. The uncertainties are listed in detail in Table 10.1 and Table 10.2. Both results are larger than the cross sections determined with the default selection and after the mass reconstruction. Especially, the difference between $\sigma_{t\bar{t}}^{\mathrm{TCHEL}}$ and $\sigma_{t\bar{t}}^{\mathrm{def}}$ is two times larger than the given b tagging uncertainty.

For the $t\bar{t}$ cross section result the first two obtained values determined with the default selection and with the mass reconstruction algorithm are considered as more reliable as those obtained with b tagging. It will be interesting to see if the agreement between data and simulation in the plots of Figure 10.1 gets better with more statistics in the future.

Finally, the correlation between the number of b-tagged jets and the kinematic event solution is studied. This is illustrated in Figure 10.2. A kinematic solution exists for 19 out of the 28 candidate events. Based on the numbers from the previous chapter, it is expected that about 10 events are background. Further, it can be expected that among the 19 successfully reconstructed events there are still about 5 background events while among the 9 events with no solution there about 5 signal events.

Taking this into account, both plots look quite reasonable. The fraction of events with a kinematic solution is higher for events with b-tagged jets than for events without solution. For the TCHEL (SSVHEM) algorithm the kinematic reconstruction efficiency is 50% (60%) for events without b tags while it is 70% (72%) for events with at least one tagged jet. For events with two b tags these efficiencies increase to 73% for the TCHEL and 80% for the SSVHEM.

Chapter 11

Summary

The cross section for top–antitop production has been measured using a selection of two oppositely-charged muons, two jets and missing transverse energy. The contribution of the most important background process, $Z/\gamma^\star \to \mu^+\mu^-$, has been scaled to the data using the Z^0 mass peak. The contribution of events from QCD background and events with fake muons has been constrained to an upper limit by selecting events with equally charged muons.

On top of the selection of physics objects, further attempts have been studied in order to improve the measurement. The result using the kinematic event solution algorithm gives a result which is in excellent agreement with the value obtained after the default selection. The deviation between the two values is only about 1% although they have partially different systematic uncertainties.

Two different b tagging algorithms have been studied, one using the impact parameters of tracks associated to the jets, the other one based on secondary vertex reconstruction. For the event selection at least on b-tagged jet has been required. For both algorithms the control distributions show deviations between data and simulation. Taking into account the provided correction factors for both algorithms would make these discrepancies even worse. The cross sections with b tagging are therefore assumed to be not as reliable as the other values. Nevertheless, a correlation between the candidate events selected with the mass reconstruction method and those selected with b tagging can be observed.

Since the value $\sigma_{t\bar{t}}^{\text{kin}}$ using the the mass reconstruction has a smaller total uncertainty than the one measured after the default selection, $\sigma_{t\bar{t}}^{\text{kin}}$ is considered as the best value for the cross section. Hence, the final result of this analysis for the $t\bar{t}$ production cross section is given by

$$\sigma_{t\bar{t}} = 150 \pm 48\ (\text{stat.}) \pm 35\ (\text{syst.}) \pm 6\ (\text{lumi.})\,\text{pb}. \tag{11.1}$$

This result can be compared to theoretical standard model predictions. This is done in Figure 11.1. Two calculated values using different PDFs as input and their uncertainties are shown. The value using the MSTW08 PDFs

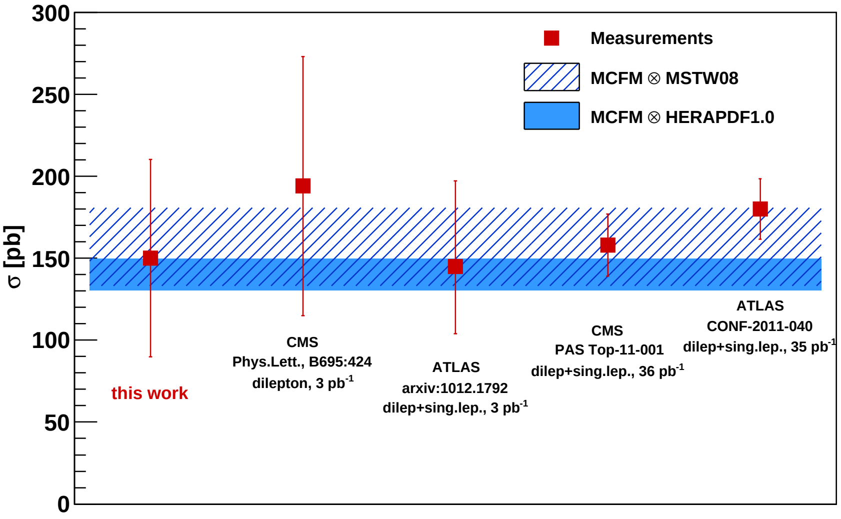

Figure 11.1: Comparison between measured cross sections and NLO predictions. The markers show measured cross section results and their uncertainties. These are compared to two different theoretical predictions illustrated by the coloured and the dashed area.

[43] is $157.5^{+23.2}_{-24.4}$ pb [118], the one with HERAPDF1.0 [119] is $144.3^{+5.5}_{-13.8}$ pb [120]. The measured value is in agreement with both NLO calculations. No deviation from the standard model can be observed.

Further, the result is compared to other measured values published by the LHC experiments. The first result concerning top quark pair production was published by the CMS collaboration in October 2010 [5]. It is based on the first 3 pb^{-1} of data and combines results from the dimuon, dielectron and electron–muon decay channel. The measured cross section is found to be 194 ± 72 (stat.) ± 24 (syst.) ± 21 (lumi.) pb with a very large statistical error. Another publication was released by the ATLAS collaboration in December 2010 [6]. It comprises results from the single lepton and dilepton channel using the first 2.9 pb^{-1} of data. The result is 145 ± 31 (stat.)$^{+42}_{-27}$ (syst.) pb.

More recent results including the whole 2010 data have just been published by both collaboration and are also shown in Figure 11.1. The CMS value of 158 ± 10 (stat.)± 15 (syst.)± 6 (lumi.) pb is combined from the dilepton channel and single lepton channel with and without b tagging [121]. The ATLAS result of 180 ± 9 (stat.) ± 15 (syst.) ± 6 (lumi.) pb is combined from the same decay channels in a similar way [122].

In conclusion, it can be said that for an experimental result with very first collision data almost all distributions and all comparisons between data and Monte Carlo simulation look remarkably consistent. The detector was very well understood from the very beginning of data taking thanks to extensive studies with cosmic radiation.

Up to now, the uncertainty of the result is dominated by the statistical uncertainty. With more data, which will be recorded in 2011, systematic uncertainties will soon become more important. Especially the dependency of the Drell–Yan dimuon mass shape on the selection jets and $\not{E}_{\mathrm{T}}$ has to be understood since this is by far the largest systematic uncertainty. In order to do this, further studies with more data have to be accomplished in 2011. Also more detailed studies like measurements of differential cross sections will be possible with more data.

List of Tables

List of Figures

Bibliography

[1] M. Kobayashi and T. Maskawa. *cp*-violation in the renormalizable theory of weak interaction. *Prog.Theor.Phys.*, 49(2):652–657, 1973. `http://ptp.ipap.jp/link?PTP/49/652`.

[2] S. W. Herb, D. C. Hom, and L. M. Lederman et al. Observation of a dimuon resonance at 9.5 gev in 400-gev proton-nucleus collisions. *Phys.Rev.Lett.*, 39(5):252–255, 1977. `http://prl.aps.org/abstract/PRL/v39/i5/p252_1`.

[3] CDF Collaboration: F. Abe et al. Observation of Top Quark Production in $p\bar{p}$ Collisions with the Collider Detector at Fermilab. *Phys.Rev.Lett.*, 74(14):2626–2631, 1995. `http://arxiv.org/abs/hep-ex/9503002`.
D0 Collaboration: S. Abachi et al. Observation of the Top Quark. *Phys.Rev.Lett.*, 74(14):2632–2637, 1995. `http://arxiv.org/abs/hep-ex/9503003`.

[4] *LHC sets new world record*, volume PR18.09 of *CERN Press Release*, 2009. `http://press.web.cern.ch/press/PressReleases/Releases2009/PR18.09E.html`.

[5] The CMS collaboration: V. Khachatryan et al. First Measurement of the Cross Section for Top-Quark Pair Production in Proton-Proton Collisions at $\sqrt{s} = 7$ TeV. *Phys. Lett.*, B695:424–443, 2011. `http://arxiv.org/abs/1010.5994`.

[6] ATLAS Collaboration: G. Aad et al. Measurement of the top quark-pair production cross section with ATLAS in pp collisions at $\sqrt{s} = 7\,\mathrm{TeV}$, 2010. `http://arxiv.org/abs/1012.1792`.

[7] M. Aldaya, W. Behrenhoff, D. Dammann, E. Gallo, A. Geiser, J. Hauk, M. Marienfeld, A.B. Meyer. Measurement of the Top Quark Pair Production Cross Section in the Dimuon Decay Channel at $\sqrt{s} = 7$ TeV. *analysis note*, AN-10-428, 2010. unpublished, restricted access at `http://cms.cern.ch/iCMS/jsp/openfile.jsp?tp=draft&files=AN2010_428_v9.pdf`.

[8] CMS Collaboration. Measurement of the top-quark pair-production cross section in the dilepton channel at $\sqrt{s} = 7$ TeV , 2011. to be published, for approved results, see `https://twiki.cern.ch/twiki/bin/view/CMSPublic/PhysicsResultsTOP10005`.

[9] D. Perkins. *Introduction to High Energy Physics*. Cambridge University Press, 4th edition, 2000. ISBN 0 521 62196 8.

[10] K. Nakamura et al. PDG Particle Listings. *J.Phys.*, G37:075021, 2010. `http://pdg.lbl.gov/2010/listings/contents_listings.html`.

[11] M. Weitz, A. Huber, F. Schmidt-Kaler, D. Leibfried, and T. W. Hänsch. Precision measurement of the hydrogen and deuterium 1 S ground state Lamb shift. *Phys.Rev.Lett.*, 72(3):328–331, 1994. `http://prl.aps.org/abstract/PRL/v72/i3/p328_1`.

[12] D. Berkeland, E. Hinds, and M. Boshier. Precise Optical Measurement of Lamb Shifts in Atomic Hydrogen. *Phys.Rev.Lett.*, 75(13):2470–2473, 1995. `http://prl.aps.org/abstract/PRL/v75/i13/p2470_1`.

[13] H. J. Bhabha. The Scattering of Positrons by Electrons with Exchange on Dirac's Theory of the Positron. *Proc.R.Soc.*, A154:195–206, 1936. `http://rspa.royalsocietypublishing.org/content/154/881/195`.

[14] H1 Collaboration and ZEUS Collaboration. Resonance searches at HERA, 2009. `http://arxiv.org/abs/0907.4574`.

[15] C. S. Wu, E. Ambler, R. W. Hayward, D. D. Hoppes, and R. P. Hudson. Experimental Test of Parity Conservation in Beta Decay. *Phys.Rev.*, 105(4):1413–1415, 1957. `http://prola.aps.org/abstract/PR/v105/i4/p1413_1`.

[16] Gargamelle Collaboration: F. J. Hasert et al. Observation of neutrino-like interactions without muon or electron in the gargamelle neutrino experiment. *Phys.Lett.*, B46(1):138–140, 1973. `http://cdsweb.cern.ch/record/203096`.

[17] UA1 Collaboration: G. Arnison et al. Experimental observation of isolated large transverse energy electrons with associated missing energy at s**(1/2) = 540-GeV. *Phys.Lett.*, B122:103–116, 1983. `http://cdsweb.cern.ch/record/142059/`.

[18] UA1 Collaboration: G. Arnison et al. Experimental observation of lepton pairs of invariant mass around 95-GeV/c**2 at the CERN SPS collider. *Phys.Lett.*, B126:398–410, 1983. `http://ccdb4fs.kek.jp/cgi-bin/img_index?8306331`.

[19] UA2 Collaboration: M. Banner et al. Observation of single isolated electrons of high transverse momentum in events with missing transverse energy at the CERN anti-p p collider. *Phys.Lett.*, B122:476–485, 1983. `http://cdsweb.cern.ch/record/142759`.

[20] ALEPH, DELPHI, L3, OPAL, SLD Collaborations, the LEP Electroweak Working Group, the SLD Electroweak and Heavy Flavour Groups. Precision Electroweak Measurements on the Z Resonance. *Phys.Rept.*, 427:257, 2006. `http://arxiv.org/abs/hep-ex/0509008`.

[21] ALEPH Collaboration, CDF Collaboration, D0 Collaboration, DELPHI Collaboration, L3 Collaboration, OPAL Collaboration, SLD Collaboration, LEP Electroweak Working Group, Tevatron Electroweak Working Group, and SLD electroweak heavy flavour groups. Precision Electroweak Measurements and Constraints on the Standard Model, 2009. `http://arxiv.org/abs/0911.2604`.

[22] M. Kobayashi and T. Maskawa. CP Violation in the Renormalizable Theory of Weak Interaction. *Prog.Theor.Phys.*, 49:652–657, 1973. `http://ptp.ipap.jp/link?PTP/49/652/`.

[23] M. Okamoto. Full determination of the CKM matrix using recent results from lattice QCD. *POS*, LAT2005:013, 2005. `http://arxiv.org/abs/hep-lat/0510113`.

[24] CDF Collaboration: D. Acosta et al. Measurement of $B(t \rightarrow Wb)/B(t \rightarrow Wq)$ at the Collider Detector at Fermilab. *Phys.Rev.Lett.*, 95:102002, 2005. `http://arxiv.org/abs/hep-ex/0505091`.

[25] D0 Collaboration: V. M. Abazov et al. Measurement of $B(t \rightarrow Wb)/B(t \rightarrow Wq)$ at $\sqrt(s) = 1.96TeV$. *Phys.Lett.*, B639:616, 2006. `http://arxiv.org/abs/hep-ex/0603002`.

[26] J. W. F. Valle. Neutrino physics overview, 2006. `http://arxiv.org/abs/hep-ph/0608101v1`.

[27] M. Nakagawa Z. Maki and S. Sakata. Remarks on the Unified Model of Elementary Particles. *Prog.Theor.Phys.*, 28(5):870–880, 1962. `http://ptp.ipap.jp/link?PTP/28/870/`.

[28] NuTeV Collaboration: G. P. Zeller et al. A Measurement of the Weak Mixing Angle in Neutrino-Nucleon Scattering at NuTeV, 1999. `http://arxiv.org/abs/hep-ex/9906024`.

[29] SLAC E158: P. L.Anthony et al. Precision measurement of the weak mixing angle in Moeller scattering. *Phys.Rev.Lett.*, 95:081601, 2005. `http://arxiv.org/pdf/hep-ex/0504049`.

[30] S. L. Glashow. Partial-symmetries of weak interactions. *Nucl.Phys.*, 22(4):579–588, 1961. `www.slac.stanford.edu/spires/find/hep/www?j=NUPHA,22,579`.
A. Salam. Renormalizability of Gauge Theories. *Phys.Rev.*, 127(1):331–334, 1962. `http://prola.aps.org/abstract/PR/v127/i1/p331_1`.
S. Weinberg. A Model of Leptons. *Phys.Rev.Lett.*, 19(21):1264–1266, 1967. `http://prl.aps.org/abstract/PRL/v19/i21/p1264_1`.

[31] P. Higgs. Spontaneous Symmetry Breakdown without Massless Bosons. *Phys.Rev.*, 145(4):1156–1163, 1966. `http://prola.aps.org/abstract/PR/v145/i4/p1156_1`.

[32] ALEPH, DELPHI, L3, OPAL and SLD Collaboration: Abbiendi et al. Search for the Standard Model Higgs Boson at LEP. *Phys.Lett.*, B565: 61, 2003. `http://arxiv.org/abs/hepex/0306033`.

[33] D0 Collaboration CDF collaboration, the Tevatron New Physics, and Higgs Working group. Combined CDF and D0 Upper Limits on Standard Model Higgs-Boson Production with 2.1 - 5.4 fb-1 of Data, 2009. `http://arXiv.org/abs/0911.3930`.

[34] LEP Electroweak Working Group. LEP/TEV EW WG Website, July 2010. `http://lepewwg.web.cern.ch/LEPEWWG`.

[35] B. W. Lee, C. Quigg, and H. B. Thacker. Weak interactions at very high energies: The role of the Higgs-boson mass. *Phys.Rev.*, D16(5): 1519–1531, 1977. `http://prd.aps.org/abstract/PRD/v16/i5/p1519_1`.

[36] J. Einasto. Dark Matter, 2009. `http://arxiv.org/abs/0901.0632`.

[37] Ian J R Aitchison. Supersymmetry and the MSSM: An Elementary Introduction, 2005. `http://arxiv.org/abs/hep-ph/0505105`.

[38] N. Arkani-Hamed, S. Dimopoulos, and G. Dvali. The hierarchy problem and new dimensions at a millimeter. *Phys.Lett.*, B429(3–4):263–272, 1998. `http://arxiv.org/abs/hep-ph/9803315`.

[39] D. Kapner, T. Cook, E. Adelberger, J. Gundlach, B. Heckel, C. Hoyle, and H. Swanson. Tests of the Gravitational Inverse-Square Law below the Dark-Energy Length Scale. *Phys.Rev.Lett.*, 98:021101, 2007. `http://arxiv.org/abs/hep-ph/0611184`.

[40] R. S. Chivukula. Electroweak symmetry breaking. *J.Phys.: Conf.Ser.*, 37:28–33, 2006. `http://www.iop.org/EJ/abstract/1742-6596/37/1/007`.

[41] J. W. Hustonand W. J. Stirling J. M. Campbell. Hard Interactions of Quarks and Gluons: A Primer for LHC Physics. *Rept.Prog.Phys.*, 70:89, 2007. `http://arxiv.org/abs/hep-ph/0611148v1`.

[42] V. N. Gribov and L. N. Lipatov. Deep inelastic e p scattering in perturbation theory. *Sov.J.Nucl.Phys.*, 15:438–450, 1972.
L. N. Lipatov. The parton model and perturbation theory. *Sov.J.Nucl.-Phys.*, 20:94–102, 1975.
Y. L. Dokshitzer. Calculation of the Structure Functions for Deep Inelastic Scattering and e+ e- Annihilation by Perturbation Theory in Quantum Chromodynamics. *Sov.Phys.JETP*, 46:641–653, 1977.
G. Altarelli and G. Parisi. Asymptotic freedom in parton language. *Nucl.Phys.*, B(2):298–318, 1977. `http://adsabs.harvard.edu/abs/1977NuPhB.126..298A`.

[43] A. D. Martin, W. J. Stirling, R. S. Thorne, and G. Watt. Parton distributions for the LHC. *EPJ*, C63:189, 2009. `http://arxiv.org/abs/0901.0002`.

[44] The H1 and ZEUS collaborations. Combined Measurement and QCD Analysis of the Inclusive ep Scattering Cross Sections at HERA, 2009. `http://arxiv.org/abs/0911.0884v2`.

[45] New Muon Collaboration: M. Arneodo et al. Measurement of the proton and deuteron structure functions, F2(p) and F2(d), and of the ratio sigma(L)/sigma(T). *Nucl.Phys.*, B483:3–43, 1997. `http://arxiv.org/abs/hep-ph/9610231`.

[46] NuTeV Experiment: M. Tzanov et al. Precise Measurement of Neutrino and Anti-neutrino Differential Cross Sections. *Phys.Rev.*, D74:012008, 2005. `http://arxiv.org/abs/hep-ex/0509010`.

[47] S. D. Drell and T. Yan. Massive Lepton-Pair Production in Hadron-Hadron Collisions at High Energies. *Phys.Rev.Lett.*, 25(5):316–320, 1970. `http://prl.aps.org/abstract/PRL/v25/i5/p316_1`.

[48] P. Bartalini. The underlying event at the LHC. *CMS Note*, 2006/067, 2006. `http://cdsweb.cern.ch/record/973110/`.

[49] A. de Roeck. The ATLAS and CMS experiments at the LHC. *Act.Phys.Pol.*, B39:2455, 2008. `http://th-www.if.uj.edu.pl/acta/vol39/pdf/v39p2455.pdf`.

[50] B. R. Webber R. K. Ellis, W. J. Stirling. *QCD and Collider Physics.* Cambridge Monographs on Particle Physics, Nuclear Physics and Cosmology, 1st edition, 1996. ISBN 0 521 54589 7.

[51] N. Kidonakis. Higher-order corrections to top-antitop pair and single top quark production, 2009. `http://arxiv.org/abs/0909.0037v1`.

[52] D0 Collaboration: V. M. Abazov et al. Evidence for production of single top quarks and first direct measurement of $|V_{tb}|$. *Phys.Rev.Lett.*, 98:181802, 2007. `http://arxiv.org/abs/hep-ex/0612052`.
CDF Collaboration: T. Aaltonen et al. Measurement of the Single Top Quark Production Cross Section at CDF. *Phys. Rev. Lett.*, 101:252001, 2008. `http://arxiv.org/abs/0809.2581`.

[53] R. Schwienhorst and C. Yuan and C. Mueller and Q. Cao. Single top quark production and decay in the t channel at next-to-leading order at the lhc. *Phys. Rev. D*, 83(3):034019, Feb 2011. `http://prd.aps.org/abstract/PRD/v83/i3/e034019`.

[54] S. Catani. Aspects of QCD, from the Tevatron to the LHC. *CERN-Th*, 2000-073, 2000. `http://arxiv.org/abs/hep-ph/0005233`, personal modifications: $t\bar{t}$ cross section highlighted, 7 TeV line added.

[55] Kirill Melnikov and Timo van Ritbergen. The three-loop relation between the MS-bar and the pole quark masses. *Phys. Lett.*, B482:99–108, 2000. `http://arxiv.org/abs/hep-ph/9912391`.

[56] S. S. Willenbrock M. C. Smith. Top-quark pole mass. *Phys.Rev.Lett.*, 79:3825–3828, 1997. `http://arxiv.org/abs/hep-ph/9612329`.

[57] Werner Bernreuther. Top quark physics at the LHC. 2008. `http://arxiv.org/abs/0805.1333`.

[58] Zhenjun Xiao et al. Implications of the top quark mass measurement for the SM Higgs boson mass MH. *J.Phys.*, G21:19–28, 1995. `http://www.iop.org/EJ/abstract/0954-3899/21/1/003/`.

[59] G. Burgers et al. *Z Physics at LEP1*, volume 1: Standard Physics. CERN, 1989. `http://cdsweb.cern.ch/record/116932/`.

[60] M. Veltman. Limit on mass differences in the Weinberg model. *Nucl.Phys.*, B(123):89–99, 1977. `igitur-archive.library.uu.nl/phys/2005-0622-154904/13949.pdf`.

[61] S. Heinemeyer, W. Hollik, D. Stockinger, A. M. Weber, and G. Weiglein. Precise prediction for M(W) in the MSSM. *JHEP*, 08:052, 2006. `http://arxiv.org/abs/hep-ph/0604147`.

[62] L. G. Almeida., G. F.Sterman, and W. Vogelsang. Threshold Resummation for the Top Quark Charge Asymmetry. *Phys. Rev.*, D78:014008, 2008. `http://arxiv.org/abs/0805.1885`.

[63] CMS Collaboration. Measurement of the charge asymmetry in top quark pair production with the CMS experiment. *PAS*, TOP-10-001, 2010. `http://cdsweb.cern.ch/record/1335714/`.

[64] T. M. P. Tait and C.-P. Yuan. Single top quark production as a window to physics beyond the standard model. *Phys.Rev.*, D63(1):014018, 2000. `http://arxiv.org/abs/hep-ph/0007298`.

[65] CDF Collaboration: T. Aaltonen et al. Combination of CDF top quark pair production cross section measurement with up to 4.6 fb^{-1}. *CDF Note*, 9913, 2009. `http://www-cdf.fnal.gov/physics/new/top/confNotes/cdf9913_ttbarxs4invfb.pdf`.

[66] Tevatron Electroweak Working Group. Combination of CDF and D0 Measurements of the Single Top Production Cross Section. 2009. `http://arxiv.org/abs/0908.2171v1`.

[67] D0 Collaboration: V. M. Abazov et al. Evidence for production of single top quarks. *Phys. Rev.*, D78:012005, 2008. `http://arxiv.org/abs/0803.0739v2`.

[68] Tevatron Electroweak Working Group. Combination of CDF and D0 Results on the Mass of the Top Quark. 2010. `http://arxiv.org/abs/1007.3178`.

[69] A. Abulencia. Top Quark Mass Measurement from Dilepton Events at CDF II with the Matrix-Element Method. *Phys.Rev.*, D74:032009, 2006. `http://arxiv.org/abs/hep-ex/0605118`.

[70] CDF Collaboration: T. Aaltonen et al. Cross Section Constrained Top Quark Mass Measurement from Dilepton Events at the Tevatron. *Phys.Rev.Lett.*, 100:062005, 2008. `http://arxiv.org/abs/0710.4037`.

[71] C. S. Hill, J. R. Incandela, and J. M. Lamb. A method for measurement of the top quark mass using the mean decay length of b hadrons in ttbar events. *Phys.Rev.*, D71:054029, 2005. `http://arxiv.org/abs/hep-ex/0501043`.

[72] D0 Collaboration: V. M. Abazov et al. Experimental Discrimination between Charge $2e/3$ Top Quark and Charge $4e/3$ Exotic Quark Production Scenarios. *Phys.Rev.Lett.*, 98(4):041801, 2007. `http://arxiv.org/abs/hep-ex/0608044`.

[73] T. Aaltonen et al. Evidence for a Mass Dependent Forward-Backward Asymmetry in Top Quark Pair Production. 2011. `http://arxiv.org/abs/1101.0034`.

[74] CDF Collaboration: T. Aaltonen et al. Measurement of the fraction of $t\bar{t}$ production via gluon-gluon fusion in $p\bar{p}$ collisions at $\sqrt{s} = 1.96$-TeV. *Phys.Rev.Lett.*, D79:031101, 2008. `http://arxiv.org/abs/0807.4262v1`.

[75] D0 Collaboration: V. M. Abazov et al. Simultaneous measurement of the ratio B(t→Wb)/B(t→Wq) and the top quark pair production cross section with the D0 detector at sqrt(s)=1.96 TeV. *Phys.Rev.Lett.*, 100: 192003, 2008. `http://arxiv.org/abs/0801.1326`.

[76] Jean-Luc Caron (with modifications by Christoph Rosemann). Layout of the LEP tunnel including future LHC infrastructures, 1993. `http://cdsweb.cern.ch/record/841542/`.

[77] L. Evans and P. Bryant (editors). LHC Machine. *JINST*, 3(S08001), 2008. `http://www.iop.org/EJ/journal/-page=extra.lhc/jinst`.

[78] ALICE Collaboration: K. Aamodt et al. The ALICE experiment at the CERN LHC. *JINST*, 3(S08002), 2008. `http://www.iop.org/EJ/journal/-page=extra.lhc/jinst`.

[79] LHCb Collaboration: A. Augusto Alves jr et al. The LHCb Detector at the LHC. *JINST*, 3(S08005), 2008. `http://www.iop.org/EJ/journal/-page=extra.lhc/jinst`.

[80] ATLAS Collaboration: G. Aad et al. The ATLAS Experiment at the CERN Large Hadron Collider. *JINST*, 3(S08003), 2008. `http://www.iop.org/EJ/journal/-page=extra.lhc/jinst`.

[81] CMS Collaboration: S. Chatrchyan et al. The CMS experiment at the CERN LHC. *JINST*, 3(S08004), 2008. `http://www.iop.org/EJ/journal/-page=extra.lhc/jinst`.

[82] LHCf Collaboration: O. Adriani et al. The LHCf detector at the CERN Large Hadron Collider. *JINST*, 3(S08006), 2008. `http://www.iop.org/EJ/journal/-page=extra.lhc/jinst`.

[83] TOTEM Collaboration: G. Anelli et al. The TOTEM Experiment at the CERN Large Hadron Collider. *JINST*, 3(S08007), 2008. `http://www.iop.org/EJ/journal/-page=extra.lhc/jinst`.

[84] CMS Collaboration. Alignment of the CMS silicon tracker during commissioning with cosmic rays. *JINST*, 5:3009, 2010. `http://arxiv.org/abs/0910.2505`.

[85] CMS Collaboration: S. Chatrchyan et al. CMS Physics Technical Design Report, Volume II: Physics Performance. *J.Phys*, G34(6):995, 2007. `http://iopscience.iop.org/0954-3899/34/6/S01/`.

[86] F. Cossutti for the CMS collaboration. Tuning and optimization of the CMS simulation software. *J.Phys.Conf.Ser.*, 219:032005, 2010. `http://iopscience.iop.org/1742-6596/219/3/032005`.

[87] T. Sjöstrand, S. Mrenna, and P. Skands. Pythia 6.4 Physics and Manual, 2006. `http://arxiv.org/abs/hep-ph/0603175`.

[88] F. Maltoni and T. Stelzer. MadEvent: Automatic Event Generation with MadGraph. *JHEP*, 0302:027, 2003. `http://arxiv.org/abs/hep-ph/0208156`.

[89] Zbigniew Was. TAUOLA for simulation of tau decay and production: perspectives for precision low energy and LHC applications. *IFJPAN*, IV-2011-1, 2011. `http://arxiv.org/abs/1101.1652`.

[90] S. Agostinelli et al. G4–a simulation toolkit. *Nucl.Inst.Meth.*, A506 (3):250 – 303, 2003. `http://www.sciencedirect.com/science/article/B6TJM-48TJFY8-5/2/23ea98096ce11c1be446850c04cfa498`.

[91] M. Case and M. Liendl and F. van Lingen. Detector Description Domain Architecture & Data Model. *CMS-Note*, 2001/057, 2001. `http://cdsweb.cern.ch/record/687388/`.

[92] CMS HLT Group. Muon HLT. website, last visit May 11, 2011. `https://twiki.cern.ch/twiki/bin/view/CMSPublic/SWGuideMuonHLT`.

[93] CMS Collaboration. Measurement of CMS Luminosity. *PAS*, EWK-10-004, 2010. `http://cdsweb.cern.ch/record/1279145/`.

[94] S. van der Meer. Calibration of the effective Beam Height in the ISR. *CERN-ISR-PO*, (68-31), 1968. `http://cdsweb.cern.ch/record/296752/`.

[95] A. Zuranski. Preliminary luminosity error and normalization, March 2011. Presentation in the CMS general meeting, restricted access at `http://indico.cern.ch/getFile.py/access?contribId=0&resId=0&materialId=slides&confId=123703`.

[96] Luminosity Overview. restricted website: `http://cms-service-lumi.web.cern.ch/cms-service-lumi/overview.php`.

[97] H. Bethe. Zur Theorie des Durchgangs schneller Korpuskularstrahlen durch Materie. *Annalen der Physik*, 397:325–400, 1930. `http://onlinelibrary.wiley.com/doi/10.1002/andp.19303970303/abstract`.

[98] C. Amsler et al. Passage of particles through matter. *Phys. Lett.*, B667 (1), 2008. `http://pdg.lbl.gov/2008/reviews/passagerpp.pdf`.

[99] CMS Collaboration. Performance of muon identification in pp collisions at $\sqrt{s} = 7$ TeV. *PAS*, MUO-10-002, 2010. `http://cdsweb.cern.ch/record/1279140/`.

[100] D. Dobur for the CMS collaboration. Jets and Missing Transverse Energy Reconstruction with CMS. *PoS*, 2009. `http://arxiv.org/abs/0904.0391`.

[101] CMS Collaboration. Performance of Jet Algorithms in CMS. *PAS*, JME-07-003, 2007. `http://cdsweb.cern.ch/record/1198227/`.

[102] M. Cacciari and G. Salam. The anti k_t jet clustering algorithm. *JHEP*, 04:063, 2008. `http://arxiv.org/abs/0802.1189`.

[103] CMS Collaboration. Jet Performance in pp Collisions at $\sqrt{s} = 7$ TeV. *PAS*, JME-10-003, 2010. `http://cdsweb.cern.ch/record/1279362/`.

[104] CMS Collaboration. Particle-Flow Event Reconstruction in CMS and Performance for Jets, Taus, and E_T^{miss}. *PAS*, PFT-09-001, 2009. `http://cdsweb.cern.ch/record/1194487/`.

[105] CMS Collaboration. Determination of the Jet Energy Scale in CMS with pp Collisions at $\sqrt{s} = 7$ TeV. *PAS*, JME-10-010, 2010. `http://cdsweb.cern.ch/record/1308178/`.

[106] K. Kousouris. Relative Response from Dijet Balance with 7 TeV data. JEC Meeting, August 2010. unpublished, restricted access at `http://indico.cern.ch/getFile.py/access?contribId=2&resId=0&materialId=slides&confId=105277`.

[107] Trigger Menu Development for 2010 7 TeV Collision Data . internal twiki page, topic revision: r188 – 14-Mar-2011, restricted access at `https://twiki.cern.ch/twiki/bin/view/CMS/TriggerMenuDevelopment#Trigger_Menu_Development_for_201`.

[108] CMS Top Dilepton Working Group: V. Krutelyov et al. Reference analysis for 2010 data taking with 38X. Pass 6., 2010. internal twiki page, topic revision: r78 – 14-Feb-2011, restricted access at `https://twiki.cern.ch/twiki/bin/viewauth/CMS/TopDileptonRefAnalysis2010Pass6`.

[109] N. Saoulidou. Particle Flow Jet Identification Criteria. *analysis note*, AN-10-003, 2010. unpublished, restricted access at `http://cms.cern.ch/iCMS/jsp/openfile.jsp?tp=draft&files=AN2010_003_v3.pdf`.
N. Saoulidou. PF Jet ID Recommendation for 7 TeV Analyses. April 2010. unpublished, restricted access at `http://indico.cern.ch/getFile.py/access?contribId=0&resId=0&materialId=slides&confId=89919`.

[110] D. Barge et al. A measurement of top quark pair production cross section in dilepton final states in pp collisions at 7 TeV. *analysis note*, AN-10-410, 2010. unpublished, restricted access at `http://cms.cern.ch/iCMS/jsp/openfile.jsp?tp=draft&files=AN2010_410_v5.pdf`.

[111] J. Brochero et al. Measurement of the $t\bar{t}$ cross section in the dilepton final state using b-tagging at $\sqrt{s} = 7$ TeV. *analysis note*, AN-10-406, 2010. unpublished, restricted access at `http://cms.cern.ch/iCMS/jsp/openfile.jsp?tp=draft&files=AN2010_406_v6.pdf`.

[112] E. Gallo. Top MET studies. DESY Top Meeting, January 2011. unpublished, restricted access at `http://indico.desy.de/getFile.py/access?contribId=0&resId=0&materialId=slides&confId=3955`.

[113] Spring10 & Summer10: 7 TeV FastSim Production. internal twiki page, topic revision: r41 – 24-Aug-2010, restricted access at `https://twiki.cern.ch/twiki/bin/view/CMS/ProductionFastSimSpring10#FASTSIM_AN1`.

[114] M. Aldaya, W. Behrenhoff, D. Dammann, A. Geiser, J. Hauk, B. Lutz, M. Marienfeld, A.B. Meyer. Measurement of the Cross-Section Ratio of Top-Pair Production and Z^0 Production in pp Collisions at $\sqrt{s}$ =7 TeV using the CMS Detector. *analysis note*, AN-10-429, 2010. unpublished, restricted access at `http://cms.cern.ch/iCMS/jsp/openfile.jsp?tp=draft&files=AN2011_018_v5.pdf`.

[115] K. Kondo. Dynamical likelihood method for reconstruction of events with missing momentum. i. method and toy models. *JPSP*, 57(12):4126–4140, 1988. `http://jpsj.ipap.jp/link?JPSJ/57/4126/`.
K. Kondo. Dynamical likelihood method for reconstruction of events with missing momentum. ii. mass spectra for 2 → 2 processes. *JPSP*, 60 (3):836–844, 1991. `http://jpsj.ipap.jp/link?JPSJ/60/836/`.
K. Kondo, T. Chikamatsu, and S. Kim. Dynamical likelihood method for reconstruction of events with missing momentum. iii. analysis of a cdf high p_T eμ event as $t\bar{t}$ production. *JPSP*, 62(4):1177–1182, 1993. `http://jpsj.ipap.jp/link?JPSJ/62/1177/`.

[116] D. Tornier. Untersuchung dileptonischer $t\bar{t}$-Zerfalle bei CMS. *Diplomarbeit*, 2005. in german, `http://www.physik.rwth-aachen.de/fileadmin/user_upload/www_physik/Institute/Inst_3B/Forschung/CMS/Analyse/Veroeffentlichungen_und_Arbeiten/Diplomarbeit_Tornier.pdf`.

[117] CMS Collaboration. Commissioning of b-jet identification with pp collisions at $\sqrt{s} = 7$ TeV. *PAS*, BTV-10-001, 2010. `http://cdsweb.cern.ch/record/1279144/`.

[118] J. Campbell and R. K. Ellis. MCFM for the Tevatron and the LHC. *Nucl. Phys. Proc. Suppl.*, 205-206:10–15, 2010. `http://arxiv.org/abs/1007.3492`.

[119] A. Cooper-Sarkar on behalf of the H1 and ZEUS. Proton Structure from HERA to LHC, 2010. `http://arxiv.org/abs/1012.1438`.

[120] Predictions provided by K. Lipka and R. Plačakytė.

[121] CMS Collaboration. Combination of top pair production cross sections in pp collisions at 7 TeV and comparisons with theory. *PAS*, TOP-11-001, 2011. `http://cdsweb.cern.ch/record/1336491/`.

[122] ATLAS Collaboration. A combined measurement of the top quark pair production cross-section using dilepton and single-lepton final states. *ATLAS-CONF-2011-040*, 2011. `http://cdsweb.cern.ch/record/1338569`.